University of Nairobi

SCHOOL OF ENGINEERING

DEPARTMENT OF MECHANICAL AND MANUFACTURING ENGINEERING.

AN INVESTIGATION OF THE FATIGUE PROPERTIES OF THE ALUMINIUM-COPPER ALLOY 2014.

By

MURITHI ALFRED MUCHANGI

F56/32924/2019

A Thesis submitted in partial fulfillment of the requirements for the degree of Master of Science in Mechanical Engineering, in the Department of Mechanical and Manufacturing Engineering in the University of Nairobi

@ March 2022

DECLARATION

I, Murithi Alfred Muchangi, hereby declare that this thesis is my original work and to the best of my knowledge, the work presented here has not been presented in any other institution of higher learning.

.....AMG..... .....10/03/2022.....

Murithi Alfred Muchangi. Date.

This thesis has been submitted for examination with our approval as university supervisors.

.....Prof. G. O. Rading..... .....14th March 2022.....

Prof. G. O. Rading. Date.

....15th March 2022.....

Dr. T. O. Mbuya Date.

DEDICATION

This thesis is dedicated to my family for their support during the entire period of this study. This thesis is also dedicated to my supervisors, Prof. G. O. Rading and Dr. T. O. Mbuya for their great source of inspiration and motivation.

ACKNOWLEDGEMENTS

I would like to appreciate the following people and institution for the roles they played in the course of this study.

1. My supervisor Prof. G. O. Rading for his guidance, immense knowledge and also for funding this work during the entire period of this course.
2. My second supervisor Dr. T. O. Mbuya for his guidance and offering valuable insights to the project.
3. The university of Nairobi for granting me access to its workshop and laboratories at the Department of Mechanical and Manufacturing Engineering.
4. Mr. Macharia and Mr. Kigen for their assistance in machining the specimens required for mechanical testing and microstructural analysis.
5. Miss Jackline and Mr. Akhusama of the University of Nairobi for their assistance during the polishing of the specimens and optical micrograph analysis.

Lastly, I would like to thank my family for their prayers, encouragement and continuous support throughout my research.

ABSTRACT

Investigating fatigue properties is very important to researchers since the knowledge of the fatigue life is required in both design and predicting the life of aircraft and other structural materials. Through experimental study of fatigue properties, prevention of tragic events like the infamous Aloha airline disasters can be achieved. Owing to its relatively high strength and low density, the aluminium alloy AA 2014 has been the primary structural material for aircrafts. In military and commercial airplanes, rivets are been replaced by welds so as to improve on cost and structural integrity. Porosity and hot cracking are some of the major welding defects encountered during welding of high-strength AA 2014 aluminium alloy. Upon repetitive loading on these welded structural components cracks develop and grow leading to catastrophic failures. This study therefore investigates the fatigue properties of AA 2014 aluminium alloy. Fatigue crack growth (FCG), low cycle fatigue (LCF) and high cycle fatigue (HCF) properties of AA 2014 aluminium alloy as-received were investigated.

Welding also affects the microstructure, mechanical properties and fatigue properties of the heat affected zone (HAZ). Therefore, the effect of the welding process on fatigue properties of AA 2014 aluminium alloy was also analyzed. Since investigating HAZ of real welded joints is difficult because of the narrowness of the HAZ, a suitable process of thermal simulation was employed to prepare specimens used to study the various sub zones of the heat affected zone. This process involved thermal simulating the two regions of HAZ to an already predetermined welding temperature. Thermal simulation done was one that resulted in as close as possible to the thermal cycle histories studied earlier by actual welding obtained using alternating current gas tungsten arc welding (GTAW). The simulation process was done using a muffle furnace that had a peak temperature of 1200 $^{\circ}$C. Specimens were put in the muffle furnace to simulate the two regions of the HAZ with peak temperatures of 590 $^{\circ}$C (region C) and 650 $^{\circ}$C (region D) representing regions 5mm and 4mm respectively from the weld center line.

The HAZ region located at 5 mm from the weld centerline was found to offer least resistance to fatigue crack growth, had shorter fatigue life and displayed lowest value of hardness and fatigue strength compared to both the base metal (BM) and the HAZ region located at 4mm from the weld center line. The optical micrographs of the base metal and the two regions of the heat affected zone were carried out using a universal optical microscope named OPTIKA B-353

MET. The optical micrographs were taken at a magnification of X200 with the BM and the two regions of HAZ oriented in the longitudinal transverse direction (L-T). Microstructure characterization was also carried out. The HAZ region C recorded the highest grain size value compared to the base metal and heat affected zoned region D. In this study, HAZ region C was confirmed to be the weakest link in the HAZ which is significantly affected by the thermal cycle profiles developed during the thermal cycle simulation process. The potential precipitates in Al-Cu (2xxx series) alloys particularly AA 2014 are $CuAl_2$, and $Al_5Cu_2Mg_8Si_5$. The possible cause of weakness in HAZ region C was associated with dissolution of strengthening phases. Precipitate dissolution in AA 2014 occurs as the particles of this alloy are exposed to thermal cycle temperatures higher than 400 °C. Therefore, degradation of the strengthening phases of AA 2014 aluminium alloys occurs severely at 590 °C due to dissolution of $CuAl_2$ precipitates in aluminium matrix.

Anti-Plagiarism Statement

I would like to confirm that this thesis has been written by me and in my own words, except where otherwise explicitly acknowledged. I am aware that the incorporation of material from other works or paraphrase of such material without acknowledgement will be treated as plagiarism, subject to the custom and usage of the subject, according to the University Regulations on Conduct of Examinations.

.....AMG..... .....10/03/2022.....

Murithi Alfred Muchangi. Date.

NOMENCLATURE

a	Half crack length for central crack
da/dN	Crack growth rate (length per cycle)
$\Delta\varepsilon_e$	Elastic strain range
$\Delta\varepsilon_p$	Plastic strain range
$\Delta\varepsilon_t$	Total strain range
ε_f	Fatigue ductility coefficient
K	Stress intensity factor (MPa$\sqrt{m}$)
K_{IC}	Plane strain fracture toughness
K_C	Fracture toughness
ΔK	Range of stress intensity factor
ΔK_{eff}	Effective range of stress intensity factor
ΔK_{th}	Threshold range of stress intensity factor
N_f	Number of cycles to failure
ΔP	Range of load
R	Stress ratio
T	time
T6	Solution heat treated and then artificially aged
$\Delta\sigma$	Stress range
θ''	Coherent Al_2Cu Phase
θ'	Semi coherent Al_2Cu Phase
θ	Stable Al_2Cu Phase

ABBREVIATIONS

AA	Aluminium Association
ASTM	American Society for Testing and Materials
BM	Base Metal
EBW	Electron Beam Welding
FCG	Fatigue Crack Growth
FL	Fusion Line
FZ	Fusion Zone
FSW	Friction Stir Welding
GP	Guinier Preston
GPBZ	Guinier–Preston–Bagariastkij Zones
GMAW	Gas Metal Arc Welding
GTAW	Gas Tungsten Arc Welding
HAZ	Heat Affected Zone
HCF	High Cycle Fatigue
HV	Vickers Hardness
LEFM	Linear Elastic Fracture Mechanics
LCF	Low Cycle Fatigue
NZ	Nugget Zone
PWHT	Post Weld Heat Treatment
PFZs	Precipitates Free Zones
SEM	Scanning Electron Microscope

SSS	Supersaturated Solid Solution
TMAZ	Thermo-Mechanically Affected Zone
WM	Weld Metal
WN	Weld Nugget
WRS	Weld Residual Stresses

TABLE OF CONTENTS

LIST OF TABLES

LIST OF FIGURES

CHAPTER ONE: INTRODUCTION

1.1 Background

Aluminium alloys, after ferrous metals, are the most often used structural alloys. These alloys find use in the aerospace and automotive sectors due to their low density and exceptional corrosion resistance [1]. In its completely heat-treated state, AA 2014 is an aluminium alloy containing 4-5 percent copper. AA 2014 exhibits excellent machinability which has inspired its frequent use in the aviation and military industries for the manufacture of high-strength components. Commercially, the alloy is used to manufacture truck frames, structural applications, aircraft structures, military vehicles, high-strength structural components and aerospace fittings [2].

AA 2014 can be machined in specific tempers, and is one of the strongest available alloys of aluminium with additional properties such as high hardness. One problem with the alloy is its low weldability since it cracks when welded [3]. After 2024 aluminium alloy, AA 2014 is the most popular of the 2xxx-series aluminium alloys. AA 2014 aluminium alloy is typically supplied in T651 form and manufactured as extruded flat bar, hexagon bar, channels, round tube, tee sections hollow bar, plate, sheet, strip, rectangular tube, round bar, square tube, and square bar. The alloy has a relatively low corrosion resistance. To overcome this, it is frequently encased with pure aluminium [4].

Aluminium's relative lightness is one of its most notable properties. Magnesium, lithium, and silicon are typical alloying elements that reduce the density of aluminium whereas copper, chromium, iron, nickel, zinc, titanium, and manganese enhance it [5]. Due to its high solubility and strengthening effect, copper is one of the highly significant alloying metals for aluminium. Many commercial alloys contain copper in amounts ranging from 1 to 10%. They are used either as the main addition or as one of the primary elements for alloying. Copper is the main alloying element in AA 2014 alloy. The chemical composition of this alloy is shown in Table 1.1.

Table 1.1: The chemical composition of AA 2014[6].

Element	Si	Fe	Cu	Mn	Mg	Cr	Zn	Ti	Al
2014	0.81	0.7	4.4	0.8	0.50	0.10	0.25	0.15	Remainder

Due to their greater strength compared to other aluminium alloys, 2xxx alloys (Aluminium-Copper) are more commonly used in aviation applications [3]. Precipitation hardening gives these alloys their strength. Artificial aging of these alloys causes strengthening through coherent precipitates in the matrix, which imparts greater strength owing to coherency stresses around every precipitate. By precipitation of strengthening secondary phases, AA 2014 alloy is an Aluminium-Copper-Magnesium-Silicon type alloy with properties including better strength, improved tolerance to damage, and strong resistance to FCG in comparison to other families of aluminium alloys [7].

Age hardening also referred to as precipitation hardening, is among the most common processes for metal alloys strengthening. The essential knowledge and framework for this approach were formed in early work on Duralumin at the United States Bureau of Standards [8]. Age hardening can increase hardness and strength of some metal alloys via the formation of second phase particles that are very small and evenly dispersed within the initial phase of the matrix. The particles of the precipitate impede dislocation motion hence strengthening the heat-treated alloys. Age hardening methods can strengthen several aluminium based alloys, Cu-Sn alloys, some steels, titanium alloys and nickel based superalloys.

Since AA 2014 displays a high strength to weight ratio and good fatigue resistance, it is frequently used for structural applications (especially in the aviation and automobile industries) at medium service temperatures. This alloy's mechanical characteristics are achieved by the precipitation or age hardening phenomenon [9]. The alloying components are fully dissolved in solid solution, and the material exhibits a behavior similar to a single phase material with low hardness and strength. Depending on the aging temperature, the alloying elements cluster and begin to produce various forms of tiny precipitates. Precipitation strengthening of alloys demands a terminal solid solution that has diminishing solubility of solids as temperature falls [10]. Figure 1.1 depicts this sort of reduction along the solvus between the α and α+θ regions of the Aluminium-Copper phase diagram. Consider a 96-weight-percent Al – 4-weight-percent Cu alloy, which was chosen due to the significant drop in the solid solubility of solid solution following a reduction of temperature from a value of 550°C to 75°C. Solution treatment, quenching, and aging are the three main steps in the process of precipitation hardening.

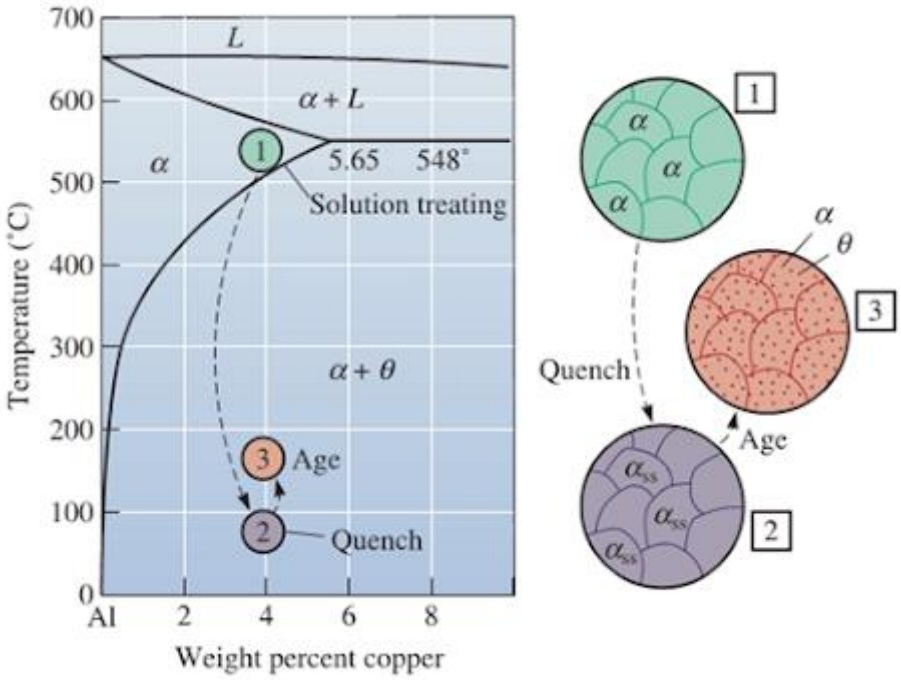

Figure 1.1: Aluminium-Copper phase diagram demonstrating precipitation hardening process and the microstructures types produced [11].

Researchers [12-15] have studied what happens during these three steps in the process of precipitation hardening. The first stage, known as solution treatment involves the heating of the alloy way above its solvus temperature before holding it at that temperature until the formation of a homogeneous solid solution (α). The stage is also referred to as solutionizing. The second stage is called quenching, involving a rapid cooling of the solid (α), resulting in a supersaturated solid solution $\alpha_{SS}.\alpha_{SS}$ consists of excess copper and exists as a non-equilibrium structure. The stage also involves a limited time, not sufficient for atoms to disperse into nucleation sites resulting in the lack of formation of θ precipitates. In the final stage, the supersaturated α, α_{SS}, is heated below the solvus temperature to form a finely distributed precipitate in a process known as aging. It is during this aging temperature that a short distance dispersion of atoms is observed and a spread of the additional Cu atoms to several nucleation sites and formation of precipitates due to the instability of the supersaturated α. The ultimate end result of the precipitation hardening process is the creation of a finely distributed precipitate which obstructs dislocation motion by ensuring that the dislocations are forced to cut through or go around the precipitated

particles. Limiting dislocation movement in the process of deformation is a means of strengthening the alloy.

1.2 Problem Statement

This thesis aims to investigate the microstructure, mechanical properties and fatigue properties in the BM and HAZ of the aluminium alloy 2014. The HAZ, which is defined as the region adjacent to the weld metal zone [16], is composed of BM that does not melt but is exposed to high enough temperatures that enables grain growth to occur. A study by Sawka [16] and others [17, 18] model HAZ of AA 2014 and AA 2024 as a single material. However, it has been shown that HAZ is comprised of 3 metallurgical distinct regions namely, the region of grain growth, the grain refinement and the transition region [19]. Steep property gradients in the HAZ make it extremely difficult to study the fatigue properties from an actual weld. An approach to determine the behaviour of HAZ with regard to FCG characteristics and fatigue properties in AA 2014 has not been investigated exhaustively since the HAZ has been treated as one region during the analysis of fatigue properties in most studies. This thesis will address this problem by finding the endurance limit, the LCF and the FCG characteristics at selected points in the HAZ of aluminium alloy AA 2014.

1.3 Justification of the Study

There are numerous ongoing research studies to improve the prediction of FCG in aluminium aircraft structures. Due to the fairly low fracture toughness of the high strength materials such as AA 2014 developed for the aerospace industry, structural fatigue continues to be a crucial design concern in the aviation industry [20, 21]. It is a serious concern hampering the safety and economic viability in aviation [22]. On occasion, factors such as visibility constraints mean that cracks go undetected. However, the application of repetitive stress results in the growth of these cracks and the ultimate failure of the structure by this mechanism of fatigue. The eventual outcome of this failure is often catastrophic, such as the infamous Aloha Airlines or Comet disasters [23]. Knowledge of fatigue properties is of critical importance to researchers who want to ensure that disasters like the Aloha Airlines are avoided. This work provides an extensive

experimental investigation of the FCG, LCF and HCF that offers a better understanding of fatigue properties of AA 2014 aluminium alloy.

The AA 2014 alloy belongs to the 2xxx family, initially developed for application in aerospace launch vehicles, and now considered suitable for welded structural parts in commercial aircrafts. In both cases, an adequate damage tolerance is required. In this respect, the fatigue crack propagation resistance is a critical property. Among the 2xxx series aluminium alloys, the choice of AA 2014 is gaining more important research interests for aero-structures applications. There are fatigue crack propagation results reported in references [23] and [24] for a 2xxx aluminium alloy. However, less research work has been carried out that focuses on fatigue behavior of AA 2014 aluminium alloys. This thesis will provide more experimental data on the fatigue response and also contribute in offering more literature on fatigue properties in HAZ of AA 2014.

1.4 Objectives of the Study.

1.4.1 Broad Objective

This study aims to link the microstructural changes in the HAZ to the fatigue properties (Fatigue Crack Growth, High Cycle Fatigue and Low cycle fatigue) and hardness characteristics of welded AA 2014 based on the principle that the HAZ is composed of different microstructural regions.

1.4.2 Specific Objectives

a) Simulation of two different regions of the HAZ (weakest regions of HAZ located 4mm and 5mm from the weld centerline) by subjecting the material to thermal histories as close as possible to thermal histories experienced in actual welding of the two different regions.
b) To determine the fatigue properties (i.e., Fatigue Crack Growth, High Cycle Fatigue and Low cycle fatigue) of the BM and two simulated regions of the HAZ.
c) Characterization of the microstructure of the BM and two simulated regions of the HAZ using optical microscopy.

d) Characterization of the hardness profiles of the HAZ in order to find the weakest region of the HAZ.

1.5 Limitation of the Study.

- Comparison between thermal cycle histories of the muffle furnace and Gleeble simulator was not conducted since the Gleeble simulator could not be found locally.

CHAPTER TWO: LITERATURE REVIEW

2.1. Precipitation Sequence and Hardening of AA 2xxx.

Precipitation hardening, also referred to as age hardening, remains one of the most common processes used to strengthen alloys of metals. Age hardening produces the strongest aluminium alloys (6xxx, 7xxx and 2xxx) [11]. Artificial aging initiates the precipitation of the supersaturated solution and a consequent rise in the material's strength is also accompanied by a rise in both size and quantity of the precipitates [25]. Eventually, the strength reaches a maximum value, also referred to as the peak aged state, and any additional over-aging causes coarsening of the precipitates and a decrease in strength.

The precipitation events observed during age hardening can be extremely complex, and multiple intermediary phases are frequently involved. In an aluminium-copper (2xxx) alloy, for example, aging often begins with the formation of extremely fine plate like Guinier–Preston (GP) zones in the aluminium matrix on {001} planes. At this point, Guinier–Preston zones have a diameter of around 10 nm and are made up of single planes of copper atoms. As the Guinier–Preston zones age, they develop into a cohesive θ" phase. Further aging occurs in sequential transformations to semi-coherent θ' and, finally, plate-like θ-$CuAl_2$ particles. The aging kinetics and, to a lesser degree, the precipitation sequence are determined by the diffusion of copper atoms and are impacted by vacancy levels as well as the existence of traces of specific elements that interact with the vacancies, such as cadmium, indium, or tin [25].

The precipitation of various phases in aluminium alloys is caused by the presence of different micro-alloying components and suitable heat treatment. The effect of age hardening treatments on hardness is depicted on a graph in Figure 2.1. The hardness change with aging time shows various peaks correlating to different phases precipitating. Presence of a typical precipitation sequence is visible in the aging curve. Figure 2.1 shows a rapid increase in hardness level (from solution-treated state,105 HV) after artificial aging for 4 hours, which is attributable to the development of the GP I zone (which are coherent with the matrix) [26]. Aging further between 4 hours to 12 hours leads to additional hardness increase, with a peak hardness of around 150 HV reached in 12 hours.

Peak hardness in this alloy is caused by the precipitation of the θ′ particles/metastable phase and second phase θ″ with defined crystal structure [26]. Aging for extended periods of more than 12 hours, results in a continuous decrease in the hardness level due to process of over-aging. Material softens as a result of precipitation of non-coherent stable precipitates (the equilibrium phase θ, which results in loss of coherency strain) or due to coarsening of previously precipitated particles. As aging continuous at any temperature point, tiny particles tend to dissolve and the resulting solution precipitates on bigger particles, forcing them to expand and reducing the overall interfacial energy in a process called particle coarsening [26].

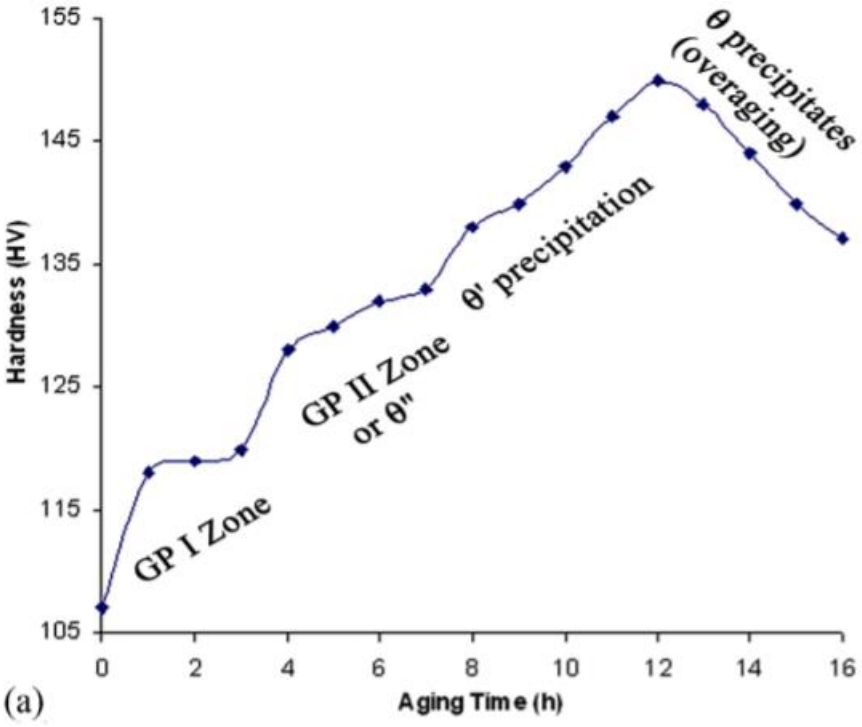

Figure 2.1: Graph of hardness Vs aging time for AA 2014 alloy [26].

There has been a lot of research done on precipitation hardening in aluminium-copper, aluminium-copper-silicon-magnesium and aluminiun-copper-magnesium alloys. According to numerous studies, there exists three potential sequences of precipitation in AA 2014 that cause precipitation hardening [9, 27]. 'α_{sss}' Guinier Preston Zones (GPZ) is the copper based clusters (copper-rich phase) in the aluminium matrix whereas θ is the stable Al_2Cu phase and θ′ and θ″ are the metastable Al_2Cu phases. Similarly, GPBZ stands for Guinier–Preston–Bagariastkij

Zones, which are Cu–/Mg-based clusters. Q is the quaternary phase, characterized by having an Al-Cu-Mg-Si composition [9, 27, 28]. The precipitation sequence for various alloys is presented in equations 2.1 to 2.3.

$$\alpha_{sss} \rightarrow GPZ \rightarrow \theta'' \rightarrow \theta' \rightarrow \theta \ (Al_2Cu) \ldots\ldots [2.1]$$

$$\alpha_{sss} \rightarrow GPBZ \rightarrow S'' \rightarrow S' \rightarrow S \ (Al_2CuMg) \ldots\ldots [2.2]$$

$$\alpha_{sss} \rightarrow GPZ \rightarrow Q' \rightarrow Q \ (Al_3Cu_2Mg_9Si_7 \text{ or } Al_4Cu_2Mg_8Si_7) \ldots\ldots [2.3]$$

According to Abis et al [28], the quaternary alloy precipitation sequence (Al–Cu–Si–Mg) is typically determined by the relative quantities of alloying elements. A copper concentration above 4 weight percent increases the likelihood of formation of θ precipitation sequence described in the literature occuring. Chakarbarti and Laughlin [10] also noted that in high copper quaternary alloys, the precipitation sequence of the Mg_2Si β-phase, and that of the θ-phase, are detectable when the magnesium/silicon ratio is larger than one. However, if the magnesium/silicon ratio is less than 1, as in the case of AA 2014 aluminium alloy, which is primarily a quaternary alloy of aluminium–copper–silicon–magnesium, the precipitation of the S phase (ternary phase) or Q phase (quaternary phase) sequence is highly likely. However, the existence of Q or S phase during the precipitation process depends on the amount of silicon present. If the silicon quantity is less than 0.1 weight percent, the S phase is precipitated; otherwise the Q phase will be precipitated.

Merica et al [8, 29, 30] investigated the effect of different heat treatments and chemical composition on alloy hardness. The research disclosed that the solubility of $CuAl_2$ in aluminium was directly related to the temperature, such that an increase in temperature increased the solubility. They highlighted the four main aspects of the original Duralumin theory. The first and second highlight was that age hardening is possible due to the solubility-temperature relationship of the hardening constituent in aluminium and that the hardening constituent is $CuAl_2$. The third highlight was that hardening is caused by precipitation of the constituent in a form separate from atomic dispersion and highly likely to be in fine colloidal, molecular or crystalline form. Lastly, this theory highlighted the fact that the hardening effect of $CuAl_2$ in aluminium is related to the size of its particles.

2.2. Welding of 2xxx Aluminium Alloys.

Welding is a permanent joining technique that uses heat and/or pressure to fuse materials such as metals, alloys, or polymers together at their contacting surfaces. The work pieces to be connected are melted at the contact during welding, and following solidification, a permanent connection can be formed [31]. Aluminium and its alloys are regarded as having lesser weldability than steels for a variety of reasons, including its strong affinity for ambient gases, high electrical and thermal conductivity, high thermal expansion coefficient, low stiffness, and wide solidification temperature range [32]. Such properties of aluminium alloys in general render them susceptible to fault development during welding. The influence of the above characteristics on weld joint performance is generally reduced using two approaches. The first approach is known as effective protection of the weld pool from contamination by atmospheric gases, which is done using proper shielding methods and cutting down the weld thermal cycling influence through the use of a welding process of higher energy density. The second approach focuses on using different environments (argon, vacuum, helium, or argon-vacuum-helium mixture with hydrogen and oxygen) to provide shield to the weld pool from ambient gases.

The first approach has resulted in the development of newer processes of welding such as laser, pulse variants of GTAW and gas metal arc welding (GMAW), and friction stir welding (FSW) [33, 34]. To be manufactured into a desired shape for structural applications, 2xxx aluminium alloys require shaping and joining procedures. As a result of rapid development of a stable oxide layer when exposed to air, welding of aluminium alloys is usually a difficult operation. Some significant flaws observed during welding process of high strength 2xxx alloys include porosity development, hot cracking, and the production of segregated coarse microstructure in the fusion zone (FZ) [33, 34]. Among the many welding types, GTAW is the best, producing reasonably clean and high-quality welds [34, 35].

In the 1940s, the GTAW method was developed for welding magnesium and aluminium alloys especially in the aviation industry. GTAW was created as a replacement for shielded arc welding (SMAW) which was not very effective in the welding of such metals [33]. An electrical arc is positioned between an electrode made of tungsten and the component to be welded in the GTAW process. The process involves the use of high voltage to break down the insulating gas contained

between the electrode and the component in order to initiate the arc. Current is further passed through the electrode which forms an electrode arc. The arc's tremendous heat melts the metal to be welded, which then fuses together with or without a filler substance. Furthermore, inert gas is used to fill the arc zone as a protection of both the tungsten electrode and the molten material from oxidation and to create a conducting channel for the arc current. Shielding gases utilized include argon, helium, argon-helium combinations, and tiny amounts of hydrogen combined with argon. Typically, the shielding gas is selected based on the BM to be welded [35]. A simple welding setup includes the following components: a welding power source, a welding controller, a welding torch, and a tungsten electrode.

Welding settings in application are also critical components of the GTAW process, other than the equipment used. A weld program is a set of welding settings designed to produce a certain weld output and quality. Since changes in parameters can alter the quality of the final weld, welding variables are often noted down, or kept in the memory of the welding machine [36]. In several applications that dictate high-purity or precision, there is need for specifications that detail the welding parameters such as the base material; weld joint: part diameter and part fit-up requirements. Other parameters including the arc length, shield gas purity and type, tungsten electrode material, surface condition, and tip geometry, may be provided [34]. Some welding equipment manufacturers provide a library of welding programs that have already been pre-calculated to accommodate a wide range of component sizes, materials, and thicknesses. Welders should always follow the methods recommended by the equipment provider first since the vendors have typically done a substantial amount of qualification and troubleshooting work [34]. Current, frequency, voltage, welding gun speed, arc length, welding gun location, shielding gas, and heat input are some of the many weld parameters that primarily affect weld quality.

The secondary Al_2Cu phase (θ) in AA 2014 alloys is often distributed inside the matrix and at grain boundaries [7]. Due to the use of targeted heat input, welding of high strength alloys using fusion can result in dramatic microstructural changes. The result is a change to a grain structure consisting of equiaxed and dendritic coarse grains in the FZ accompanied by considerable coarsening of grains in the HAZ [37]. Furthermore, the percentage and size of the Al_2Cu precipitates in various zones are changed as a result of precipitate coarsening and/or dissolution.

The secondary Al_2Cu phase (θ) in AA 2014 alloys is dispersed along grain boundaries and within the aluminium matrix [7]. Drastic microstructural changes take place following welding of high strength aluminium alloys. The changes often see a shift from a traditional grain structure to equiaxed grains with coarse dendritic-like column in the FZ. Besides, the application of localized heat causes a coarsening of grains in the HAZ [37]. Also, the coarsening of the precipitates results in the alteration of the size and fraction of the Al_2Cu precipitates at varying zones [38]. Changes in grain sizes, microstructures, precipitate fraction and distribution in various zones can all have an impact on the electrochemical and mechanical characteristics of the welded region. Sinhmar and Dwivedi [37] studied corrosion behavior microstructure characteristics of AA 2014 alloy following GTAW and FSW. According to their findings, the Al_2Cu precipitates that were present in both GTAW and FSW weldments had accelerated the anodic and cathodic reaction, and gas tungsten arc weldments exposed to higher temperatures were more vulnerable to sensitization than friction stir welding weldments.

2.3. Microstructural Evolution During Welding.

A typical fusion weld comprises many different areas, which may be roughly categorized as a FZ, where melting and re-solidification takes place, and a HAZ, the area next to the BM whose microstructure is distorted by welding heat. The Process of solidification, more than post-solidification changes, determines the microstructure of the FZ in aluminium alloys. A limited area of the BM is melted and solidified during welding. The interplay between temperature gradient, solidification growth rate, and diffusion determines the solidification morphology as well as the solute distribution. As a result, different welding techniques have varied effects on the weld microstructure and subsequent characteristics. High energy density methods, such as electron beam welding (EBW), create refined microstructures, whereas arc welding procedures, such as GTAW, produce coarser microstructure. The FZ can only be strengthened by aging after welding because much of the solute required to create precipitates is bound up in a eutectic component that develops at the conclusion of solidification [39].

Solid state processes that occur in areas heated to extreme temperatures as heat flows out from the FZ largely determine the microstructure within the HAZ. Most HAZ microstructural changes

in lithium-bearing aluminium alloys are related with a shift in the strengthening precipitates. Other modifications, such as grain coarsening, may influence microstructure development, although their impact on HAZ characteristics is minimal. Precipitation coarsening is expected to be restricted to areas with relatively low peak temperatures, whereas precipitate dissolution appears to occur in areas with higher peak temperatures. Because one phase may dissolve while another coarsens, it is difficult to provide a quantitative study of the heat affected zone of alloys including a range of strengthening precipitates. Dissolution and coarsening are both predominantly diffusion-controlled processes.

The dissolution of precipitates at the grain boundary supplies solute in the matrix resulting in higher alloy strength owing to solid solution strengthening, although the overall increase in strength in these places is due to re-precipitation upon cooling from welding temperatures. Regions with partial dissolution have lower strength owing to a smaller precipitation percentage, whereas regions with lower temperatures have lower strength due to the precipitate coarsening effect [40, 41].

2.4. HAZ Strength and Hardness of AA 2014.

The microhardness survey throughout the weld in GTAW AA 2014 Alloy is shown in Figure 2.2. According to Shankar et al [42], the weld core has a low hardness value compared to the other areas of the weld. A rapid reduction in hardness was seen from the fusion border to the HAZ, which is ascribed to precipitate coarsening and grain coarsening impact. In general, the weld metal comes as close as possible to the equilibrium condition whether the weld metal cools quickly or not. The hardness is low around the weld center due to the dissolution of hardening precipitates. However, grain coarsening and dissolution of coherent Al_2Cu phase might have had a contribution to the low levels of hardness values recorded in HAZ. The fluctuation in hardness inside the FZ of the weldment to the fusion line (FL) is ascribed to changes in solute concentration and, as a result, the amount of equilibrium Al_2Cu as a second phase.

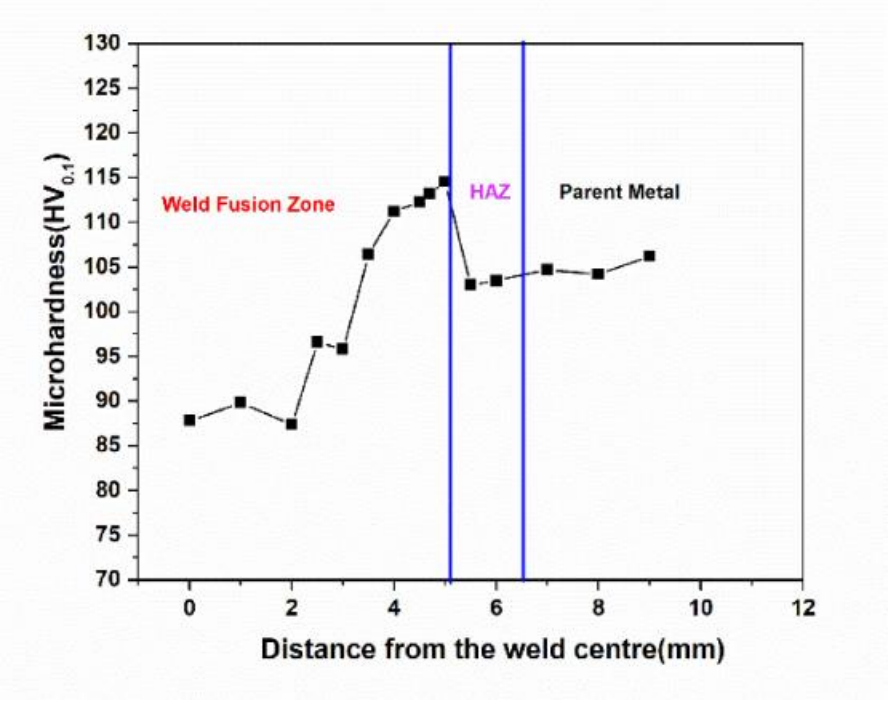

Figure 2.2: The weld microhardness values in Gas Tungsten Arc Welded AA 2014 Aluminium Alloy [42].

The weldment's maximum hardness value is generally found at the weld metal/HAZ boundary. Away from the weld fusion line, other areas of the HAZ exhibit an increase in hardness value [43, 44]. According to studies [45-50], the HAZ generally has one or more maxima and minima hardness value(s). Researchers [44, 51, 52] ascribe the HAZ's poor strength and/or hardness to the material's microstructure. This weakness experienced in the HAZ has been attributed to several factors which includes; dissolution of strengthening precipitates in both the HAZ and the weld metal [45, 47, 53], precipitation of incoherent equilibrium precipitates at the same time [45], lack of locations where precipitates can nucleate to cause natural aging [54], segregation of intermetallic phases to dendritic boundaries [44, 51, 52] and solute atom segregation to interdentritic phases leaving the dendrite matrix without the advantage of solution strengthening [45, 52].

2.5. Fatigue Crack Growth

2.5.1 Crack Surface Displacement Modes.

Fatigue failure may initiate from a machined notch or material defect. Understanding the basic displacement modes of surface crack through which a crack can extend is essential before the prediction of crack propagation can begin. As shown in figure 2.3, three basic modes of crack surface displacement exist [55]. The first one is known as Mode I. Often consisting of the crack faces moving apart, Mode I is the most common mode of fatigue loading. The second one is called Mode II. The sliding mode as it is also known, is characterized by the crack faces sliding relative to one another. It often occurs in a direction perpendicular to the crack's leading edge. The final mode is referred to as Mode III. It is characterized by the crack faces sliding in a direction parallel to the leading edge [20]. Tension loading causes mode I, whereas shear loading causes modes II and III. Because mode I is the most common mode of macroscopic FCG, nearly all studies have been focused on it.

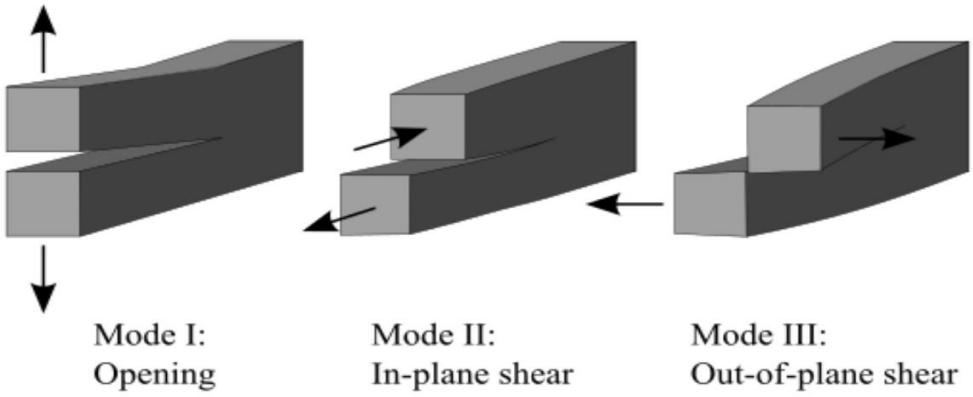

Figure 2.3: Basic crack surface displacement modes [56].

2.5.2 Fatigue Crack Growth Rate.

The logarithm plot of crack growth rate (da/dN) versus stress intensity factor range (ΔK) is usually sigmoidal in shape. The shape can be separated into three main parts as illustrated in Fig 2.4. The first part, known as the near threshold region is controlled mainly by the microstructure and the mean stress. Below this, there exists no discernible crack growth. The second part is the linear region, also referred to as the Paris region. The linear region is characterized by a

correspondence of the FCG to a stable macroscopic crack growth. The environment controls the two regions. The third one is the region marred by a very high FCG at the point when it nears instability and point of fracture. It is mainly controlled by the fracture toughness, responsible for the little FCG life involved. The region II or the Paris region is the one that this proposal builds most of the concern. The region II utilizes the relationship between cyclic da/dN, and ΔK to explain the crack growth behavior [20]. Region 1 denotes a period of slow growth, the second one denoting that of stable growth and region III denoting unstable growth as indicated in Figure 2.4.

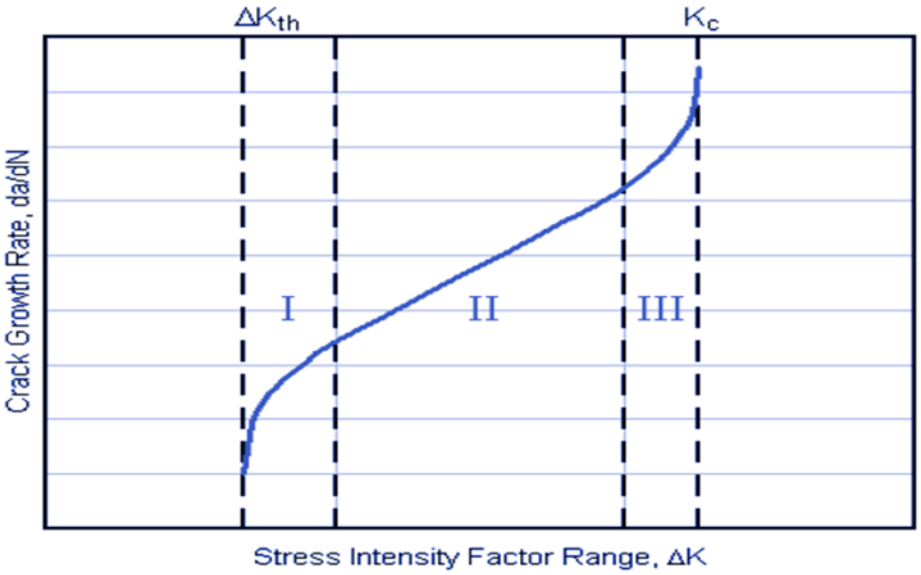

Figure 2.4: Three regions of fatigue crack growth rate [57].

The Paris equation (2.4) is often used by researchers following its proposal in the 1960s. It is used to denote stable crack growth. In the equation, C represent the coefficient of the growth of fatigue crack while m, is the exponent of FCG which often ranges between 2 to 7. Most values of m fall between 3 and 4 [58]. ΔK is the stress intensity range (K_{max} - K_{min}) where K_{min} and K_{max} represent the minimum stress intensity factor and maximum stress intensity factor values respectively.

$$\frac{da}{dN} = C\,(\Delta K)^m \qquad [2.4]$$

The region II, is often linear in the logarithm scale, and denotes the central part of the crack growth curve. The crack propagation in this region is addressed by the linear elastic fracture

mechanics (LEFM) condition. Ripples or striations whose spacing may be correlated to average crack growth rates characterizes the fracture surface in this region [59]. Region III exhibits a more rapid fatigue crack growth than that predicted by the Paris law as the ΔK increases, towards the value of fracture toughness (K_C). Forman et al. [60] modified the Paris equation (see [2.5]) to highlight the effect of stress ratio as the crack grows: R [2.6] is the stress ratio which is defined as the minimum stress intensity factor (K_{min}) divided by the maximum stress intensity factor (K_{max}) [60]. The relationship below accounts for the effects of stress ratio, while the Paris law assumes that da/dN is dependent on ΔK only.

$$\frac{da}{dN} = \frac{C(\Delta K)^m}{(1-R)K_c - \Delta K} \quad \text{..... [2.5]}$$

$$R = \frac{K_{min}}{K_{max}} \quad \text{..... [2.6]}$$

2.5.3 Crack Closure.

The fatigue crack closure is an essential factor used to detect the growth rates of cracks especially near the threshold region. It implies that the current propagation rates can be influenced by the conditions of the prior loading history and conditions in the wake of the crack [61]. Such is mostly evident in oxide particles in aluminum causing crack closure. Voluminous oxides formation on crack surfaces results in the occurrence of oxide-induced crack closure [62]. The oxide being harder than the aluminium means that it will push the crack open. The areas adjacent to crack growth threshold and having small crack openings experience significant oxide induced crack closure.

The Paris model fails to incorporate the effects R on the crack propagation. Thus, Elber proposed the concept of crack closure and the ΔK_{eff} (effective stress intensity factor range) in an attempt to demonstrate the R effects [63]. According to Elber's model, a portion of the crack front remains in contact during each loading cycle. ΔK_{eff} represents the stress intensity factor that the crack front remains open. Consequently, the stress ratio has an effect on ΔK_{eff}, making it possible to obtain the results of the constants C and m independent of R. Equations 2.7 and 2.8 show the modified formulas:

$$\frac{da}{dN} = C\,(\Delta K_{eff})^m \quad \text{..... [2.7]}$$

$$\Delta K_{eff} = K_{max} - K_{cl} \quad \text{..... [2.8]}$$

As demonstrated in equation 2.8, K_{max} denotes the maximum value of stress intensity factor while K_{cl} denotes crack closure stress intensity factor. Wide acceptance of the model has promoted the basis of the crack closure effect, explaining the effect of R on crack growth. Evaluating the effective ΔK using the experimental formula from Elber's model [63] leads to the existence of equations 2.9 and 2.10 shown below.

$$\Delta K_{eff} = U \times \Delta K \quad \text{..... [2.9]}$$

$$U = 0.5 + 0.4R \quad \text{..... [2.10]}$$

Combining Equations 2.7 to 2.10 the FCG rate can be expressed as shown in equation 2.11.

$$\frac{da}{dN} = C\,[(0.5 + 0.4R)\,\Delta K]^m \quad \text{..... [2.11]}$$

2.5.4 Fatigue Crack Growth Properties of 2xxx Aluminium Alloys

Fatigue failure is recognized to be a key factor in aviation crashes [64, 65]. The required characteristics of AA 2014 include high stiffness, fracture toughness, and excellent ductility. Higher ductility makes the material less responsive to stress concentrations under cyclic loading, prolonging the crack initiation period. Because crack initiation is a key contributor to fatigue life, this results in a prolonged fatigue life under low stress [66]. Quantitative analysis and thorough understanding of crack initiation and propagation behaviour is crucial in determining fatigue life of aluminium alloys. During cyclic loading, multiple crack nucleation sites occur in aluminium alloys [67, 68]. In 2xxx and 7xxx series, multiple fatigue cracks initiate in the coarse iron containing particles due to strain/stress concentration in these particles. The iron and silicon containing particles are the coarse constituent particles in high strength aluminium alloys [69]. Iron containing precipitates such as Al_7Cu_2Fe are relatively brittle.

During extrusion and rolling the precipitates fracture resulting in pre-cracks which act as crack initiation sites in the material [70-72]. Several crack initiation processes occur within the welds and the HAZ with separately distinct implications on the fatigue performance of welded structures [73]. Researchers [73] investigating the effect of residual stress on fatigue

performance of welded aircraft structures reported that, although crack initiation was found in the FZ, cracks forming at the peak of residual stresses were located in the heat affected zone. The low hardness in the heat affected zone and highest residual stress of 264 MPa in the longitudinal direction was found to be detrimental to fatigue performance in AA 2024-T351 aluminium alloy joints [74].

Hatamleh [75] revealed that residual stresses play a significant role in crack growth. Despite the fact that the friction stir welding technique produces relatively modest residual stresses in the welds when compared to fusion welding, they had a significant impact on FCG. In general, the behavior of crack growth in friction stir welded coupons is influenced by microstructure, residual stresses, and specimen shape. When compared to the base material, the findings of this investigation showed a substantial reduction in fatigue crack growth rates utilizing laser peening. Figure 2.5 shows FCG rate versus SIF range for high strength aluminium alloys as studied by Doglione and Bartolone [76]. This study led to the following points; crack growth resistance of AA 2014 alloy is comparable to that of the classical competitors i.e. the 2xxx and 7xxx series alumimium alloys. Crack growth occurs crystallographically in mixed mode I and II, with very tortuous path; important stress ratio effects manifest in the threshold region, ΔK_{th} decreases as R increases; crack closure is the main cause of stress ratio effects until R = 0.6; and further decrease in ΔK_{th} occurs beyond R = 0.6 apparently without crack closure.

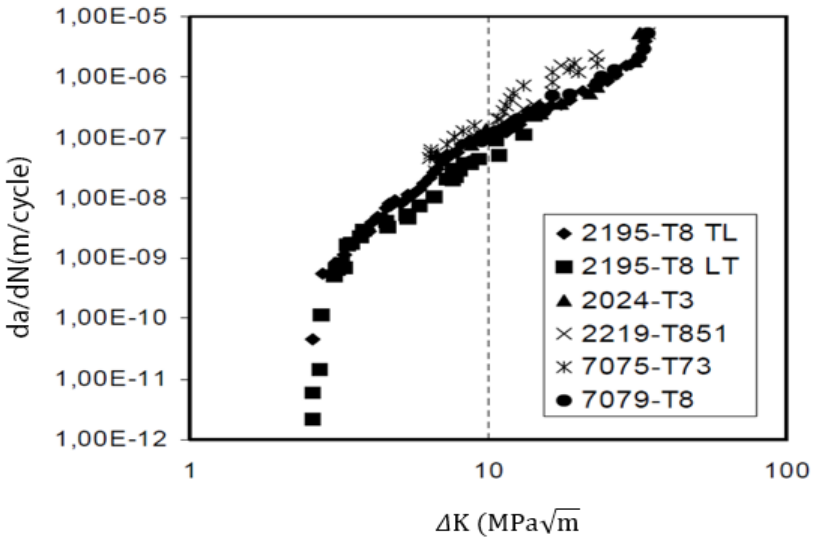

Figure 2.5: Fatigue crack growth rate vs SIF range for high strength aluminium alloys [76].

Sharma et al [77] investigated the fatigue behaviour of AA 2219 alloy under various aging circumstances. They established that the alloy was most resistant to fatigue crack formation when it was naturally aged. Fatigue crack resistance was better in the underaged condition, followed by peak aged condition, while the overaged condition had the least resistance to FCG. With advanced age circumstances, the rate of crack growth rose while the threshold stress intensity factor dropped. The fracture morphology changed dramatically from crystallographic facets at the threshold area to a region with well-developed ductile striations. Studying the fatigue behavior of high strength AA 2524-T34 alloys, Zheng et al [78] observed that the presence of second phase particles significantly impacted fatigue crack initiation and propagation. The deflection of cracks revealed obvious crystallographic characteristics, suggesting that grain orientation is important in regulating FCG in the alloy.

2.6. Effect of Welding on Fatigue Crack Growth (FCG) Characteristics.

Metallographic investigations using optical microscopy and scanning electron microscopy [79] revealed that it is possible to split the cross section of the weld into three zones namely: nugget zone (NZ), thermo-mechanically affected zone (TMAZ), and HAZ [80, 81]. The material in the NZ region experiences rapid recrystallization and a strengthening phase redistribution, according to the analysis of each zone. The existing cracks vanish as the microstructure is transformed into finer equiaxed grains [82]. According to Hrishikesh et al [83], materials whose grains are fine exhibit better mechanical properties, offer a better resistance to fatigue crack growth and display higher tensile properties. Examining the TMAZ on either side of the joint material welded with friction stir method showed a clear contour boundary for the advancing side and a fuzzier contour boundary for the retreating side. This phenomenon is thought to be connected to the direction of material movement [81]. The HAZ is positioned between the TMAZ and the BM. Thermal cycling is the only factor affecting the HAZ, resulting in the strengthening precipitates becoming coarse and hence reduced yield and final strengths [84, 85].

Welded components and machine parts find applications in areas where the stress is constantly varying in magnitude and direction. Research has shown that welding has a substantial effect on the microstructure of the base metal which in turn affects the fatigue properties [86]. Fatigue

damage is generally described as nucleation and growth and nucleation of the small cracks to the final failure [57]. It is widely accepted and proven in research that the initiation stage is absent in welded structures generally due to micro-imperfections in welds [87, 88].

GMAW and GTAW are commonly used to weld high strength Aluminium alloys such as AA 2014. The tendency of the weld metal and the HAZ to lose strength is caused by the strengthening precipitates' dissolution during welding just as the high cooling rates after the weld cycles do not favor re-precipitation [89]. In aluminium alloys, zinc quickly changes into an oxide during the welding process, which affects the weld pool's surface tension and increases the dangers of defects due to the absence of fusion [90]. The problem can be solved by using a current which is ~10-15% higher than that used in welding 5xxx alloys [90].

High deposition rates, high welding speeds and deeper penetration are achieved in GMAW due to the high heat input. However, a high heat input is detrimental to welding of thin aluminium sheets since it causes distortion and increases the width of the HAZ [70]. Alloying elements such as magnesium may be oxidized during welding and the loss of magnesium is worst during GMAW [91]. Grain refinement in GTAW increases the resistance to fatigue crack growth [92]. The heat input can be controlled precisely during the pulsed GTAW process. GTAW is therefore preferred over GMAW as it produces good quality welds [92-94]. The pulsing of welding current leads to grain refinement in the FZ, HAZ width reduction, reduction of residual stresses and hot cracking sensitivity [92, 95].

Ma et al [96] investigated the mechanical characteristics and FCG rates in FSW nuggets of Aluminium-Lithium alloy joints made of 2198-T8. The researcher subjected both the BM and the welded nugget to fatigue tests with varying stress ratios. The results indicated a difference between the FCG rates in the nugget area and those of the parent material, which is sensitive to stress ratio. Additionally, the research showed the existence of striations on the fracture surfaces of the fracture of the welded nugget. The study of the fracture surface of aluminium alloy AA 2524 under loading due to fatigue indicated that fatigue cracks in this alloy nucleated at either one of two places, namely; the second phase particles and the continuous phase rich in aluminium [97]. The reported fracture mechanism includes the initiation and growth of microcracks as well as microcrack coalescence.

Yan and Fan [97] showed that grain boundaries can impact the direction of microcrack propagation. Shou et al [98] investigated how grain size influenced FCG in 2524-T3 alloy. They established that alloys whose grain sizes range from 50 μm to 100 μm have faster fatigue crack growth rates. Fatigue cracks spread in a more convoluted way in the alloy whose grain sizes range from 50 μm to 100 μm, according to fractography studies. Wu et al [64] studied the behavior of an Aluminium-Copper-Lithium alloy under fatigue and established that grain boundaries were not capable of preventing the development of fatigue cracks owing to the grain boundaries having coarse second phase particles along them. Fatigue crack propagation at grain boundaries is reduced hence a better fatigue crack growth life.

2.7 Low Cycle Fatigue

Low cycle fatigue is a kind of fatigue induced by significant plastic stresses in a limited number of load cycles prior to failure. The high stresses in LCF that exceed the material yield strength are caused by either thermal or mechanical loading. In the event that the stresses surpass the yield strength, significant plastic deformation takes place. Cracks that cause LCF mostly initiate from regions with high concentration of stress/strain. Microscopic cracks of a particular depth or length, or a total component fracture are some of the failure criteria of LCF [99]. The LCF regime is distinguished by high cyclic stress levels that exceed the material's endurance limit, which is usually believed to be between 10^4 and 10^5 cycles. In general, LCF data is shown by a plot of the total strain range, versus the number of cycles before failure, N_f, or the plastic strain range, versus N_f in log–log scale [100]. LCF tests are performed in much the same way as high cycle fatigue (HCF) testing. However, the exception is that for LCF, the strain range is kept constant. Upon plotting the log to log graph of plastic strain amplitude, $\Delta\varepsilon_p/2$, against the number of load reversals to failure, $2N_f$, both Coffin [101] and Manson [102] established a linear connection, as indicated in Equation 2.12.

$$\frac{\Delta\varepsilon_p}{2} = \varepsilon_f' (2N_f)^c \quad \text{[2.12]}.$$

where $\Delta\varepsilon_p$ denotes the plastic strain range and N_f denotes the number of load cycles required to attain fatigue failure. In the stress–strain hysteresis loop, N_f is the number of reversals to failure.

The material constants ε_f' and c are empirical. The fatigue ductility exponent, c, typically ranges from -0.5 to -0.7. When the temperature rises, the value of c becomes more negative [99]. ε_f' denotes the fatigue ductility coefficient, which is often closely connected to the material's fracture ductility. From equation 2.12 it is evident that a rising plastic strain results in a falling number of cycles and a small value of c indicates long fatigue life [103]. Equation 2.13 expresses the Basquin relationship [104] between the stress amplitude in a completely reversed non-changing amplitude fatigue test and the number of load reversals prior to failure, $2N_f$.

$$\frac{\Delta\sigma}{2} = \sigma_a = \sigma_f' (2N_f)^b \quad \text{[2.13]}$$

where σ_f'denoted the fatigue strength coefficient and b is the Basquin exponent or the fatigue strength exponent. Since it is possible to express the value for the total strain amplitude, $\Delta\varepsilon_t/2$, in terms of plastic strain amplitude and elastic strain amplitude, $\Delta\varepsilon_e/2$, equation 2.14 can be derived as shown below.

$$\frac{\Delta\varepsilon_t}{2} = \frac{\Delta\varepsilon_e}{2} + \frac{\Delta\varepsilon_p}{2} \quad \text{[2.14]}$$

Mason [102] later proposed a more general connection (equation 2.15) by considering both plastic and elastic strains, i.e. the total strain, as an indication of failure due to LCF. The strain life illustration for the component on a log to log scale as constructed using Equation 2.15, is illustrated in Figure 2.6. Larger plastic stresses, in general, result in shorter life. Improved ductility of the material can enhance the LCF life. However, higher material strength can on occasion shorten the life of the component especially in the event that it is prone to LCF failure since ductility is often lowered by higher material strength [99].

$$\frac{\Delta\varepsilon}{2} = \varepsilon_f' (2N_f)^C + \frac{\sigma_f'}{E} (2N_f)^b \quad \text{[2.15]}$$

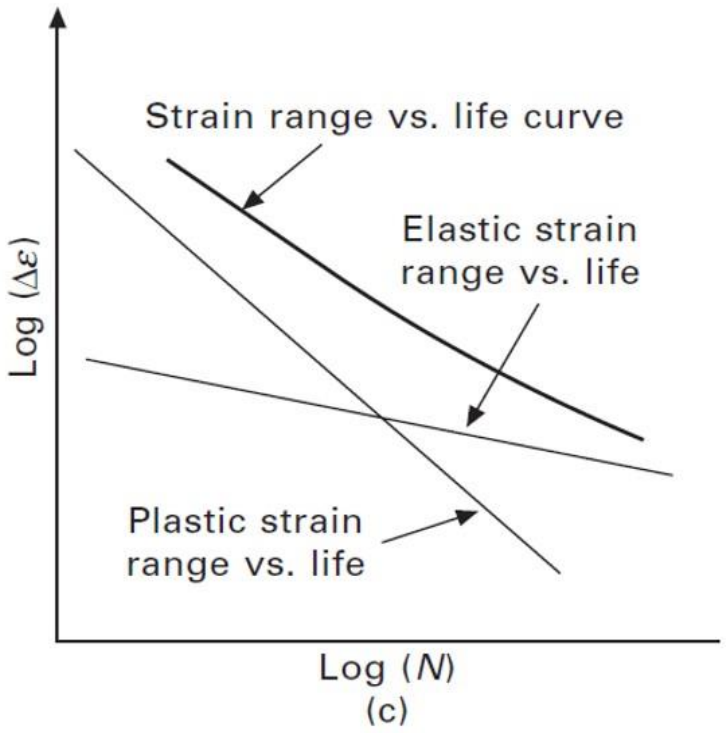

Figure 2.6: A Graph of Total Strain Range Vs Life in LCF [99].

The material typically undergoes some plastic deformation throughout the LCF process. The coherent ordered precipitates that are widely dispersed in the binary aluminium-copper alloy are vulnerable to shearing due to dislocation, and additional dislocations prefer to migrate along the already existing slip planes, resulting in planer slip [105]. Furthermore, strain localization can be an outcome of both coarse inclusion particles and grain boundary precipitate free zones (PFZs) which result in the alloy's heterogeneous microstructure and local plastic deformation. This heterogeneity is linked with the formation of micro-voids and micro-cracks, resulting in fatigue resistance deterioration [106-112].

Szusta and Seweryn [113] studied the LCF behavior of 2024-T3 under multiaxial stress at high temperatures. The fatigue life of 2024-T3 aluminium alloy at high temperatures increased due to the increase in the phase shift between torsional loading and tensile loading progressions. Hao et al [114] studied the microstructural characteristics and effect of strain ratio on fatigue response of AA 2121-T851. In this study, it was established that length and density of the slip bands influence the strain ratio values. The authors demonstrated that greater slip band density and

length resulted in increased strain ratios at 0.6 percent strain amplitude. Moreover, it was demonstrated that when strain ratio increases, the size of coarse components and the volume fraction increase. The loss in fatigue life of the material was linked to the consequences of these alterations in microstructures.

Lewandowska et al [111] examined the precipitate impact on the low cycle fatigue property of alloys of aluminium-copper and established that adding copper introducing T_1 phase may contribute to a more uniform plastic deformation of the alloys under cyclic loading and increase its low cycle fatigue life. Liu and Wang [115] investigated the LCF properties of 8090 Al–Li alloys that had been heat treated and angular pressed under equal-channel. They proposed that for heat-treated samples, the amount of intergranular failure in high strain amplitude is much higher than that in intermediate strain amplitude. They also established that there were no apparent differences in the fatigue fracture mode between high and intermediate plastic strain amplitude for equal channel angular pressing. According to Wang et al [116] adding scandium (Sc) may significantly alter the Al–Li alloys' microstructure. The alteration included the precipitation of phases containing Sc and the promotion of the S′ phase, resulting in a fall in planar slip propensity and a rise in LCF life.

There exists a strong link between a materials' LCF behavior and the feature of precipitated phases in other Al alloys that are results of age-hardening such as Al–Li alloys. Han et al [117] investigated cyclic deformation behavior and the evolution of dislocation structure of an alloy of aluminium-copper containing precipitates exhibiting properties of shear-resistance. This study [117] proposed a cyclic slip irreversibility expression dependent on both the state of the precipitate and the amplitude of the plastic strain. Hockauf et al [118] studied how precipitate morphology affected the low cycle fatigue and FCG behavior of ultrafine-grained AA 6060. The research disclosed that freshly generated coherent precipitates during the process of thermal recovery are likely to result in more evident planar slip and strain localization, thus a decrease in LCF life.

2.8 High Cycle Fatigue

High cycle fatigue results from low elastic strains as a result of a high number of load cycles prior to failure [99]. The stress originates from a mix of both mean stresses and alternating stresses. On the one hand, the mean stress is an outcome of the residual stress while the alternating stress is mechanical stress, at any frequency, or a thermal stress at similar conditions. Alternating stress is a thermal or mechanical stress at any frequency. The cyclic cylinder pressure load is a common loading parameter in HCF. HCF involves a large number of loading cycles before fatigue failure, which is caused mostly by elastic deformation. In HCF the stresses as compared to low cycle fatigue, are also below the yield strength of the material. The high cycle fatigue does not often exhibit as much macroscopic plastic deformation as LCF.

According to Suresh [59], the methodologies for quantifying high cycle fatigue in terms of nominal stress amplitude arose from the work of Woehler (1860) while working on fatigue of alloys in railroad bogie axles. Fatigue data is often given in the traditional representation of strain life or stress life (S-N) curves, as pioneered by Woehler. The S-N curve is a graphical representation of the loading cycles that a specimen can endure before failure. The test specimens are cut to produce a waisted cylindrical gauge length for testing in rotational bending mode.

There are specific materials that exhibit a “knee” in a plot of S-N curve as shown in Figure 2.7. Materials such as mild steel behave in that manner especially when we assume that the specimen has infinite life [119]. The behavior is seen in an asymptotic decrease in the curve to a horizontal constant value for the amplitude stress. Many alloys of copper and steel exhibit the endurance limits of between 35% and 50% of the tensile strength [120]. However, several high strength alloys of steels and aluminium alloys do not show a fatigue endurance limit which is therefore found as the stress amplitude that the specimen can support for a minimum of 10^7 cycles of fatigue [59].

In most engineering designs the assumption is made that any cyclic stress below the fatigue limit does not affect the component. Recent studies [121] have, however, indicated that failure due to fatigue in aluminium alloys can take place at 10^9 fatigue cycles, which contradicts the work of Woehler. High strength AA 2014 aluminium alloys used in the aircraft or automotive industry

are subjected to high cyclic loading in service, involving high frequency vibrations. Whereas it is time consuming and impractical to undertake fatigue tests to the gigacycle regime, most components and structures in service are often loaded beyond 10^8 cycles [122].

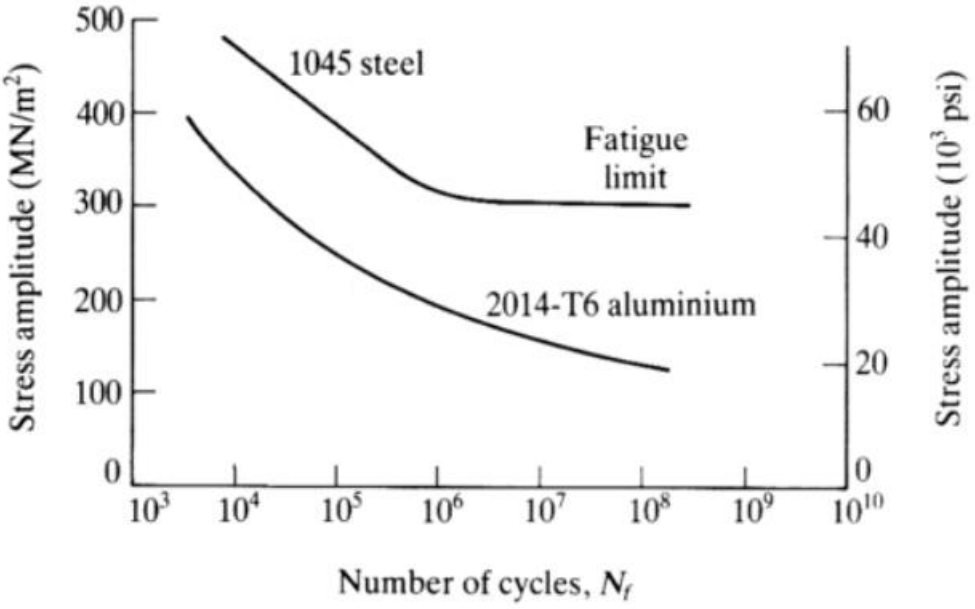

Figure 2.7: The S-N curve of 1045 steel and 2014-T6 aluminium alloy [99].

Fares et al [123] examined the combined influence of substrate microstructure and sulfuric process anodizing on the performance of an aluminium alloy AA 2017A-T4. It was concluded that the presence of an anodic layer has no discernible impact on the fatigue cracks development in the alloy at high alternating stresses for both microstructural situations. Nonetheless, the findings obtained at modest alternating loads indicated that anodizing considerably decreases the alloy's fatigue life for both microstructural situations. The favored breakdown of the matrix surrounding the cathodic particles was ascribed to the shorter fatigue life (such as Al_2Cu). As a result, cavities formed, which functioned as stress concentrators, encouraging the production of numerous fatigue microcracks.

2.9 Effect of Welding on the Fatigue Strength.

The process of welding introduces porosity and reduces the mechanical properties of welded metal [124]. The FCG life and fatigue strength in welded components are also reduced by the weld imperfections. Research has shown that undercuts and solidification cracks are more damaging than embedded porosity [125]. It was further demonstrated in the study [125] that decreasing the stress concentration and increase in fatigue strength could be achieved by improving the weld geometry. The welded structures' fatigue strength is reduced by bending stress, different mechanical characteristics of weld metal, residual stress and the HAZ. Plate thickness has a less substantial influence on stress intensity factor and fatigue strength than weld flank angle and weld toe radius [126].

The dissolution of strengthening precipitates during welding has been found to be the cause of softening and consequently the reduction of fatigue strength in welds [87]. Improvement of fatigue life can be done by shot peening, toe grinding, GTAW dressing and hammer peening. Relationship between fatigue life and size of the grain changes according to the mechanism of deformation. The size of the grain has the largest impact on fatigue strength under low stresses, high cycle regime, where stage I cracking is predominant. Cell structures form easily in aluminum alloy materials due to high stacking fault energy associated with them and this controls stage I crack propagation. [127].

The repair of welded joints with a secondary weld is not a certainty of a prolonged life of the joint beyond the initial welded joint. Heat input in the process of weld repair results in unusual coarse grains and weld porosity of the repaired weld plates' microstructure [125]. Furthermore, additional voids and porosity at the weld repaired plates' grain boundaries results in a faster rate of fatigue crack growth and shorter fatigue lifetimes for weld repaired specimens.

The Welding process reduces the mechanical properties of the base metal [128]. These properties are dependent on the microstructure change. Several workers have conducted research to unearth the role of grain size on toughness and hardness [129] indicating that the excess growth of the grain can result in fatigue strength reduction and increased crack growth and initiation. The weld metal fracture mode was found to change from ductile fracture (8.1kJ/cm) to brittle fracture

mode (6.5kJ/cm) with increase in heat input [129]. This was attributed to grain coarsening due to a high heat input which reduced the impact energy and toughness.

2.10 Summary of Literature Review

The presence of different micro-alloying elements and an adequate heat treatment causes the precipitation of different phases in aluminium alloys. Aging in aluminium-copper alloys is often initiated by the formation of very fine platelike Guinier–Preston zones in the aluminium matrix on {001} planes. Here, Guinier–Preston zones have a diameter of around 10 nm and are made up of single planes of copper atoms. Aging of the Guinier–Preston zones makes them develop into a cohesive θ" phase. Further aging occurs in sequential transformations to semi-coherent and, finally, plate-like θ-$CuAl_2$ particles. In the case where there is high Copper concentration (nearly 4 percent mass), θ precipitation sequence described in the literature is more likely to occur. The Q or S phase precipitation sequence is highly likely in the case of AA 2014 aluminium alloy, which is primarily a quaternary alloy of aluminium–copper–silicon–magnesium.

Aluminium alloys are susceptible to fault development during welding due to their strong affinity for ambient gases, high thermal and electrical conductivity, high coefficient of thermal expansion, low stiffness, and wide solidification temperature range. The creation of porosity, the coarse segregated microstructure formation and hot cracking, in the FZ are some prominent flaws that are experienced during fusion welding of 2xxx high strength alloys. Among the many techniques of fusion welding, gas tungsten arc welding is the best, producing reasonably clean and high-quality welds.

Due to the use of targeted heat input, welding of AA 2014 aluminium alloys results in dramatic microstructural changes. The resulting microstructure ranges from the typical grain structure to grains that are equiaxed and with a coarse dendritic columnar structure in the FZ, accompanied by considerable coarsening of grains in the HAZ. The size and the fraction of Al_2Cu precipitates in various zones are also changed as a result of precipitate dissolution and/or coarsening [38]. Microstructural changes, grain sizes, precipitate distribution, and fraction can all affect the electrochemical and mechanical properties of a weldment. The hardness in the HAZ has been found to decrease as the FZ is approached. This is caused by the coarsening of the precipitates,

segregation of the strengthening precipitates into the grain boundaries and the dissolution of strengthening precipitates. Microstructural regions with the coarse grains have been established to exhibit less resistance to FCG and also low fatigue strength compared to regions with finer grains.

The hardness of the HAZ decreases due to welding thermal cycles. The resulting microstructure in the HAZ is heterogeneous and the properties differ too. The weakest region in a weldment has been found to be in the HAZ in most of the research that has been carried out. The thermal conditions and the peak temperature experienced govern and play a part in the resulting metallurgical structure, mechanical properties, residual stresses and distortion. Regulating heat input during welding is critical for the optimization of the HAZ strength. Welding affects themechanical properties, microstructureand fatigue properties of the heat affected zone. Moreover, it is clear that the heat experienced by the HAZ is responsible for the observed changes. Since different parts of the HAZ attain different peak temperatures, it should be expected that the effects (on microstructure and properties) will be different in different regions of the HAZ. These differences have not been adequately addressed in the recent literature. Therefore, this study will aim to address this shortcoming by studying fatigue properties of BM and selected points in the HAZ of AA 2014.

As outlined in the literature review, LCF is caused by large plastic strains and few load cycles prior to the occurrence of failure. Component failure occurs as a result of crack initiation in regions with high stress/strain concentration. High stresses beyond the yield strength of the base material may be as a result of mechanical or thermal loading. Such stresses can occasionally surpass the yield strength, resulting in significant plastic deformation. It has been established that microstructural characteristics and strain amplitude has an effect on LCF life on 2xxx alloys. It is therefore necessary to investigate the impact that these properties have on the LCF life of AA2014 alloy.

High cycle fatigue results from low elastic strains as a result of a high number of load cycles prior to failure. In most engineering designs the assumption is made that any cyclic stress below the fatigue limit does not affect the component. A study by Mbuya [122] indicated that high cycle fatigue failure in aluminium alloys can occur at 10^9 fatigue cycles, which contradicts the

work of Woehler. High strength AA 2014 aluminium alloys used in the aircraft or automotive industry are subjected to high cyclic loading in service, involving high frequency vibrations. In order to determine the aluminium alloys' fatigue life, quantitative analysis and a detailed understanding of crack initiation and growth behavior are required. As a result, the HCF characteristics of AA 2014 aluminium alloy will be investigated

CHAPTER THREE: MATERIALS AND METHODS

3.1 Introduction

The experimental work that was undertaken involved: thermal simulation of heat flow condition during welding, three major tests (fatigue crack growth test, high cycle fatigue test and low cycle fatigue test) and two supportive tests (microstructural characterization (Optical) and hardness test). The main objective of carrying out this work was to investigate the fatigue properties in the base metal and at selected points across the HAZ of AA 2014. The tests that were carried out, equipment and materials used are discussed below.

The material used for this experiment was AA 2014. The material was purchased from Goodfellow Cambridge Ltd in the UK and was supplied in form of plates and rods. The plates were supplied as a 2.65 mm thick sheet 300 mm by 300 mm while the rods had a length of 1000 mm and diameter of 22.2 mm. The material was supplied in T6 temper condition from the manufacturer. T6 temper is achieved by a three-step process that consist of solution treatment, quenching and artificial aging. The artificial age hardening treatment process is carried out after solution treatment. The AA 2014 alloy is subjected to artificial age hardening treatment conditions without an active cold work process. This action makes the effect of cold processing very small. The chemical composition of the material in weight percent as provided by the supplier is given in Table 3.1.

Table 3.1: Chemical composition of the material tested (wt. percent).

Element	Al	Si	Fe	Cu	Mg	Mn
AA 2014	92.0	1.0	0.5	4.5	1.0	1.0

3.2 Tensile Test

Figure 3.1 shows the dimensions of the tensile specimen which was used for this test. Tensile tests were performed to confirm the mechanical properties of the AA 2014 supplied by the manufacturer. Three specimens as outlined in Figure 3.2 were prepared in accordance with ASTM E8M standard [130]. The specimens were cut in the longitudinal direction. The

Hounsfield tensometer shown in Figure 3.3 was used for tensile testing. This equipment was manufactured by Hounsfield Test equipment Ltd in England, UK. The tensometer has a capacity of 20 kN. The sample was loaded between two grips which were operated manually. The fractured AA 2014 specimen after carrying out the test is as shown in Figure 3.4.

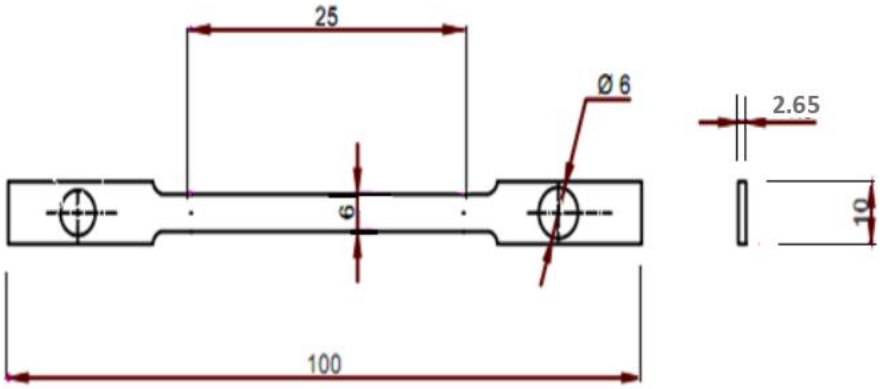

Figure 3.1: Tensile test specimen (Dimensions in mm) [130]

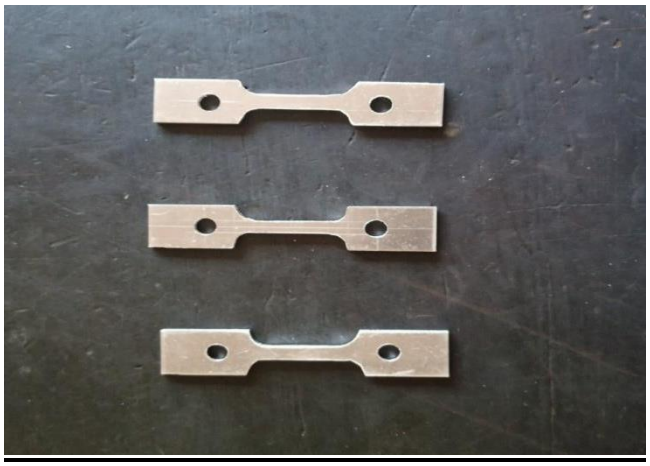

Figure 3.2: Prepared Tensile test AA 2014 specimen.

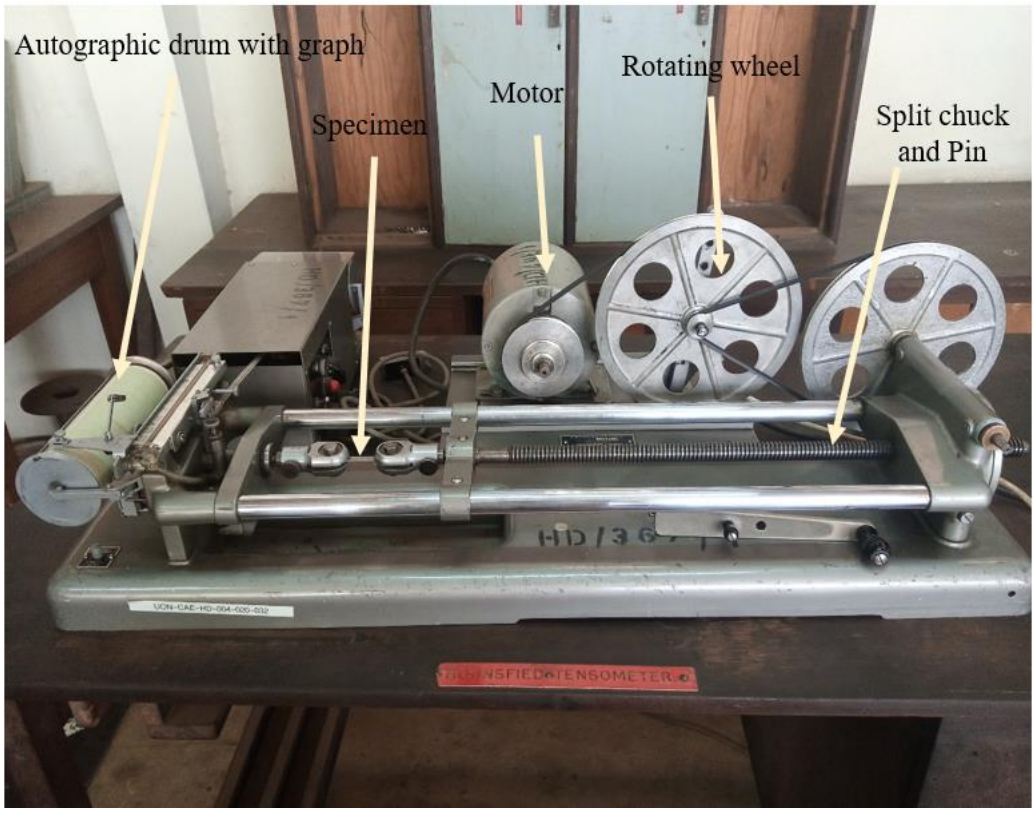

Figure 3.3: Specimen Loaded on Hounsfield Tensometer

Figure 3.4: Fractured AA 2014 specimen after Test

3.3 Thermal Cycle simulation

Thermal simulation done was one that resulted in as close as possible to the thermal cycle histories in Figure 3.5. The thermal histories had been obtained in an earlier study by Sakwa [16] by actual welding obtained using alternating current GTAW with the torch mounted on a carriage. In this study welding was done using a 2.6mm 2 percent thoriated tungsten electrode with a 50-degree tip with the arc gap preset to 2mm and the welding bead parallel to the direction of rolling. Other welding conditions were as shown in Table 3.2.

Thermal simulation of the specimen was done after the machining process of LCF, HCF and FCG specimens. The simulation process was done using a muffle furnace shown in Figure 3.6. The furnace has temperature adjustment knobs for adjusting heating rates and it had a peak temperature of 1200 ˚C. Specimens were put in the muffle furnace to simulate the two regions of the HAZ with peak temperatures of 590 ˚C and 650 ˚C representing region 5mm and 4mm respectively from the weld center line. For easy identity during this research, the specimens tested as supplied by the manufacturer were referred to as the BM and thermally simulated specimens (HAZ) at peak temperature of 590 ˚C and 650 ˚C were referred to as region C and region D respectively.

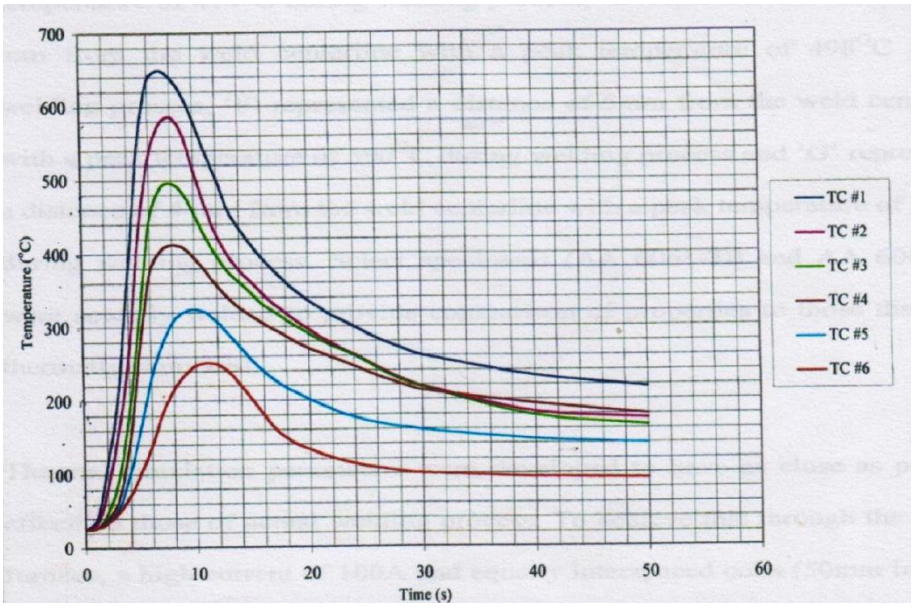

Figure 3.5: Thermal simulation cycles obtained by Sakwa [16].

Table 3. 2: Welding parameters by Sakwa[16]

Welding speed	3.2 mm per second
Feed rate	11.35 mm per second
Process	Gas Tungsten Arc Welding
Polarity	Variable
Position	Horizontal
Feed	Manual cold wire feed process
Current	75A
Voltage	20V
Shielding gas	12 l/min Pure Argon
Filler alloy	2.46 mm Dia.A1S1 4043
Electrode	2.6 mm Dia. Tungsten 2% Thorium

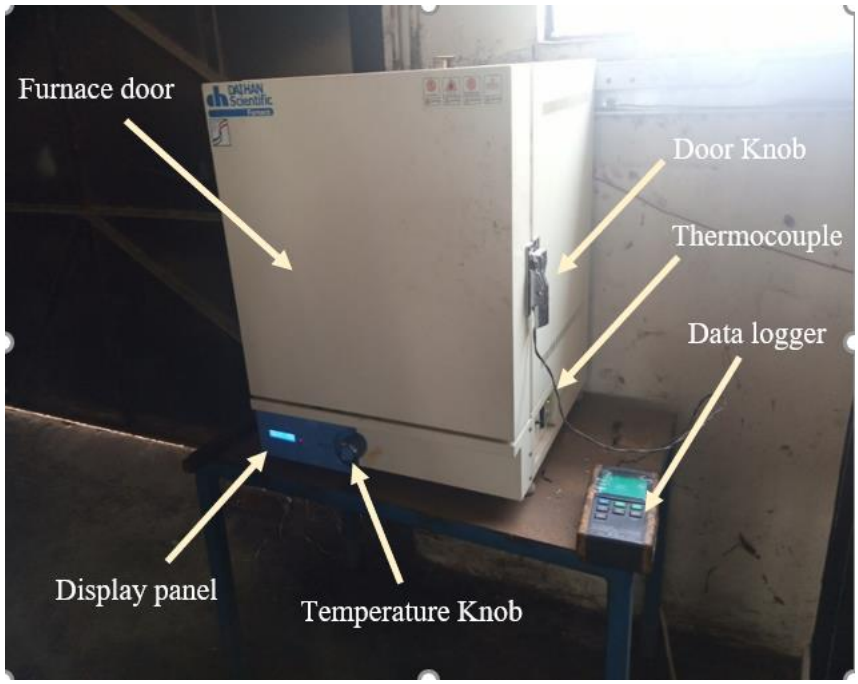

Figure 3.6: Muffle Furnace and Data logger used to monitor temperature of the specimen

The residual stresses were assumed to be negligible since the whole specimen was inserted in the muffle furnace. The specimens were quickly removed after attaining the targeted peak temperature and left to cool at room temperature. The use of a thermocouple and data logger was employed for accuracy in monitoring the temperature of the specimen in the muffle furnace. A 12 Channels Temperature Recorder with SD card Data Logger (Figure 3.7) and thermocouples type E made of chromel and constantan were used. The thermocouple connected to a data logger was attached to the specimens and temperature recorded. The temperature was monitored continuously at intervals of 2 seconds.

Figure 3.7: The12 Channels Temperature recorder with SD card Data Logger

3.3 Fatigue Crack Growth Testing

3.3.1 Fatigue Crack Growth Testing Equipment

FCG test was conducted using a test rig machine designed and constructed at the University of Nairobi mechanical engineering workshop by Rading [131]. The crack growth test rig is illustrated in Figure 3.8. The test rig has a cam operated eccentric arm mechanism. It comprises load arms like those commonly used in tensile testing machines. One of the load arms is connected to a 5,000 N capacity load cell. The second load arm is connected to the cam mechanism for holding the specimen. During the test the cam was driven by a 4 kW, 1,498 rpm motor. The eccentric arm connected to the cam converted the rotary motion of the motor into oscillatory motion of the driving force. The load was applied by tightening the nut located on one of the load arms. The load applied was displayed on a control panel fitted to the machine. The

growth of the crack was measured using a travelling microscope accurate to 0.1 mm. More details of the crack growth test rig and assembly drawings are documented in the reference [131].

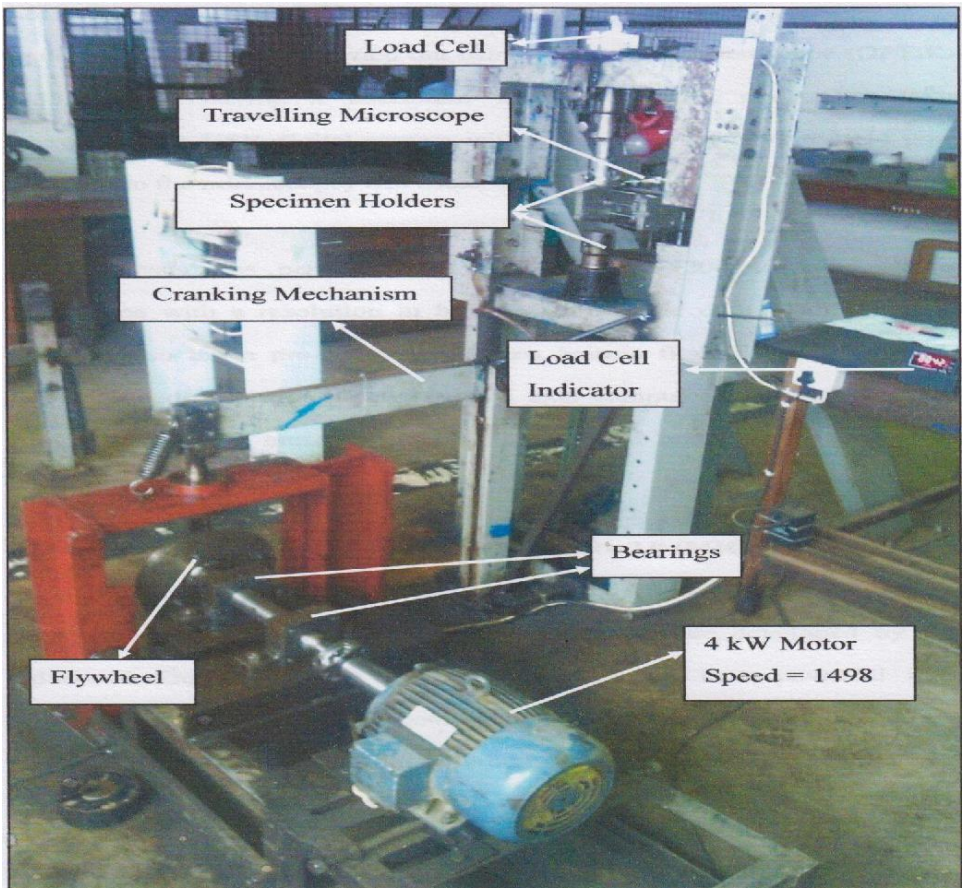

Figure 3.8: Fatigue crack growth test rig [132].

3.3.2 Fatigue Crack Growth Testing Specimen

Specimens used for this test were standard center cracked tension (M(T)) specimen prepared in accordance with ASTM E 647 [133]. This specimen is as illustrated in Figure 3.9. The M(T) specimen indicates a center crack specimen with a possibility of being loaded in a number of ways, namely: in either tension-compression or tension-tension. The crack length, a, was measured from the perpendicular bisector of the central crack. The machined notch, $2a_n$, was centered with respect to the specimen centerline to within ±.001W. For the M(T) specimen, the width, W, and the thickness, B, were independently varied within the following limits, all based

on specimen buckling and via thickness and crack curvature considerations. For the M(T) specimen the following was required:

$$(W - 2a) \geq 1.25\ P_{max} / (B\sigma_{YS}) \ldots\ldots\ldots\ldots\ldots\ldots\ldots\ldots\ldots\ldots\ldots\ [3.1]$$

In equation 3.1, (W – 2a) represents the specimen's uncracked ligament, B is the specimen thickness, P_{max} is the maximum load and σ_{YS} is equal to 0.2 percent offset yield strength which is determined at the same temperature as used when measuring the FCG rate data. The edges of the pre-crack were polished to have a smooth scratch free surface so as to enable the viewing and measurement of the crack length as it progresses during the fatigue test. Three specimens were prepared for each region of the HAZ and the BM. The types of fixtures and grips for clamping the M(T) specimens was a bolt and keyway design given in Figure 3.10.

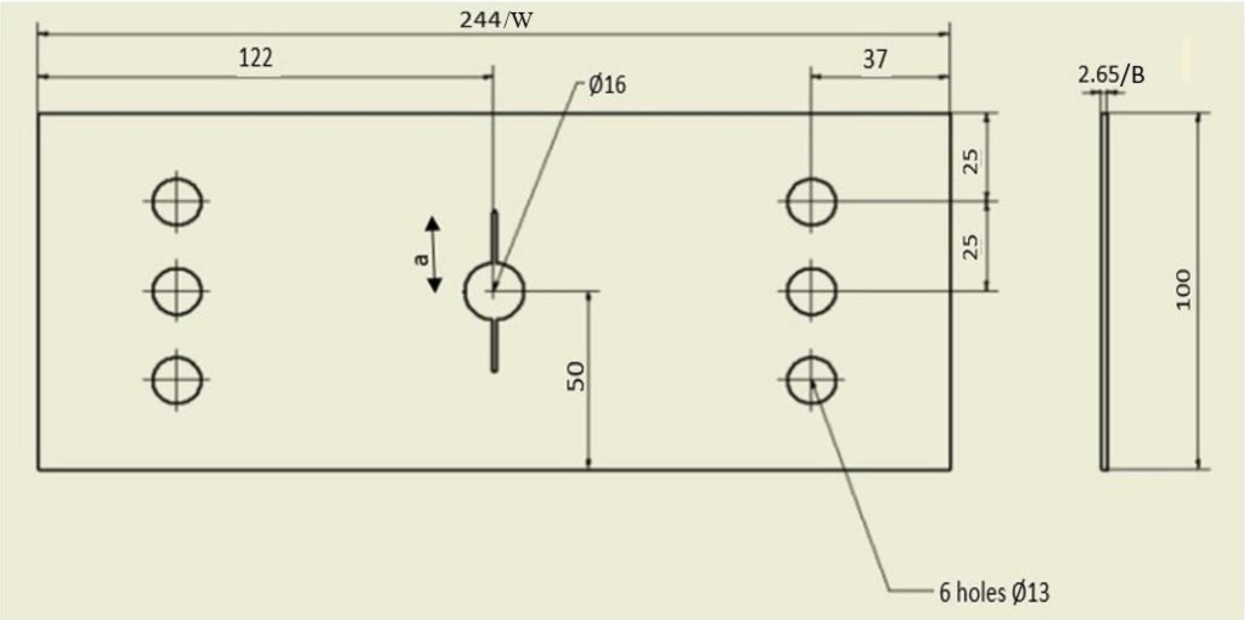

Figure 3.9: Center Cracked Tension specimen for fatigue crack growth tests (mm).

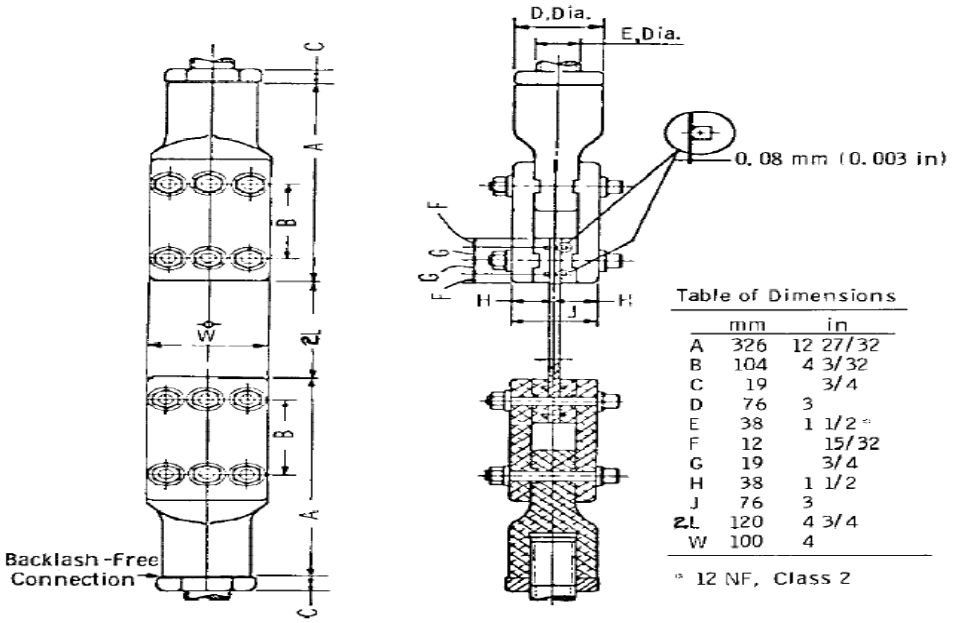

Figure 3.10: Bolt and Keyway Assembly for Gripping 100mm wide M(T) Specimen [133].

3.3.3 Fatigue Crack Growth Testing Procedure

The procedure followed was according to the ASTM E 647 procedure [133]. The fatigue crack growth test for this experiment was set to give a small stress ratio R, equal to 0.2. There were two experiments carried out during the FCG test. The first experiment was the constant load test and the second experiment was the decreasing load test. The constant load test was carried out to determine values of m and C while the decreasing load test was done to determine the threshold value of the stress intensity factor, ΔK_{th}. The decreasing load test was carried out by decreasing ΔP by not more than 10 percent after every three successive readings according to the ASTM E-647 standard [133]. The eccentricity of the fatigue test rig wheel was set at the neutral point. The prepared specimen with 2a crack of length 40 mm was loaded on the fatigue rig machine. The value of P_{min} was set. The eccentricity of the wheel was increased until a value of P_{max} that would result in a load ratio equal to 0.2 was achieved. The time (minutes) taken for the crack to grow and crack length (mm) were recorded.

Both secant and graphical methods were employed to determine the rate of crack growth, da/dN for this test. Using the secant method, da/dN, in mm/cycle was obtained as shown in equation 3.2

where, i represented the i_{th} data point, ‘a’ was length of the crack and N denoted the number of cycles [133]. The second method used to determine da/dN in mm/cycle was the graphical method. In this method, Graph software was used to plot a graph of ‘a’ vs N. ‘Graph’ is an application used to draw mathematical graphs in a coordinate system. A polynomial equation of order two was generated using the graph program. A graph of crack length, ‘a’ vs number of cycles N, was then plotted and the slope da/dN at any given point of the curve was determined. The corresponding stress intensity factor, ΔK, for both secant and graphical methods was calculated from equation 3.3 where ΔP denoted load range, W denoted the specimen width and B the specimen thickness. Fatigue crack growth curves for BM and two regions of HAZ were plotted. FCG parameters ΔK_{th}, C and m for the BM and the two regions of the heat affected zones were determined.

$$\frac{da}{dN} = (a_{i+1} - a_i) / (N_{i+1} - N_i) \quad \text{..... [3.2]}$$

$$\Delta K = \frac{\Delta P}{B}\sqrt{\frac{\pi\alpha}{2W}\,sec\,\frac{\pi\alpha}{2}} \qquad where;\ \alpha = \frac{2a}{W} \text{..... [3.3]}$$

3.4 Fatigue Strength Testing (HCF)

3.4.1 Fatigue Strength Testing Equipment.

A rotating bending fatigue testing machine SM1090 (Fig. 3.11) based at the University of Nairobi, department of mechanical and manufacturing Engineering, strength of materials lab was used for this test. It consists of two main parts: a main unit which has a motor responsible for rotating the specimen under constant stress, and a separate control and instrumentation unit. A coupler and a short driveshaft are rotated by the motor. The driveshaft rotates the collet type chuck, which applied uniform pressure around the circle of the test specimen's driving end. The consistent pressure was critical because it provided an even stress distribution on the specimen and gripped it with the least amount of eccentricity. Adjustable dead weight imposes a load(vertical) on the specimen at the loading end through a bearing that has a self-aligning mechanism. A sensor then counts the cycles (rotations) of the specimen. A load cell was used to

estimate the force that was applied on the specimen. A display panel showed the load, speed of rotations and the cycle count. Other apparatus that were needed to carry out the test included; Vernier calipers; Tommy bar; Spanner; Allen key and power supply. Data collected was monitored using a versatile data acquisition system as shown in both Figure 3.12 and Figure 3.13.

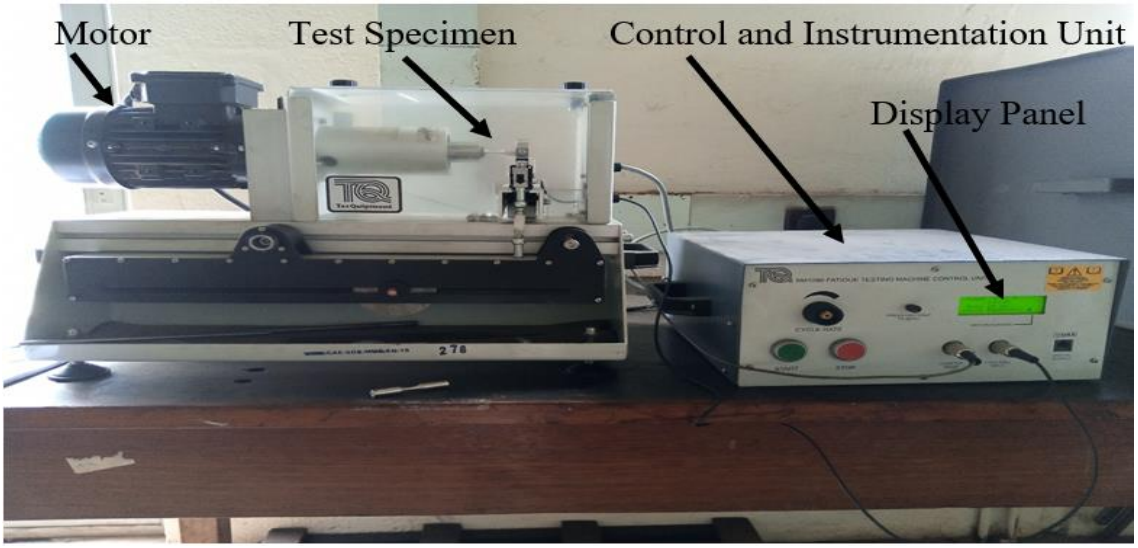

Figure 3.11:Rotating bending fatigue testing machine (SM1090).

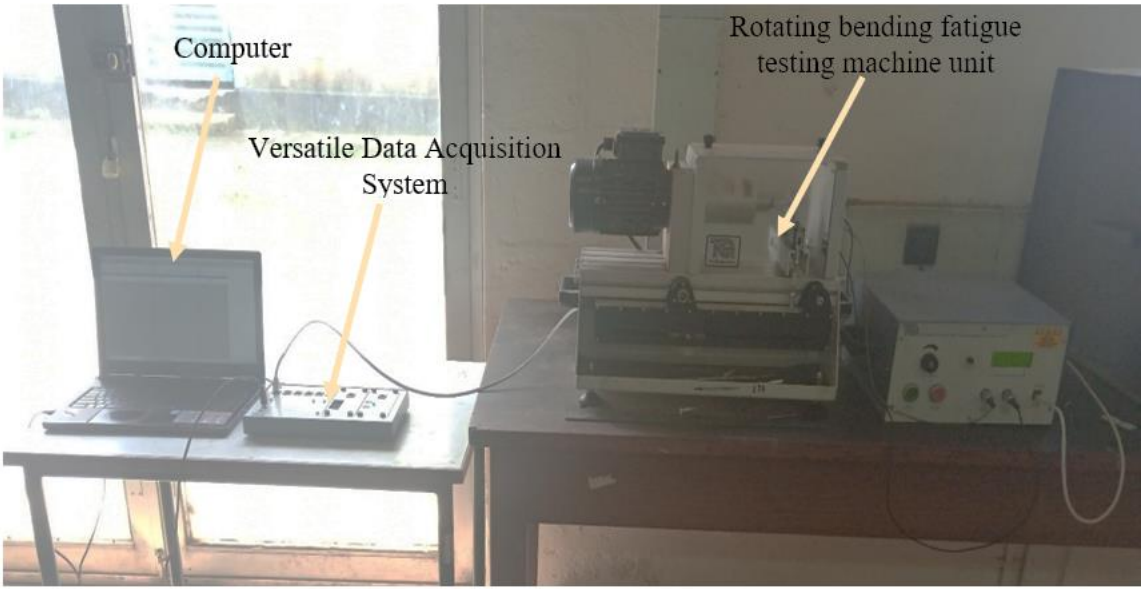

Figure 3.12: Rotating Fatigue Machine Connected to Versatile Data Acquisition System.

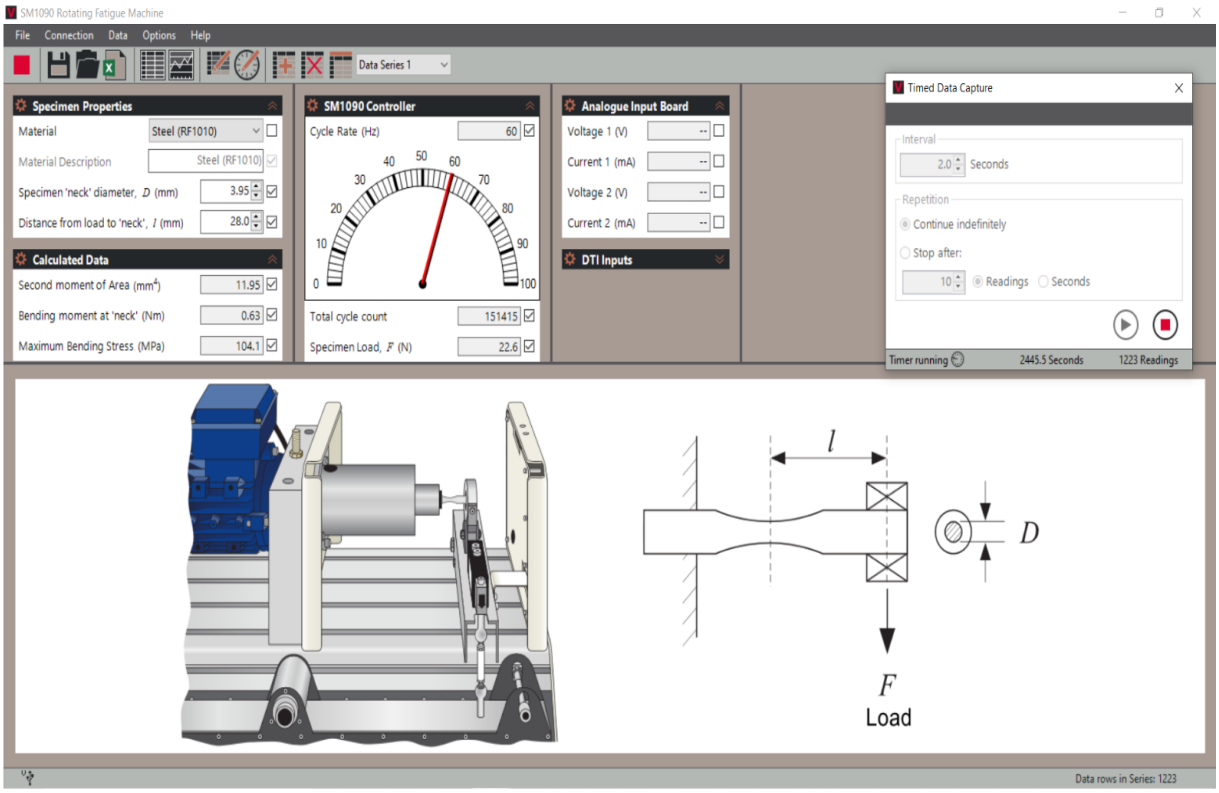

Figure 3.13: Versatile Data Acquisition System Layout.

3.4.2 Fatigue Strength Testing Specimens.

The specimens were machined at the Numerical Machining Complex Centre Ltd, Nairobi. The dimensions of the specimens used for this test are shown in Figure 3.14. Figures 3.15 and 3.16 show images of the specimen before and after the test. High cycle fatigue test was carried out to determine the approximate fatigue strength of AA 2014. The specimen was rotated by a motor and as the specimen rotated, a fibre on the surface of the specimen experienced a stress that varies from maximum (tensile) value to minimum (compressive) value. In effect the stress variation in the specimen was completely reversed (zero mean stress) sinusoidal variation. A load or stress value was chosen and the specimen rotated until it failed. The number of stress cycles N that causes the specimen to fracture was noted. This process was repeated for different values of stress.

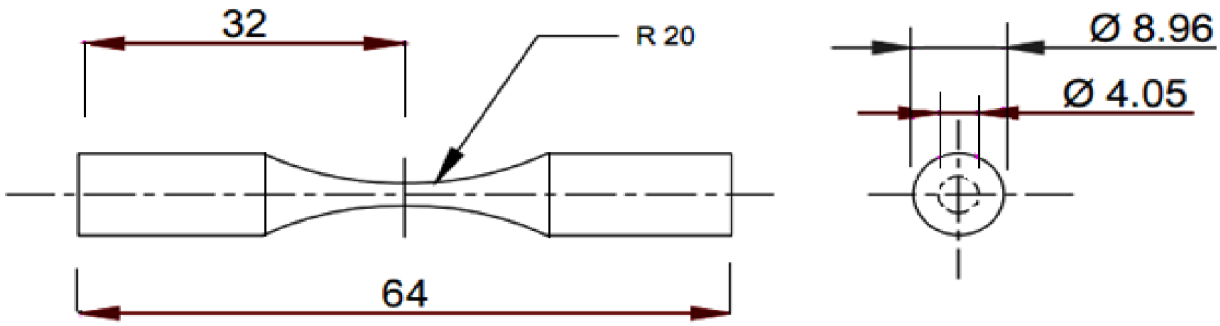

Figure 3.14: Dimensions of specimen for fatigue strength test (mm) [132].

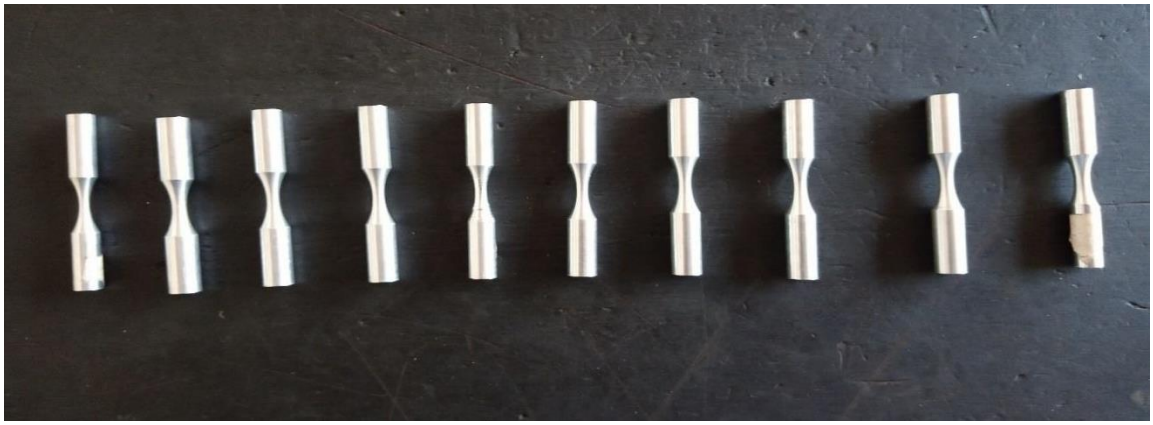

Figure 3.15: Machined specimen for the fatigue strength test.

Figure 3.16: Fractured specimen after fatigue strength test.

3.4.3 Fatigue Strength Testing Procedure.

Fatigue strength test was conducted using the staircase method under the conditions of room temperature and pressure and at a frequency of 60 Hz. For purposes of this study, the fatigue strength is defined as the alternating stress that causes the material to fail in 10^7 cycles. The step-loading procedure as described by Maxwell and Nicholas [134] was used to establish the sample's fatigue strength at 10^7 cycles. After choosing an initial stress for all the specimens, the test was done sequentially with a 7 % stress increment/decrement depending on the failure or running-out of the previous specimen. The 7 % step was chosen due to the stepwise nature of the testing machine. In the event of specimen failure prior to attaining 10^7 cycles, the level of stress for the next specimen was reduced, and likewise, it was increased if the specimen attained the 10^7 cycles without failing. The linear interpolation scheme as captured in equation 3.4 below [135] was applied in the approximation of the fatigue strength. To confirm the results a final test was run at this approximate fatigue strength value.

$$\sigma_e = \sigma_o + \Delta\sigma \frac{N_{fail}}{N_{life}} \quad \ldots\ldots\ldots\ldots\ldots\ldots\ldots\ldots\ldots\ldots\ldots\ldots [3.4]$$

Where: σ_e = Maximum fatigue strength corresponding to N_{life} cycles

σ_o = Previous maximum fatigue stress that did not result into failure

$\Delta\sigma$ = The step increase in maximum fatigue stress

N_{fail} = Cycles to failure at the fatigue stress ($\sigma_o + \Delta\sigma$)

N_{life} = Cyclic fatigue life = 10^7

Equation 3.5, which was used to determine stresses applied for predicting fatigue strength of AA 2014 was developed as shown below.

L = distance between the neck and point of load application = 0.028 m

F = load/ force in Newtons.

M = moment.

I = second moment of area about central axis.

d = diameter of the specimen (neck) in meters.

$$y = \frac{d}{2}$$

Therefore;

$M = FL$; $\sigma = \frac{My}{I}$; $I = \frac{\pi d}{64}$

Substituting we have;

$$\sigma = \frac{32FL}{\pi d^3} = \frac{0.2852F}{d^3} \ldots\ldots\ldots\ldots\ldots\ldots\ldots\ldots\ldots\ldots\ldots\ldots\ldots\ldots [3.5]$$

3.5 Low Cycle Fatigue Testing.

3.5.1 Low Cycle Fatigue Machine

A fatigue testing rig (Fig. 3.17) based at the University of Nairobi, department of mechanical and manufacturing Engineering, strength of materials lab was used for this test. The main components of the fatigue testing rig are: a load producing mechanism consisting of an AC motor (1400 rpm) connected to a belt and pulley system. Other components include load transmitting members consisting of connecting rods, eccentric center press fitted to bearings and a machine framework made of L shaped and square beams.

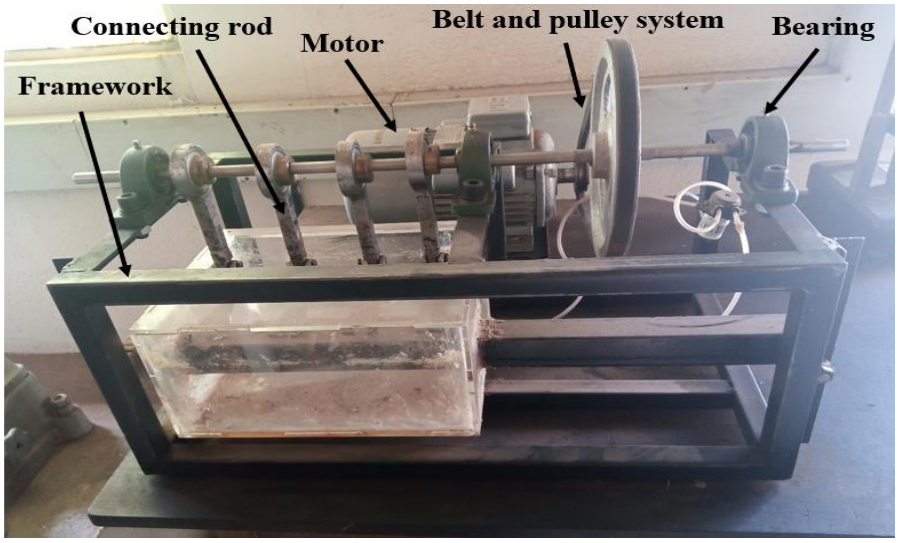

Figure 3.17: LCF testing rig

3.5.2 Low Cycle Fatigue Specimen Design and Testing

The dimensions of the specimen used for Low cycle fatigue test are shown in Figure 3.18. LCF specimens were prepared in the university of Nairobi mechanical engineering laboratories. Table 3.3 and Table 3.4 shows the parameters used in the design of LCF specimen. The procedure used for preparing the specimens involved marking, cutting, drilling and finishing. The specimens prepared were marked using a felt pen and placed onto the L- beam where they were securely fastened using bolts and nuts. The free ends of the specimens were then fastened to the eyebolt mechanism of the connecting rods using fibre locknuts. Having confirmed that all parts were securely fixed, the motor was then plugged into the mains and the fatigue tests began. The start time was recorded. The fatigue tests were left to run with constant observations made to the fatigue rig and terminated when all the specimens had fractured. The number of cycles (N) was recorded and a graph of strain versus cycles was developed.

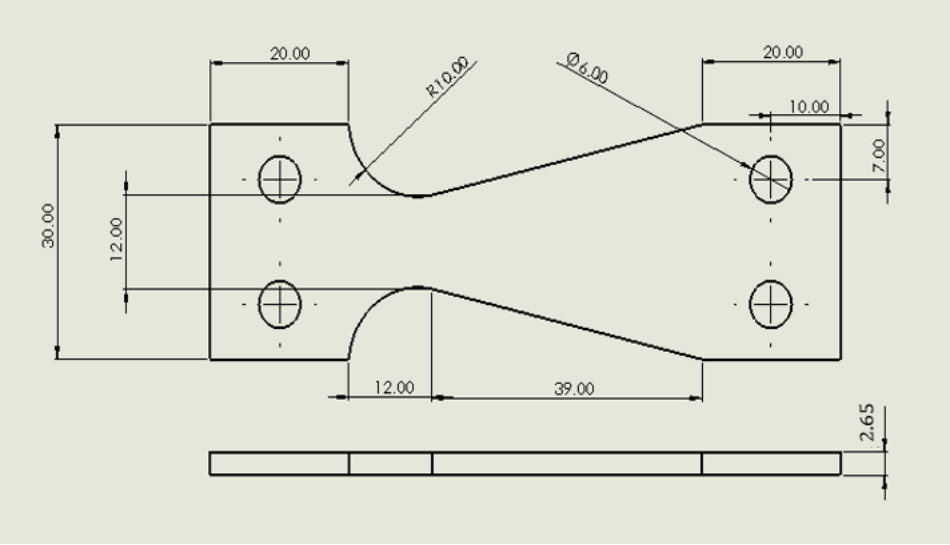

Figure 3.18: Dimensions of LCF Specimen.

Table 3. 3: Deflection measured by use of strain gauge on the fatigue rig machine

Position of the specimen on the fatigue rig machine	Deflection	Deflection Value (mm)
Position 1	δ_1	3.394
Position 2	δ_2	3.088
Position 3	δ_3	2.423
Position 4	δ_4	2.242

There exists a relationship between specimen deflection and stresses imposed [136] as shown in equation 3.6 and equation 3.7. δ is the specimen deflection, F is the force applied that results to stress σ, L is the specimen length, B_o is the specimen width, H is the specimen thickness and E is the modulus of elasticity.

$$F = \frac{B_O H^2 \sigma}{6L} \quad \ldots\ldots\ldots\ldots\ldots\ldots\ldots\ldots\ldots\ldots\ldots\ldots\ldots\ldots\ldots\ldots\ldots\ldots\ldots [3.6]$$

$$\delta = \frac{6FL^3}{B_O E H^3} = \frac{\sigma L^2}{EH} \quad \ldots\ldots\ldots\ldots\ldots\ldots\ldots\ldots\ldots\ldots\ldots\ldots\ldots\ldots\ldots\ldots\ldots\ldots\ldots [3.7]$$

Using AA 2014 properties, where σ_y = 410 MPa, σ_{UTS} = 446 MPa, E = 71 GPa, H = 2.6 mm and B_o = 30 mm, maximum and minimum specimen length located at position 1 is as shown below.

$$L_{max} = \frac{\sqrt{\delta_1 EH}}{\sigma_y} = \frac{\sqrt{0.003394 * 71 * 10^9 * 0.0026}}{410 * 10^6} = 39.09\, mm$$

$$L_{min} = \frac{\sqrt{\delta_1 EH}}{\sigma_{UTS}} = \frac{\sqrt{0.003394 * 71 * 10^9 * 0.0026}}{446 * 10^6} = 37.48\, mm$$

Table 3.4: Specimen L_{max} and L_{min} values for respective deflection measured

Position of the specimen on the fatigue rig machine	Deflection	Deflection Value (mm)	$L_{max}(mm)$	$L_{min}(mm)$
Position 1	δ_1	3.394	39.09	37.48
Position 2	δ_2	3.088	37.28	35.75
Position 3	δ_3	2.423	33.03	31.67
Position 4	δ_4	2.242	31.77	30.46

L_{max} value ranges from 31.77 to 39.09 mm and therefore it is valid to choose L value equal to 39 mm in specimen design. Using length l equal to 39 mm, E = 71 GPa, H = 2.6 mm, B_o = 30 mm, forces and stresses at location 1 were calculated as shown below and recorded in Table 3.5. Figure 3.19 shows a set of the fractured specimens after the test.

$$\sigma_1 = \frac{\delta_1 EH}{L^2} = \frac{0.003394 * 71 * 10^9 * 0.0026}{0.039^2} = 411.92\, MPa$$

$$F_1 = \frac{B_O H^2 \sigma_1}{6L} = \frac{0.03 * 0.0026^2 * 411.92 * 10^6}{6 * 0.039} = 356\, N$$

Table 3.5: Loading experience on the specimen at each deflection point

Position of the specimen on the fatigue rig machine	Deflection	Deflection Value (mm)	σ (MPa)	F (N)
Position 1	δ_1	3.394	411.92	356
Position 2	δ_2	3.088	374.78	324.81
Position 3	δ_3	2.423	294.07	254.86
Position 4	δ_4	2.242	272.11	235.83

Figure 3.19: Fractured specimens after test.

3.6. Microstructure Characterization

3.6.1 Optical Microscopy

The preparation of the specimens (BM and two regions of the HAZ) involved the following processes; sectioning, mounting, grinding, polishing and etching. The machine used for both grinding and polishing was Spectrum System 1000 Grinder/Polisher shown in Figure 3.20. The machine has an adjustable water faucet for each wheel, variable speed base, built in timer and a rugged 3/4 horse power motor which drives both 8-inch wheels simultaneously.

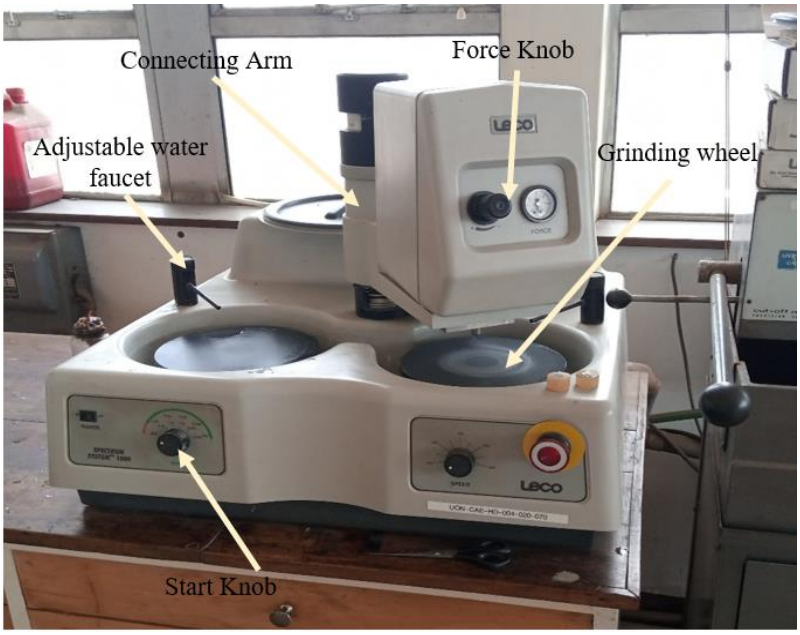

Figure 3.20: Spectrum System 1000 Grinder/Polisher.

The specimens were embedded in resin for ease of handling as demonstrated in Figure 3.21. The specimens were ground starting with coarse grinding and ending up with the fine grinding using a series of silicon carbide (SiC) papers of increasing fineness (grades 240, 320, 400, 600, 800) under running water. The specimens were cleaned in between each paper finish to remove any grit. The samples were then polished on a rotating wheel covered with a suitable cloth impregnated with a polishing diamond paste of 6µm, 1µm and alumina (Al_2O_3 slurry) of 1/4µm. The specimens were then etched in Kroll's reagent and optical micrographs were taken with the optical microscope.

Figure 3.21: Mounted specimens for micrography and hardness test.

3.6.2 Average ASTM Grain Size Number

A universal Microscope (OPTIKA B-353 MET) with a maximum magnification of X500 (Figure 3.22) was used to obtain the optical micrographs. A digital camera of resolution 2592 x 1944 pixels connected with a USB cable to the computer was used to take the micrographs. The optical micrographs of the BM and the two HAZ regions were obtained. The grain size was obtained using commercial software, the microstructure characterization software 3.0 (MIC 3.0). The software is developed by TCR Advanced Engineering (P) LTD, India. The software has a micrographic image solarizer for identification of phases and grain boundaries. The images can be taken directly from an attached camera or the images stored in the computer can be used. The MIC 3.0 then creates reports in specified layouts such as 'Joint photographic Experts Group (jpeg)' format. It also has a file format saving system for all custom reports with Microsoft (MS-Word) document interface. The software uses the ASTM E-112 linear intercept method [137] which is inbuilt in it.

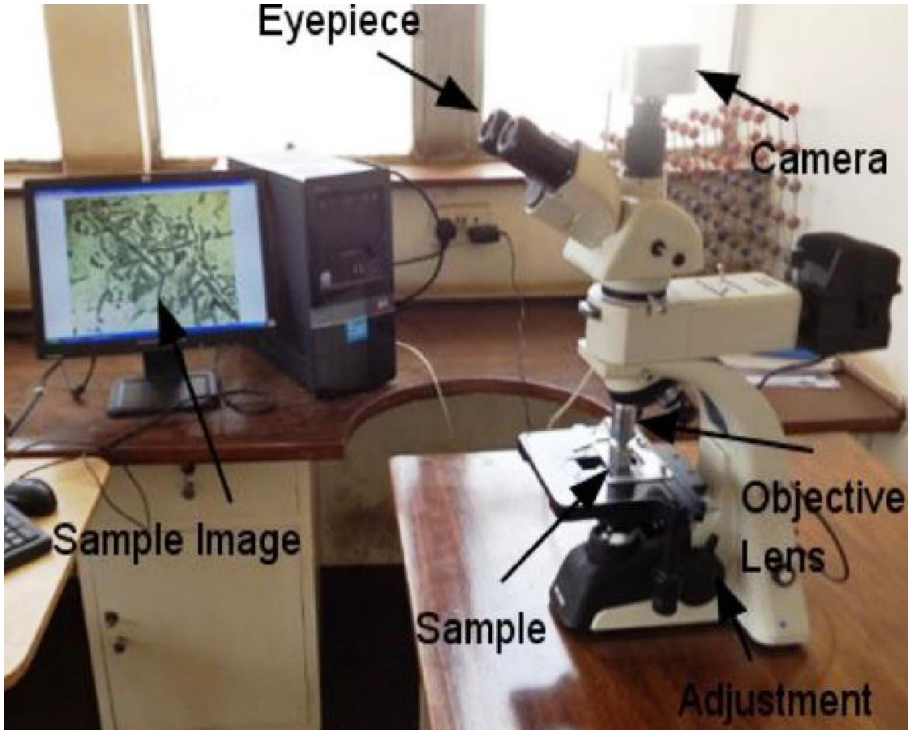

Figure 3.22: The Optical microscope connected to a computer [132].

3.7 Hardness Testing

The hardness test was done in accordance with ASTM E92 [138]. The equipment used was the Vickers macro hardness tester LV 800. Figure 3.23 below shows the type of hardness tester used, which was supplied by LECO Corporation in St. Joseph, Michigan, USA. The tester has a load capacity of 0.3 kgf to 10 kgf. It is fitted with 10x and 20x objectives and built with a video adapter. The hardness tester has an inbuilt conversion scale and hence the Vickers hardness number is directly read from its display panel.

The test specimens were placed on the stage and focusing done to bring images to clear focus using the X20 objective. The test was done using a load of 10 kgf and a dwell time of 20 seconds. The hardness values were read directly from the LCD panel attached to the machine. The indentations were done at intervals of 1 mm apart and eight indentations were carried out on every specimen to get the representative reading. An average was then calculated to get the hardness value. Hardness values for this study are in terms of Vickers Number, HV.

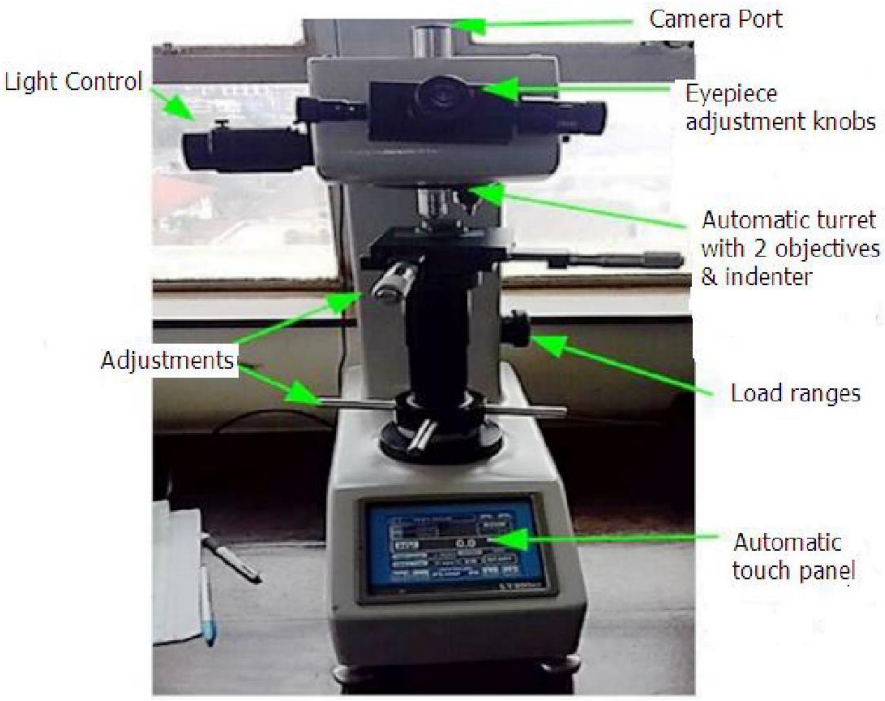

Figure 3.23: Vickers Macro hardness tester LV 800 [132].

CHAPTER FOUR: RESULTS

4.1 Tensile Properties

Longitudinal tensile test for AA 2014 specimen (as received) was carried out as discussed in section 3.2. Three tests were performed and the tensile test data recorded in Appendix A. This data was used to generate graphs of stress versus strain for the three tests shown in Figures 4.1, 4.2 and 4.3. Figure 4.4 represents a comparison of the Stress strain curves for the three tensile tests. The proof stress, ultimate stress and gauge length elongation in percentage was determined from each graph. Table 4.1 represents the average tensile properties values for the AA 2014 specimen as received.

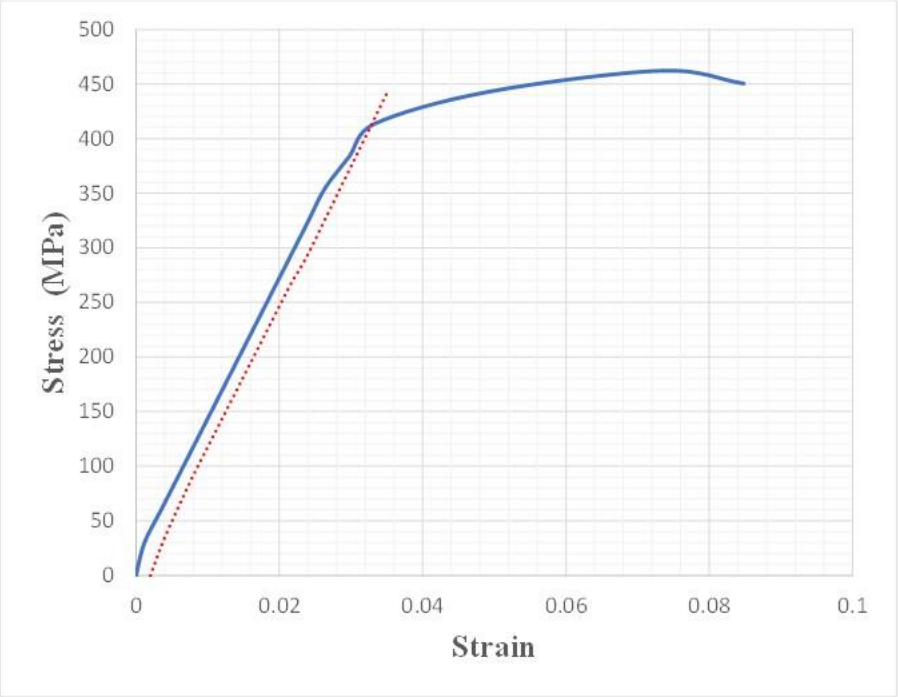

Figure 4. 1: Stress strain curve for AA 2014 specimen (First test)

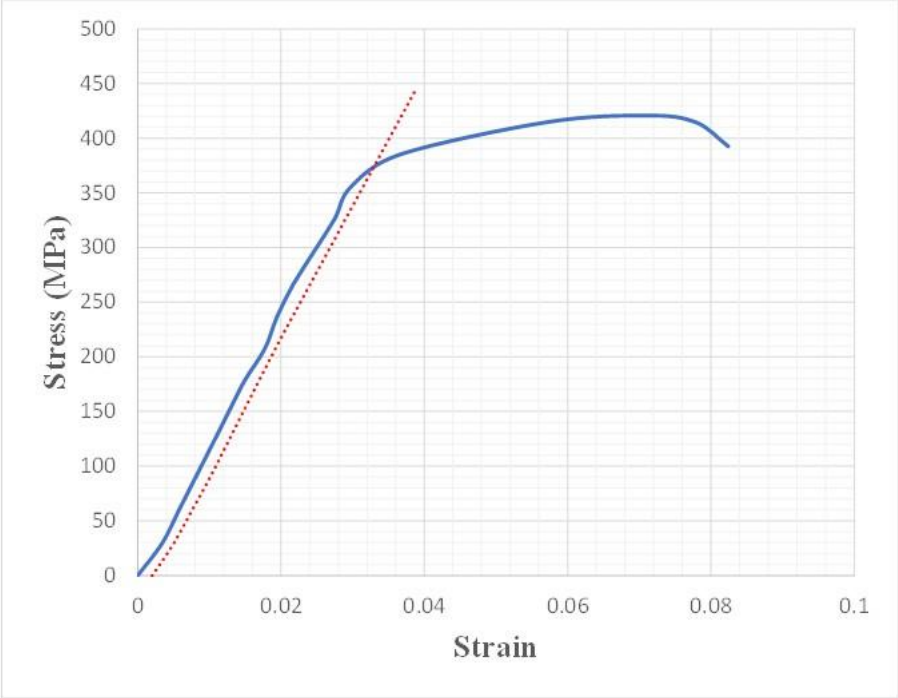

Figure 4. 2: Stress strain curve for AA 2014 specimen (Second test)

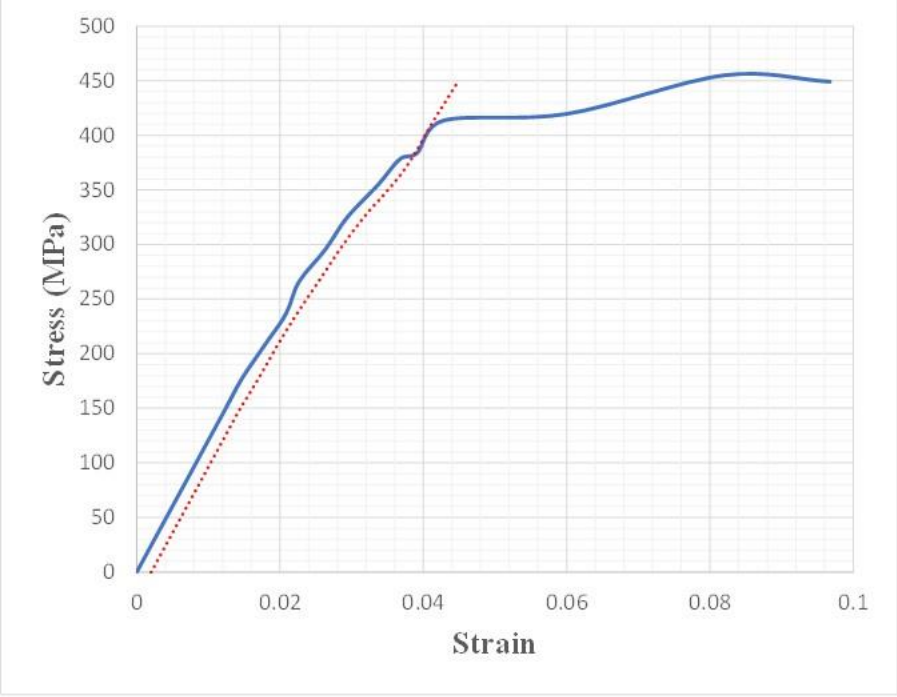

Figure 4. 3: Stress strain curve for AA 2014 specimen (Third test)

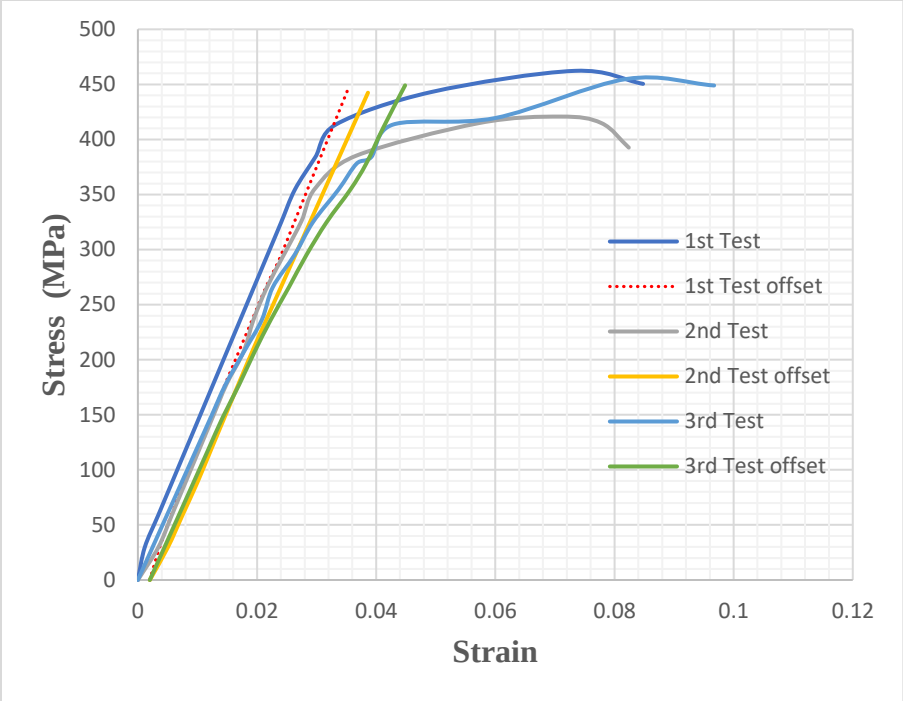

Figure 4.4: Stress strain curves for AA 2014 specimen (Three tests)

Table 4.1: Comparison of longitudinal tensile properties between the base metal and manufacturer data for AA 2014.

Tensile Properties	Proof Stress $\sigma_{0.2}$ (MPa)	Ultimate Stress σ_{UTS} (Mpa)	25 mm gauge Length Elongation (%)
Average Test Data	401	446	8.79
Manufacturer Data	390	460	11

4.2 Thermal Cycle Simulation profiles

Simulated thermal cycle data for HCF, LCF and FCG specimens for the two regions of HAZ of AA 2014 is shown in Appendix B. Figures 4.5, 4.6 and 4.7 represent thermal simulation cycles across the two regions of HAZ of AA 2014 for HCF, LCF and FCG specimens respectively. Figure 4.8 represents a comparison of the thermal cycle histories for the three different

specimens. The highest thermal cycle simulated temperature was 650°C which characterized the HAZ region closest to the weld FL. This region represented 4mm from the FL and was designated by letter D while the HAZ region thermally simulated at 590°C representing 5mm from FL was designated by letter C as shown in Table 4.2. Thermal cycle simulation parameters (temperature and replicated distance from the weld FL) for AA 2014 aluminium alloy specimen are represented in Table 4.2.

Table 4.2: Thermal cycle simulation parameters for AA 2014.

AA 2014 Specimen Region (2.65 mm thick)	Thermal Simulation Temperature	Replicated Distance from Weld Fusion Line
BM	As-received	>15 mm
HAZ region C	590°C	5 mm
HAZ region D	650°C	4 mm

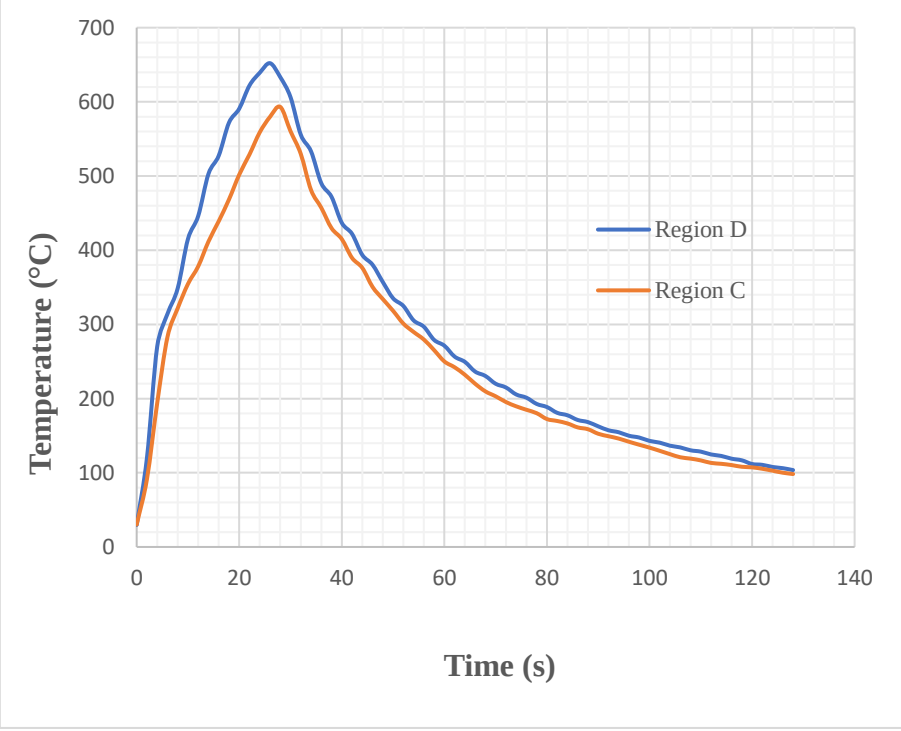

Figure 4.5: Thermal simulation cycles across the two regions of HAZ of AA 2014 HCF Specimens.

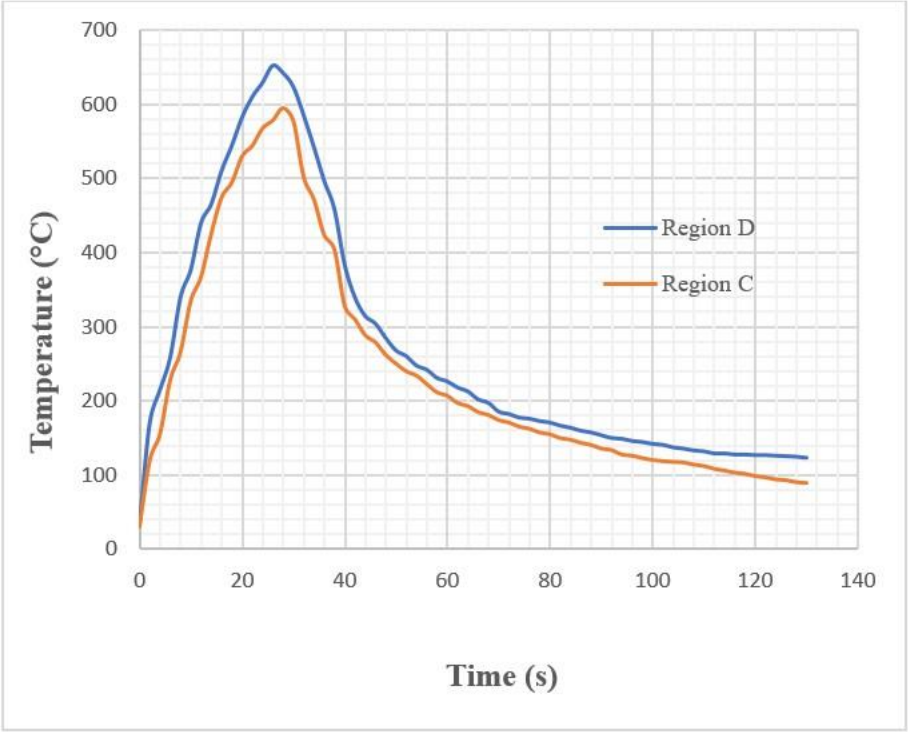

Figure 4. 6: Thermal simulation cycles across the two regions of HAZ of AA 2014 LCF Specimens.

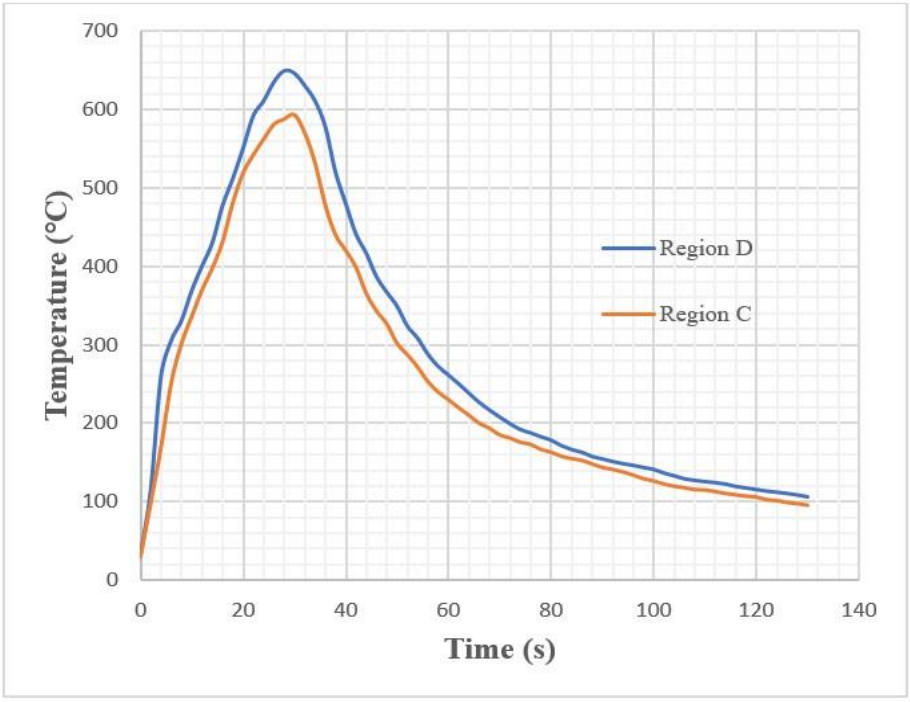

Figure 4. 7: Thermal simulation cycles across the two regions of HAZ of AA 2014 FCG Specimens.

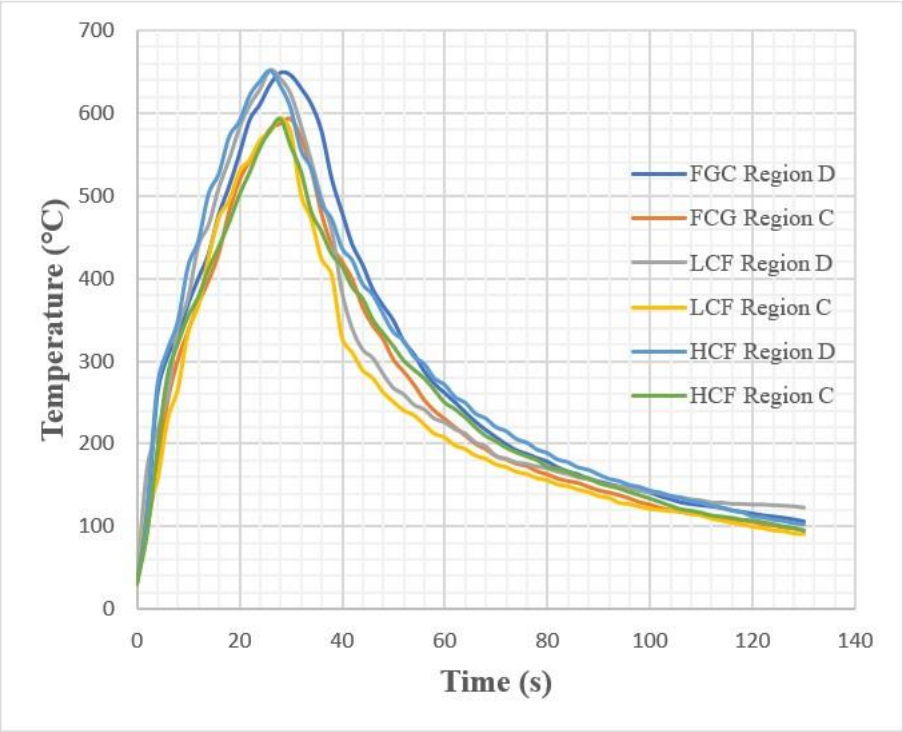

Figure 4. 8: Thermal simulation cycles across the two regions of HAZ of AA 2014 HCF, LCF and FCG Specimens.

The three thermally simulated curves shown in Figures 4.5 to 4.7 reflect typical patterns of most arc welds during the actual welding process as outlined in Figure 3.5. For the three different specimens, namely; FCG, HCF and LCF specimens, there is little variation in the time required to reach peak temperatures of the two regions of HAZ. There is an observed steep temperature distribution with slight decrease in gradients for the two regions of HAZ in all specimens as shown in Figure 4.8. Higher heating and cooling rates are recorded for the HAZ region D which is thermally simulated at 650°C as compared to HAZ region C thermally simulated at 590°C for all the three specimens (LCF, HCF, FCG specimens).

4.3 Fatigue Strength

The fatigue strength data of the BM and the two regions of the HAZ are as shown in Table 4.3 and in Appendix C. The approximate fatigue strength was calculated using linear regression method as already discussed in section 3.4.3 and results tabulated in Table 4.3. Results in Figure

4.9 show that the BM had the highest fatigue strength of 123 MPa while the HAZ region C had the least fatigue strength of 84 MPa. There was a slight improvement of fatigue strength in the HAZ region D compared to the HAZ region C from 84MPa to 92 MPa.

Table 4.3: Fatigue strength data of the BM and two regions of the HAZ of AA 2014.

AA 2014 Specimen Region	Thermal simulation Temperature	Approximate Fatigue Strength (MPa)
BM	As-received	123
HAZ Region C	590°C	84
HAZ Region D	650°C	92

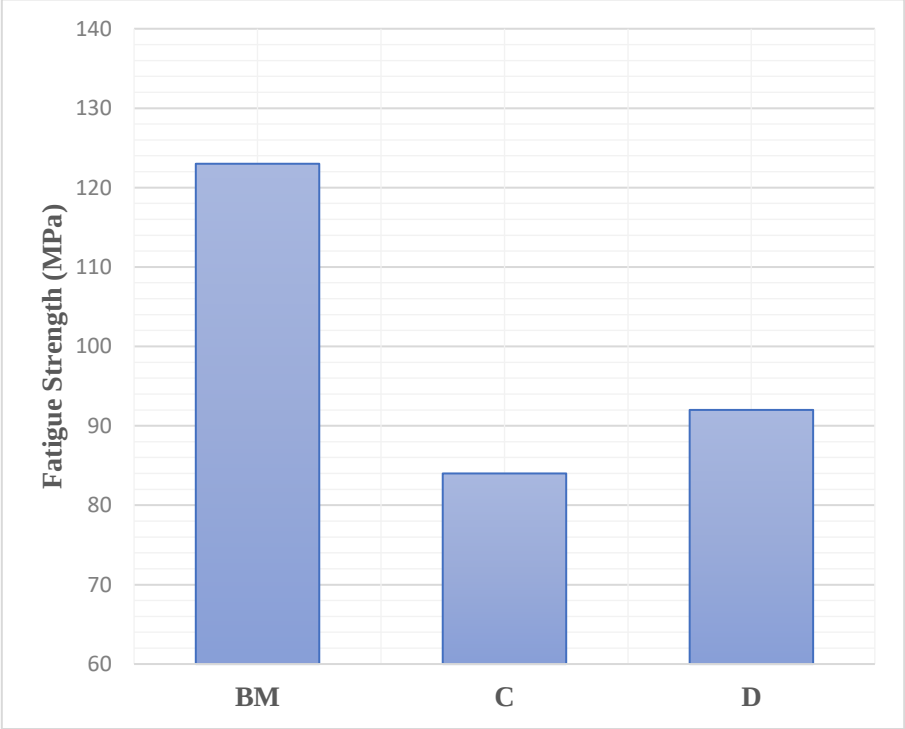

Figure 4.9: The fatigue strength of the BM, region C and D of the HAZ.

4.4 Low Cycle Fatigue

LCF test for the BM and two regions of the HAZ of AA 2014 was carried out and data recorded in Appendix D. A graph of the total strain amplitude (combination of both plastic and elastic strain range) versus reversals to failure was developed and represented in Figure 4.10. From the strain life curve, it is evident that fatigue life is more pronounced at low strains than high strains especially for the BM. This explains why at higher stains the strain life curves tend to act like they are heading towards a common point whereas at lower strains the three curves are much further apart. It is also evident that the HAZ region C exhibited shorter fatigue life as compared to the base metal and the heat affected zone region D. At both high and low strains, the HAZ region D had better fatigue life compared to the HAZ region C whereas the BM had the best fatigue life.

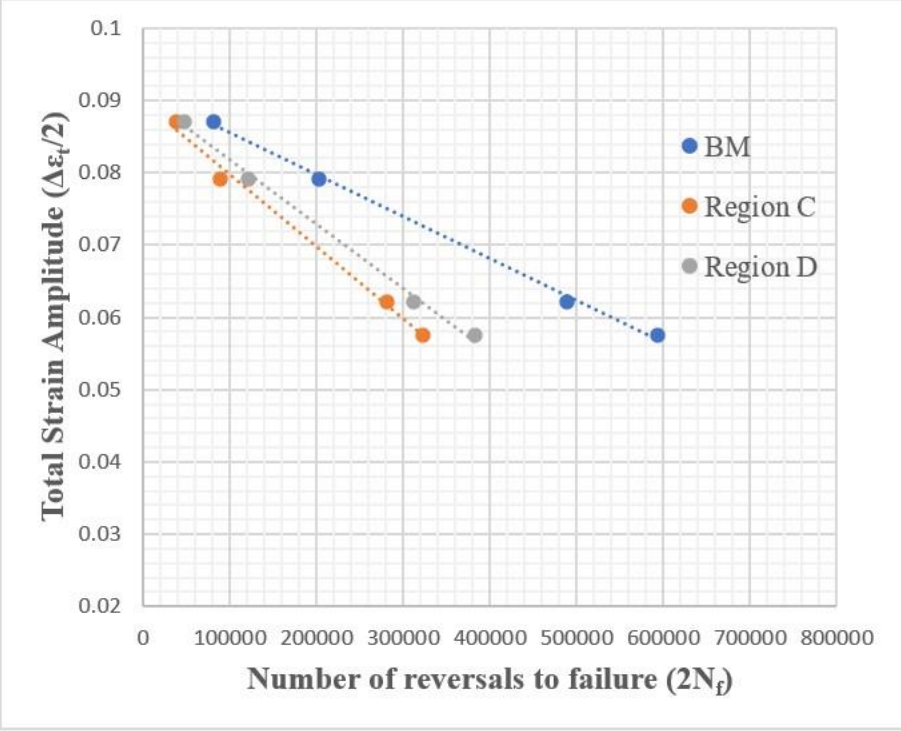

Figure 4. 10: Total strain amplitude versus reversals to failure of AA 2014.

4.5 Fatigue Crack Growth

The FCG test at a stress ratio R equal to 0.2 and data analysis was carried out. The data is recorded in appendix E. The Stress intensity factor range ΔK was calculated from the load range ΔP using equation 3.3 while rate of crack growth, da/dN was calculated using equation 3.2. This is illustrated here for the first set of data from Appendix E. Figures 4.11 to 4.18 represent FCG curves for the BM and the two regions of HAZ whose da/dN was determined using secant method. Graph program, whose interface is shown in figure 4.19 was used to analyze data for the graphical method. A graph of crack length versus cycles from FCG test of the BM and the two regions of HAZ C and D were plotted as shown in Figures 4.20 to 4.23. The slope, da/dN was determined using the Graph program and the corresponding value of crack length, a, at selected slope point was used to calculate the value of ΔK. FCG curves whose da/dN was determined using graphical method are as shown in Figures 4.24 to 4.27. The FCG constants C, m and the ΔK_{TH} values for the BM and the two regions of HAZ were evaluated and recorded in Table 4.4.

$$\Delta K = \frac{1771.1}{0.0026}\sqrt{\frac{\pi \times 0.0427}{2\times0.1\times0.1}}\,sec\frac{\pi \times 0.0427}{2 \times 0.1} = 1.764\ \text{MNm}^{-3/2}$$

$$\frac{da}{dN} = \frac{21.35 - 20.3}{86135-0} = 1.22\text{E-}05\ \text{mm/cycle}$$

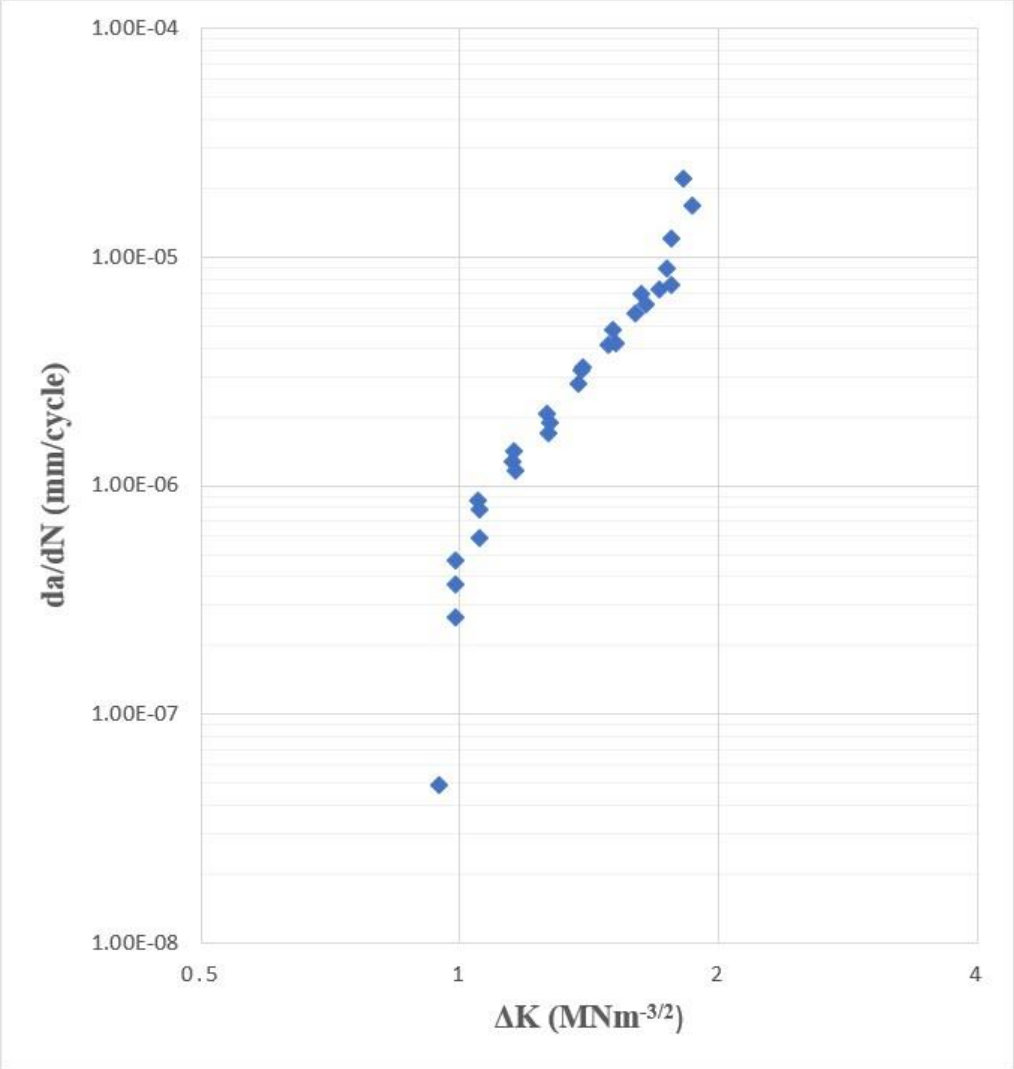

Figure 4.11: K-decreasing fatigue crack growth curve for the BM.

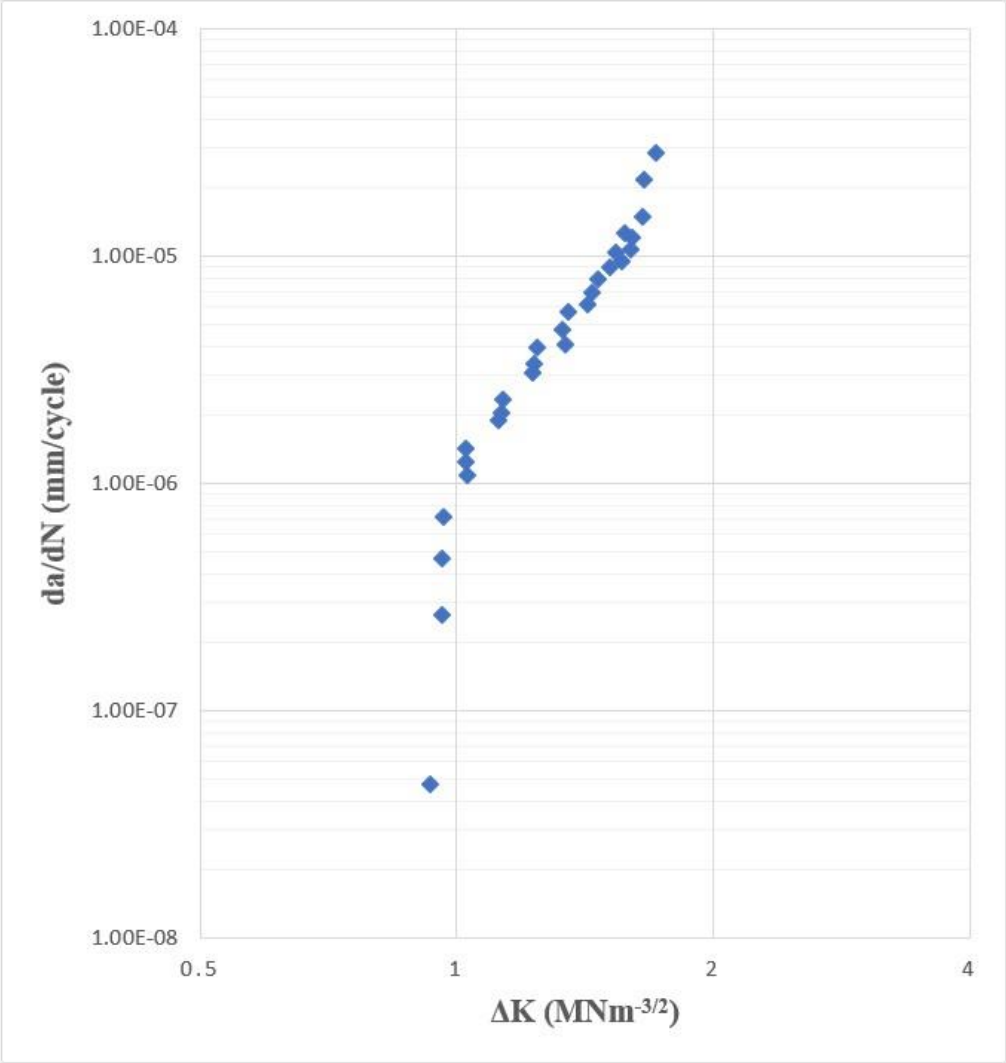

Figure 4.12: K-decreasing fatigue crack growth curve for region C of the HAZ.

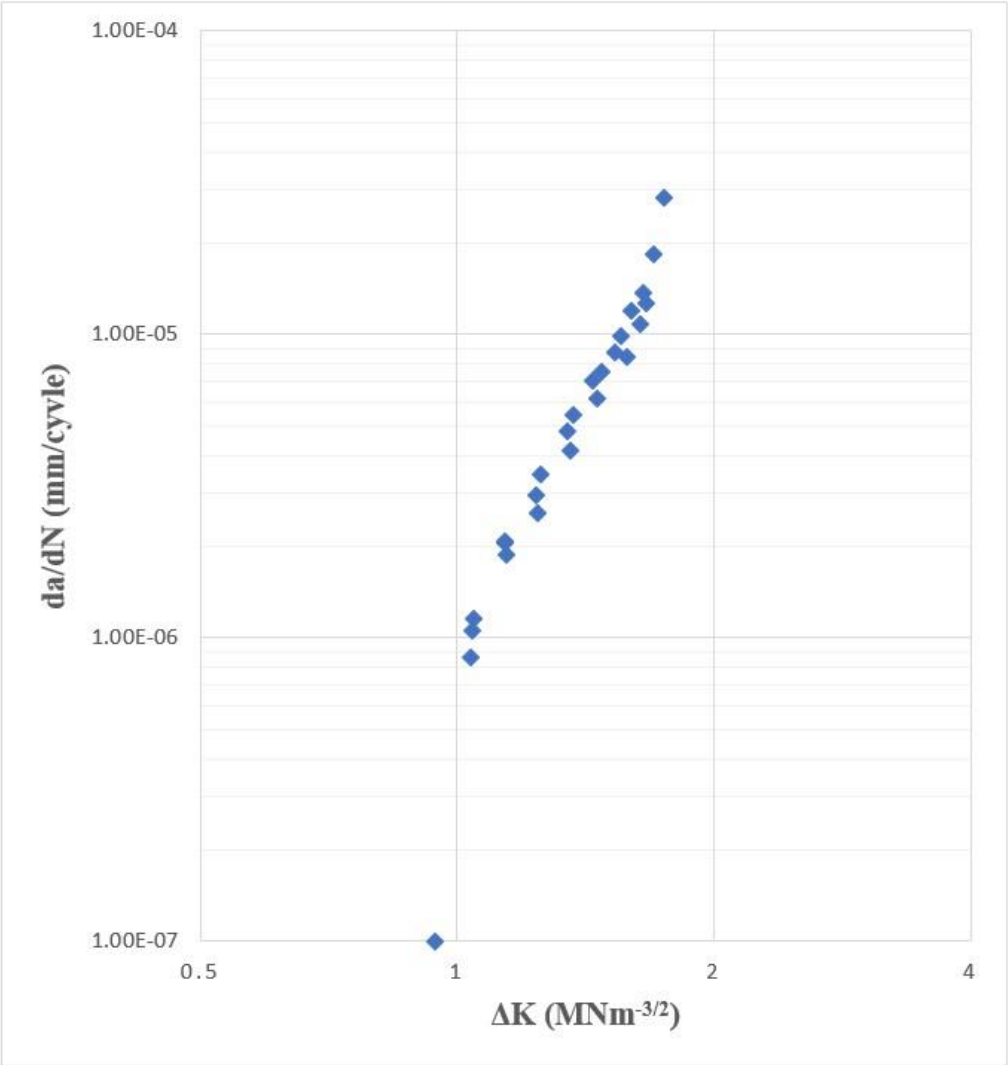

Figure 4.13: K-decreasing fatigue crack growth curve for region D of the HAZ.

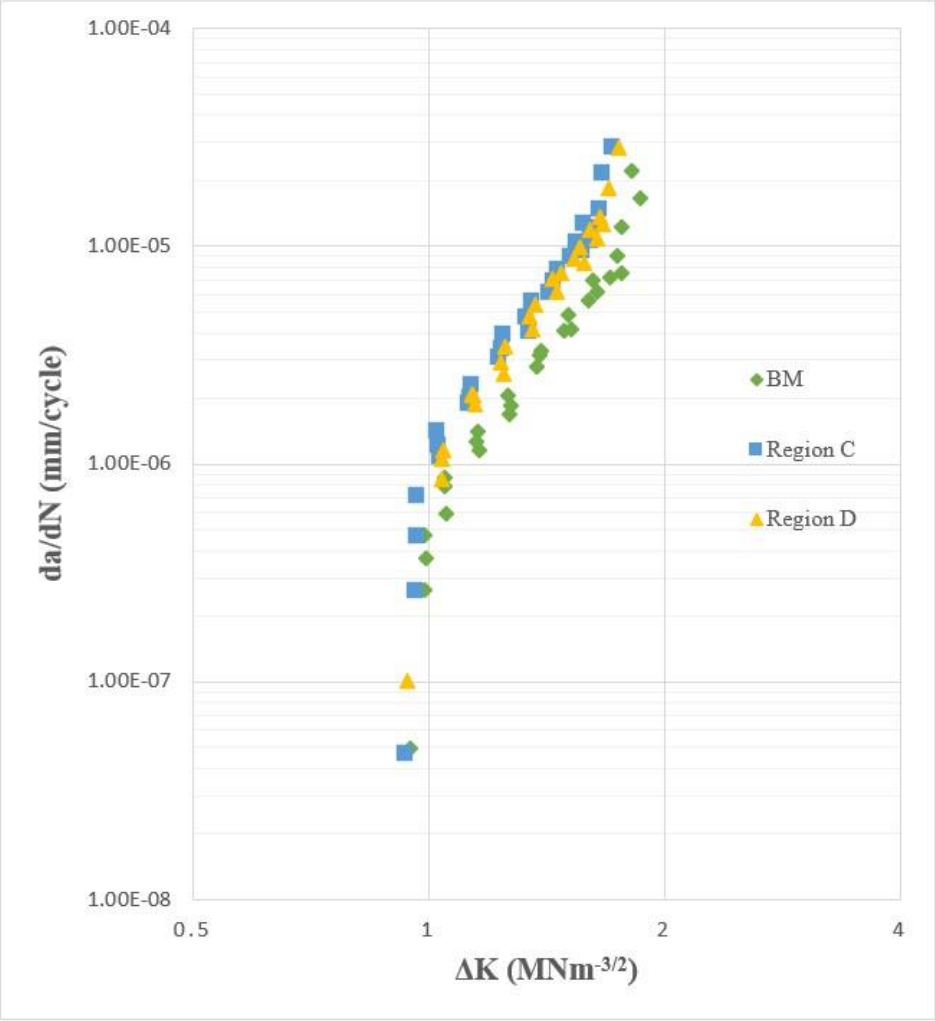

Figure 4.14: K-decreasing fatigue crack growth curve for the BM, region C and D of the HAZ.

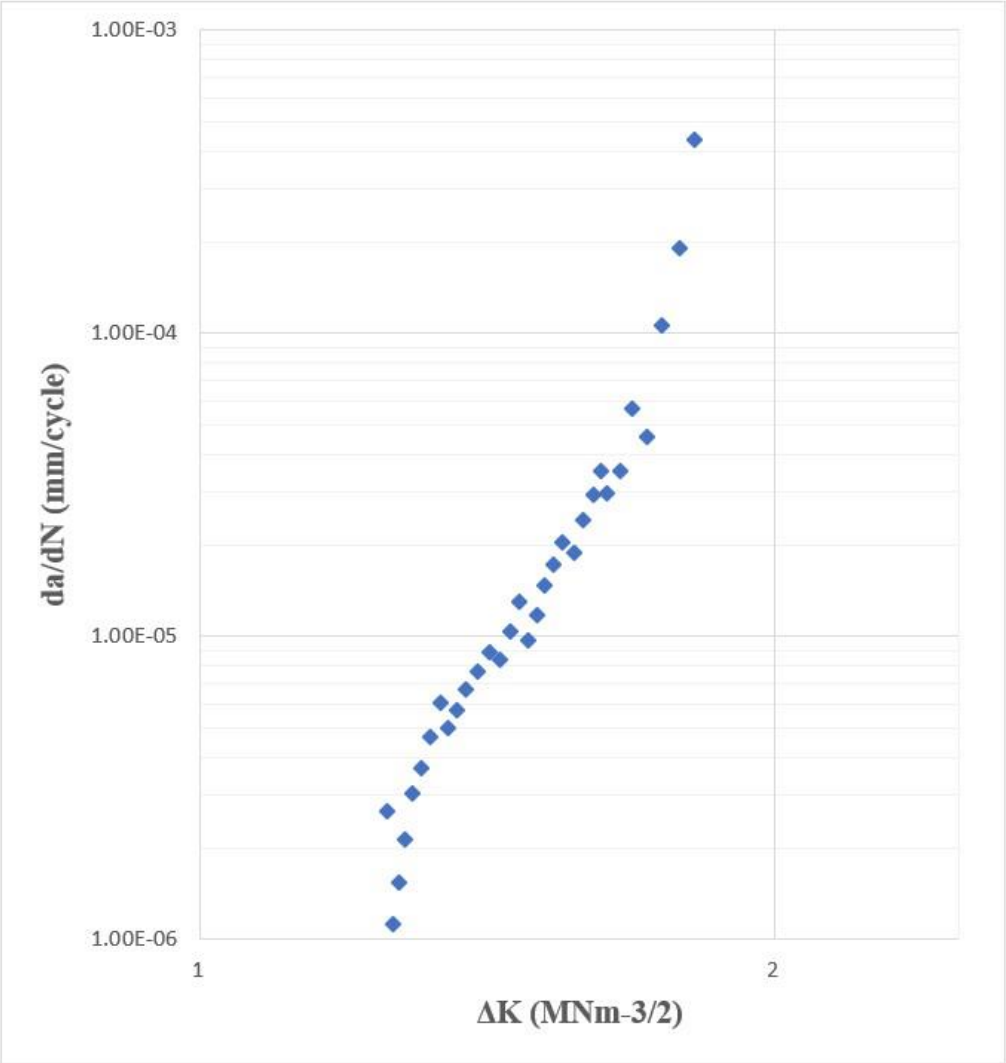

Figure 4.15: Constant amplitude fatigue crack growth curve for the BM.

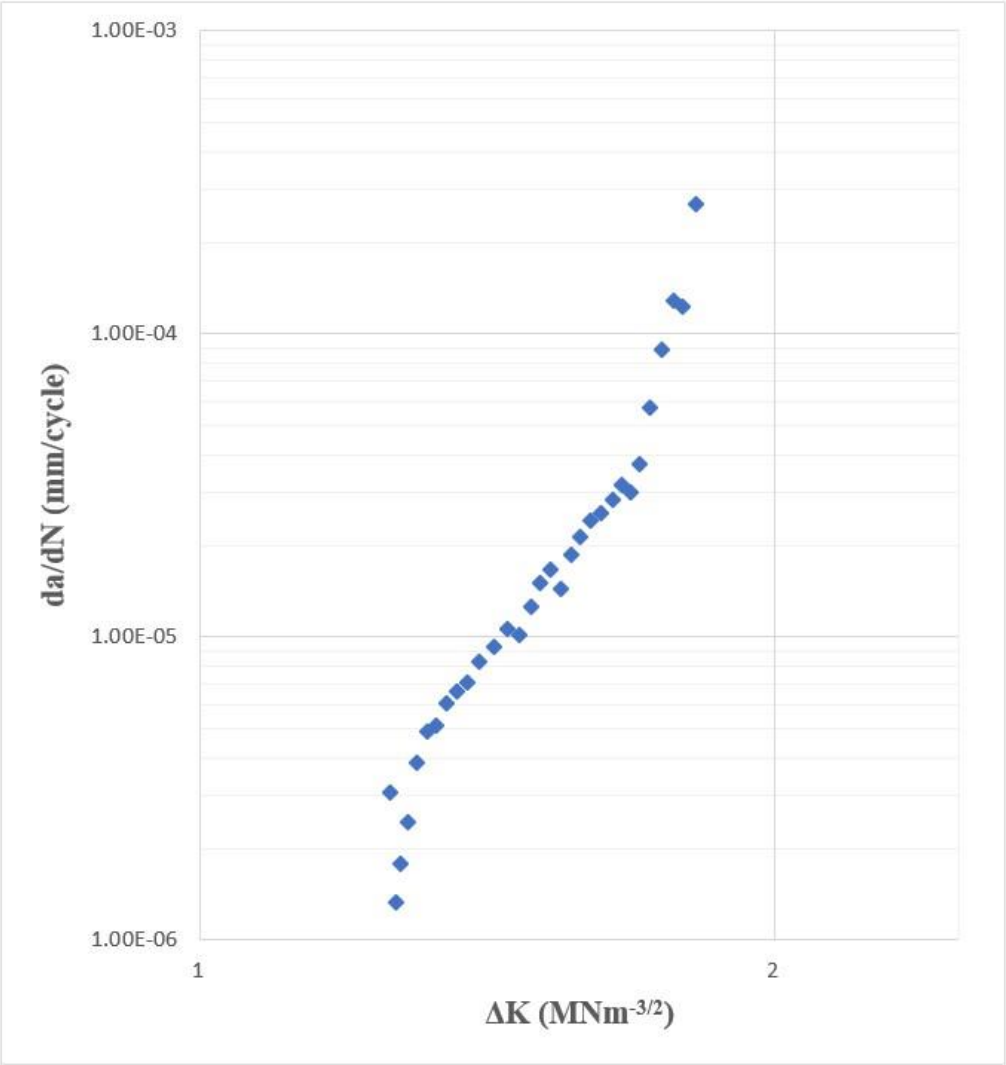

Figure 4.16: Constant amplitude fatigue crack growth curve for region C.

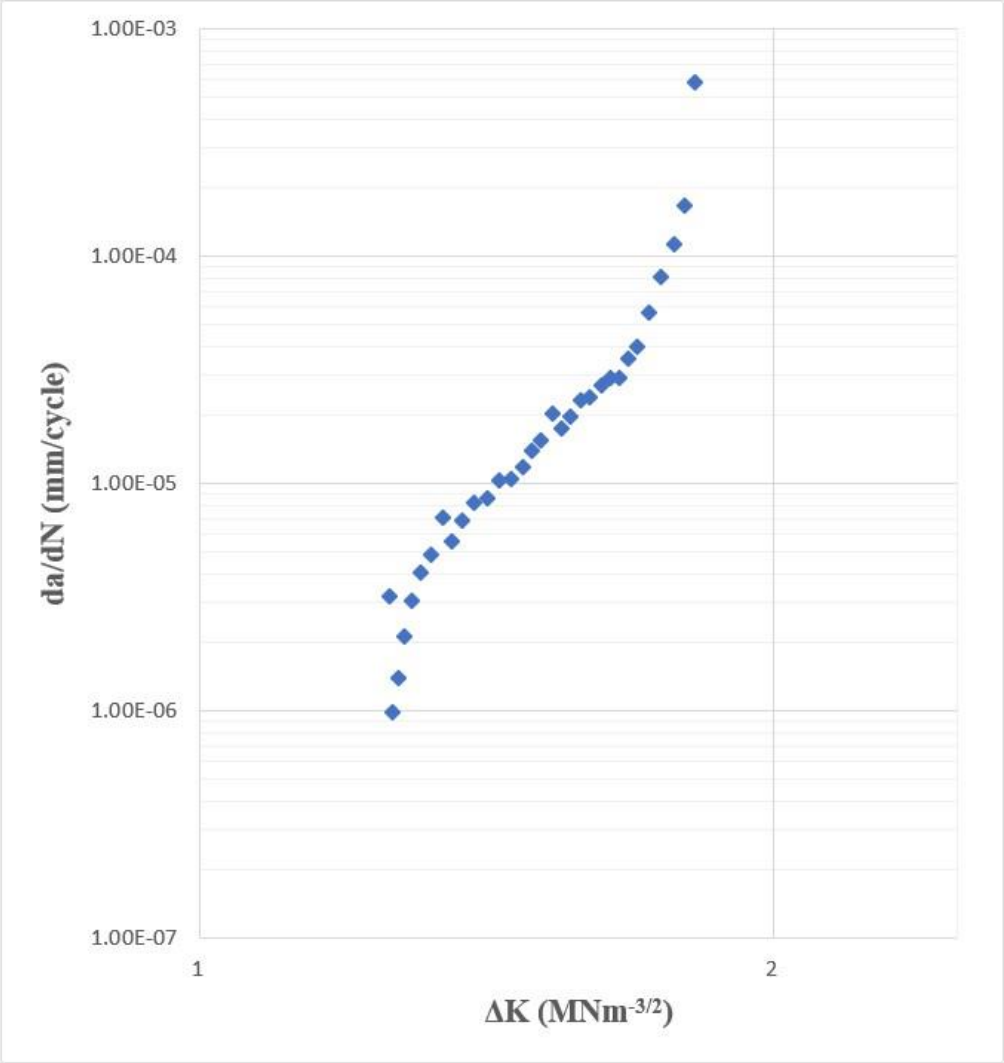

Figure 4.17: Constant amplitude fatigue crack growth curve for region D.

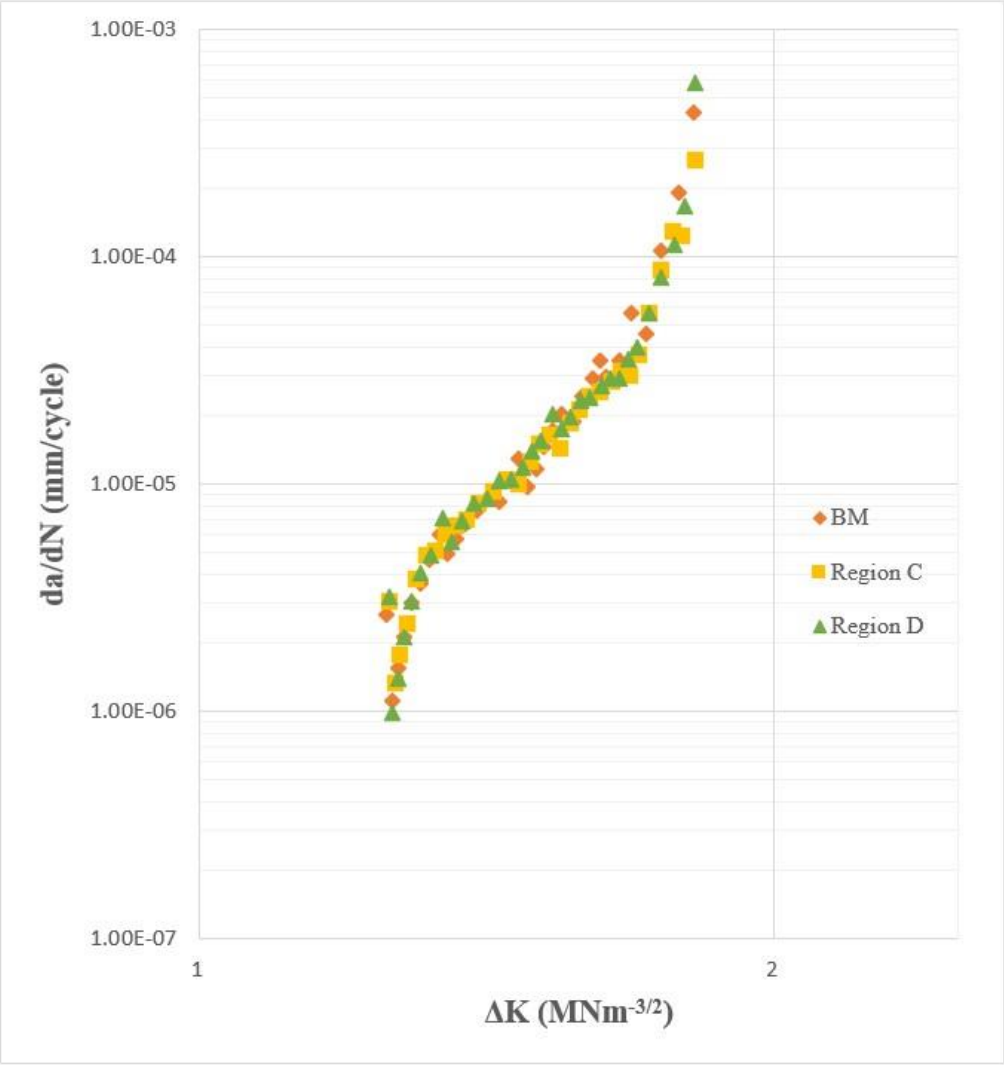

Figure 4.18: Constant amplitude fatigue crack growth curve for the BM, region C and D.

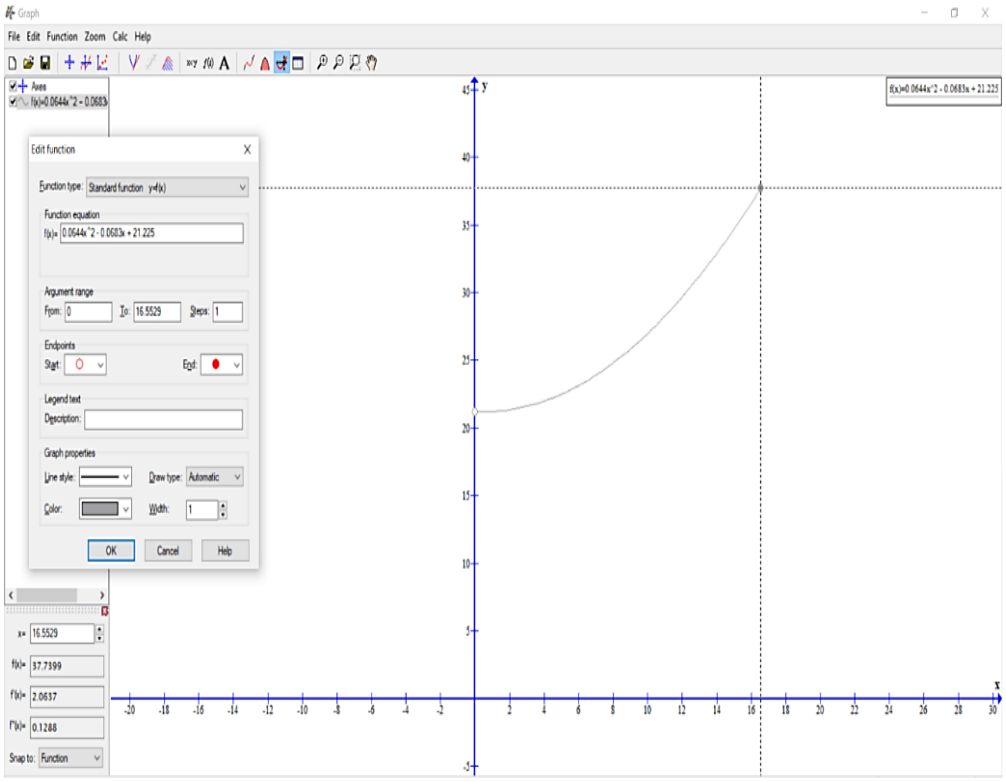

Figure 4.19: Graph program interface showing a representation of a vs N curve

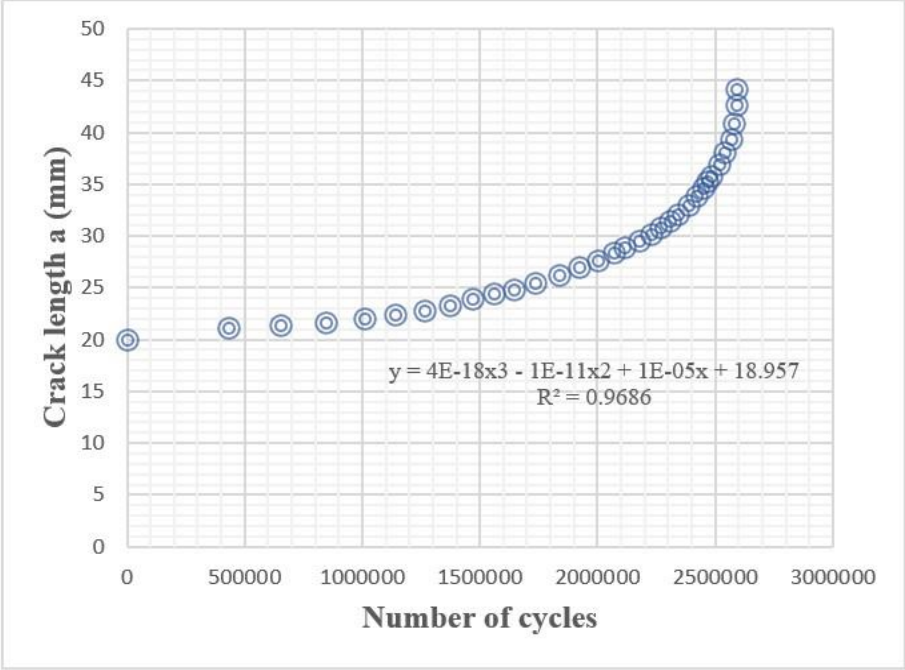

Figure 4. 20: Graph of crack length vs number of cycles for the BM.

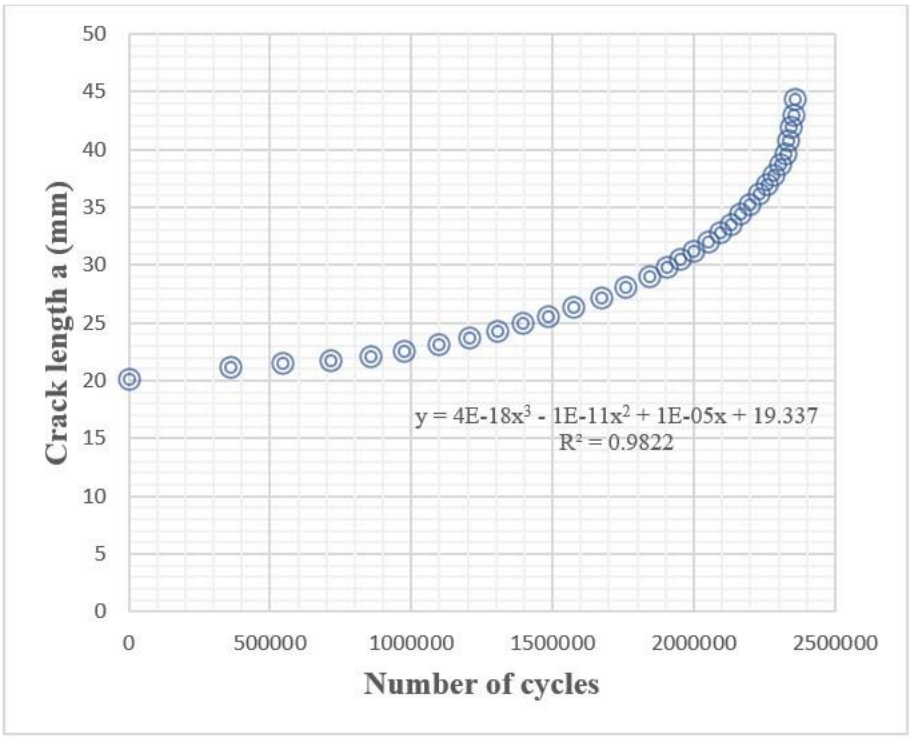

Figure 4. 21: Graph of crack length vs number of cycles for Region C.

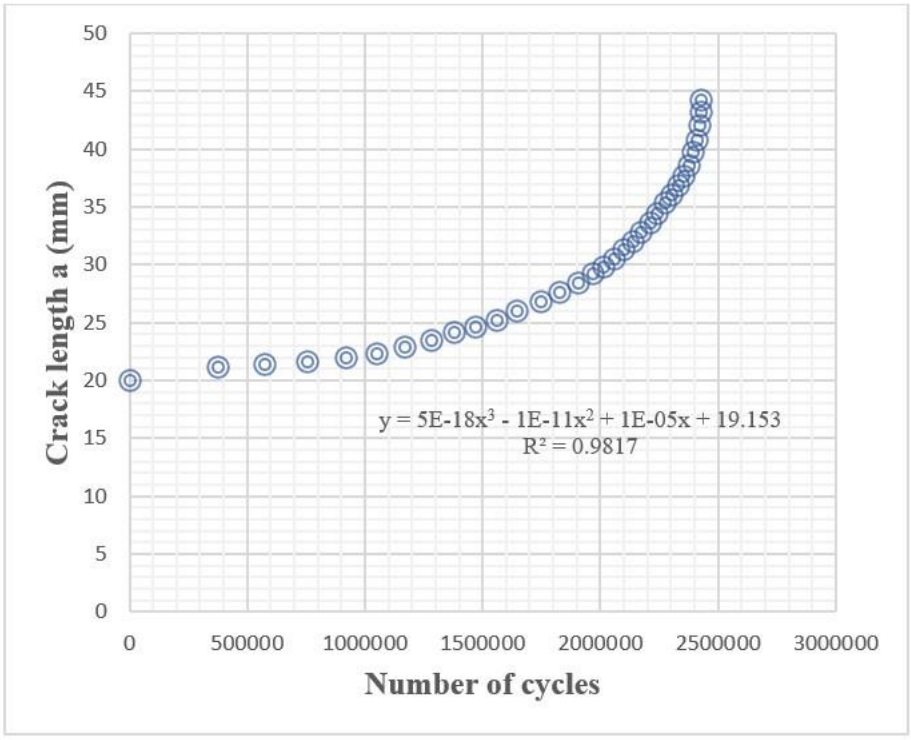

Figure 4. 22: Graph of crack length vs number of cycles for Region D.

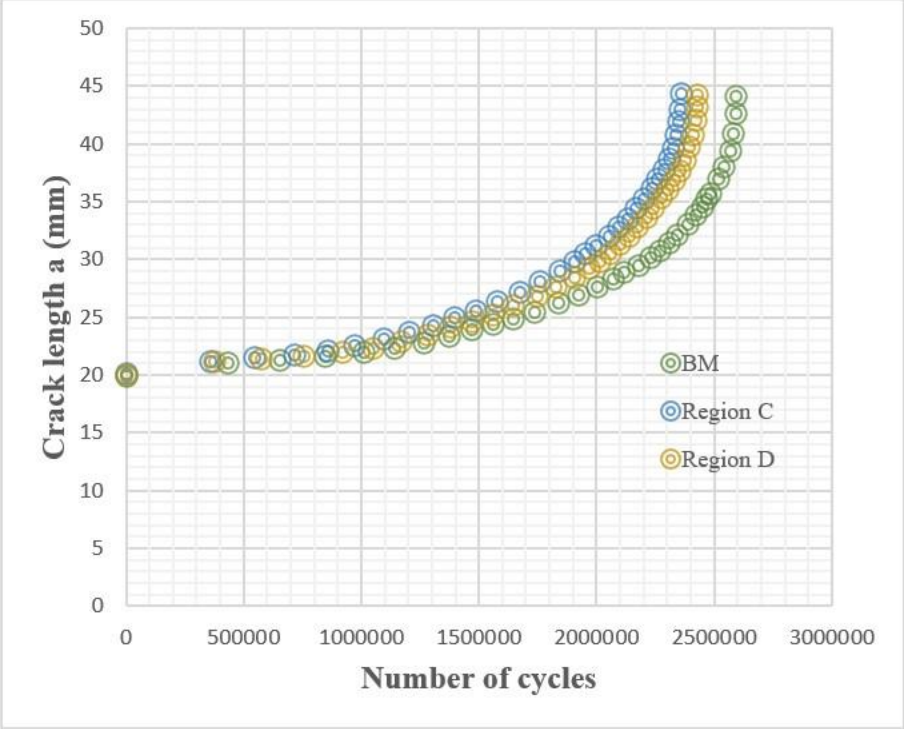

Figure 4. 23: Graph of crack length vs number of cycles for the BM, region C and D.

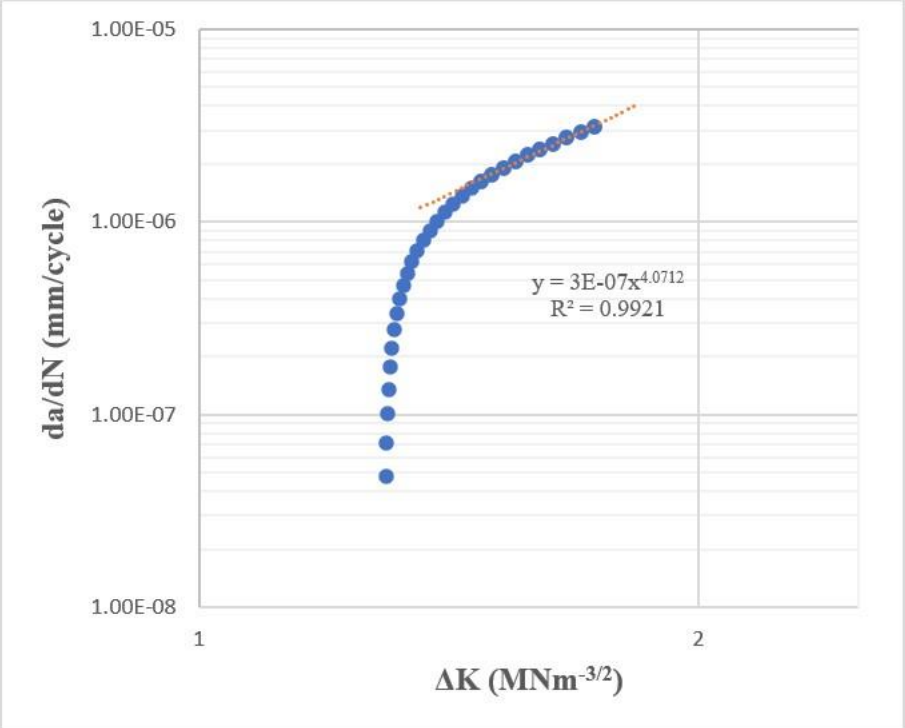

Figure 4. 24: Graphical method fatigue crack growth curve for the BM.

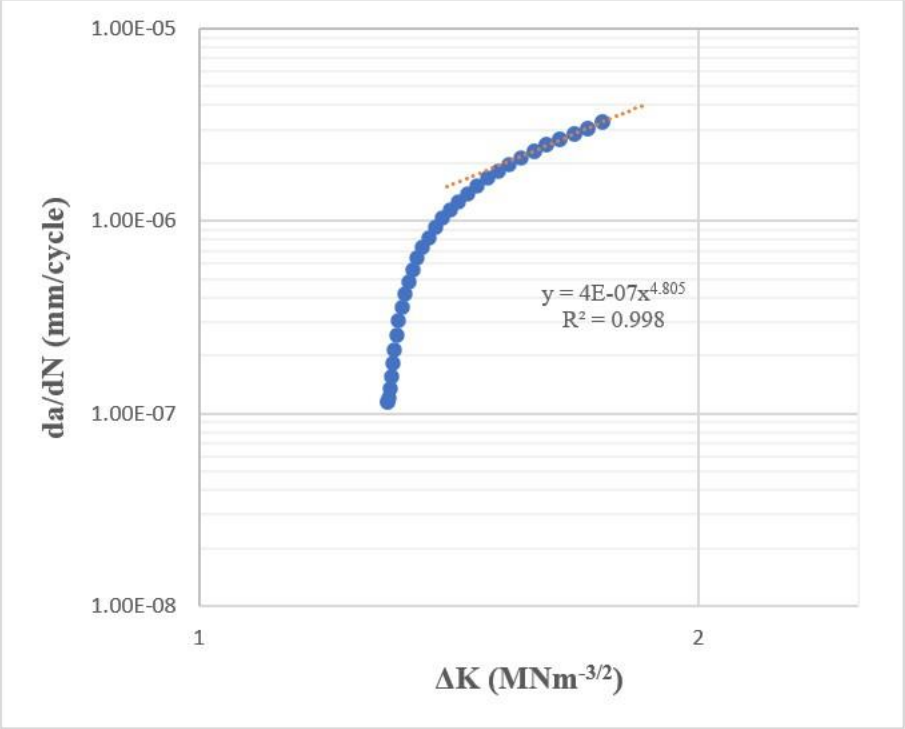

Figure 4. 25: Graphical method fatigue crack growth curve for region C.

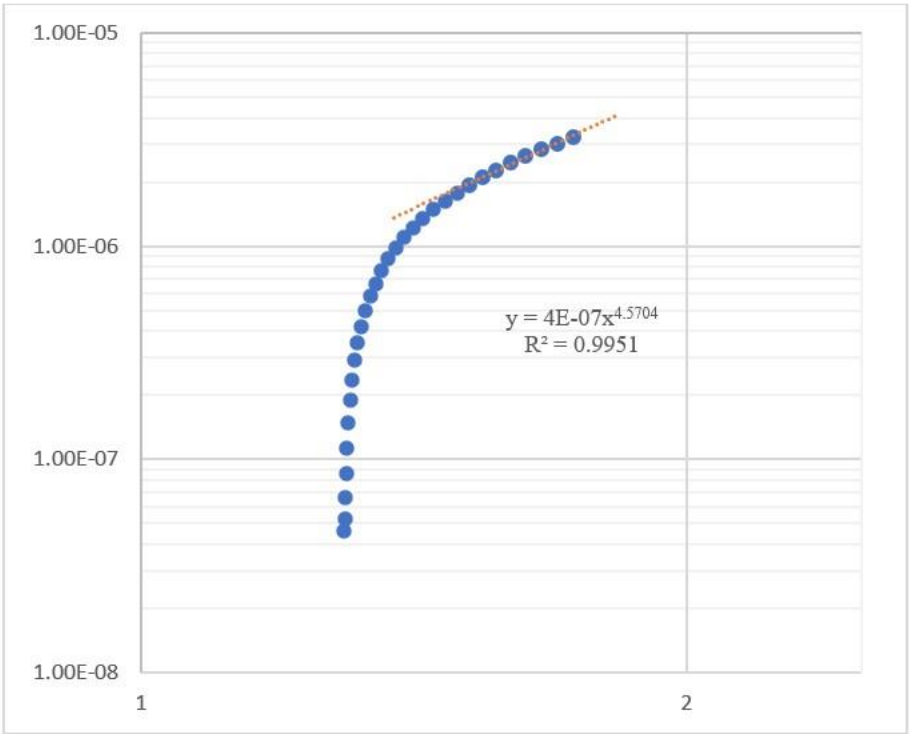

Figure 4. 26: Graphical method fatigue crack growth curve for region D.

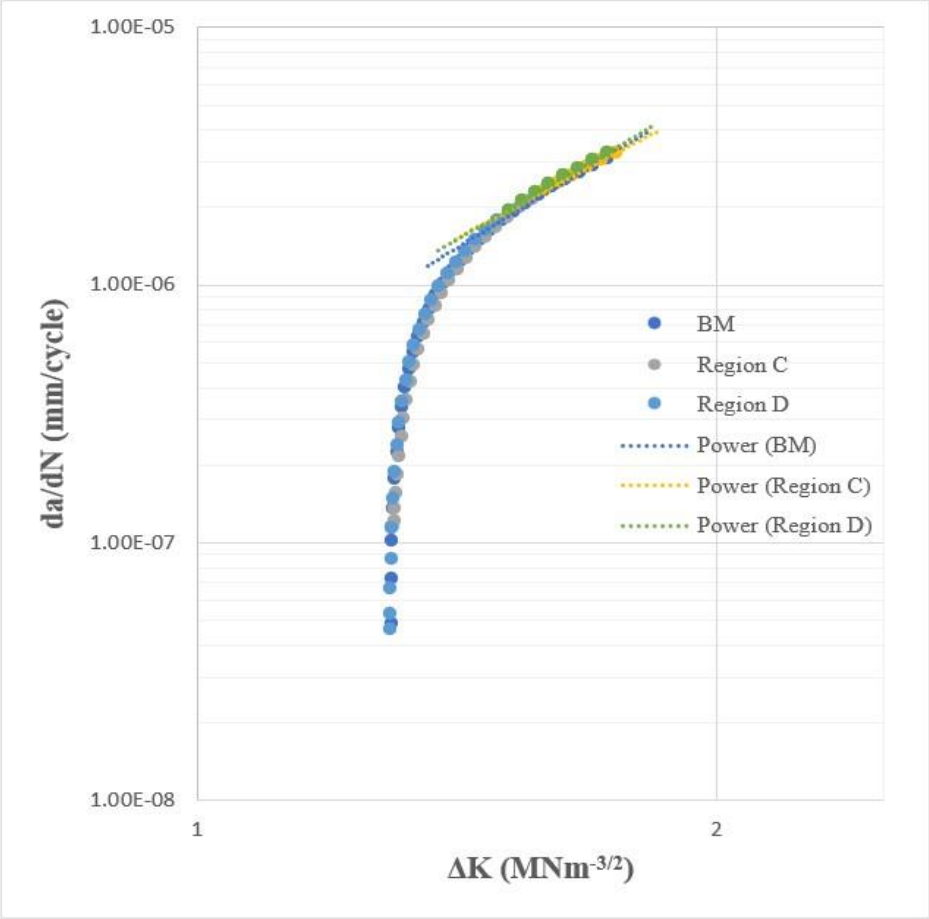

Figure 4.27: Graphical method fatigue crack growth curve for BM, region C and D.

The results in Table 4.4 represent the FCG behaviour of the BM and the two regions of the HAZ of AA 2014. There was no significant difference in the values of threshold intensity ΔK_{th} obtained in this study. It's evident from the values of ΔK_{th}, C and m, that the BM appears to offer the highest resistance to FCG compared to other regions of the HAZ. The HAZ region C appears to offer a lowest resistance to FCG compared to the BM and HAZ region D. Region D appears to offer a slightly greater resistance to FCG compared to region C.

Table 4.4: AA 2014 FCG Parameters ΔK_{TH}, C and m for the BM and the two regions of the HAZ.

AA 2014 Specimen Region	Thermal simulation Temperature	ΔK_{TH} ($MNm^{-3/2}$)	C (mm/cycle and $MNm^{-3/2}$)	m
BM	As-received	0.949	3.40188E-07	4.0712
C	590°C	0.931	4.39551E-07	4.8050
D	650°C	0.940	3.93450E-07	4.5704

4.6 Hardness Survey

Hardness test was carried out as outlined in section 3.7 and data collected is presented in Appendix F and results summarized in Table 4.5. A graphical representation of Vickers Hardness Numbers across the BM and the two regions of the HAZ of AA 2014 is as shown in the bar graph Figure 4.28. The BM and the HAZ region C recorded highest and lowest hardness values respectively. The HAZ region D recorded a higher hardness value compared to HAZ region C.

Table 4.5. Hardness Values for AA 2014

AA 2014 Specimen	Thermal simulation Temperature	Vickers Hardness Value (HV)
BM	As-received	157
HAZ region C	590°C	106
HAZ region D	650°C	118

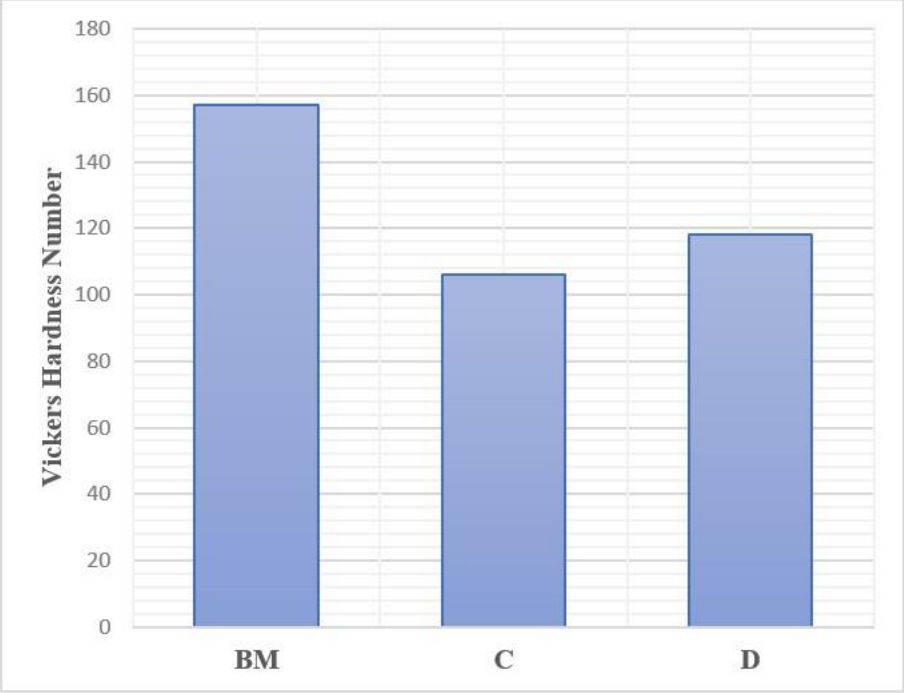

Figure 4. 28: Graphical representation of Vickers Hardness Number in the BM and across the HAZ of AA 2014.

4.7 Optical Micrography

Optical microscopy was carried out on the BM and HAZ regions C and D of AA 2014 which had been thermally simulated to temperatures 590°C and 650°C respectively and the results presented in Figures 4.29 to 4.31. The base metal and the two regions of heat affected zone specimens were oriented in the longitudinal transverse direction (L-T). It was observed that the grains had an orientation parallel to the rolling direction for the BM micrograph Figure 4.29. It is also evident that grain boundaries for the thermally simulated HAZ region C and D are more distinct and more enlarged than those of the BM. Dark particles are also observed on the micrographs and they vary in appearance in the three regions with many of them distributed at the grain boundaries for HAZ regions C and D and others distributed within the matrix of the grain for the BM.

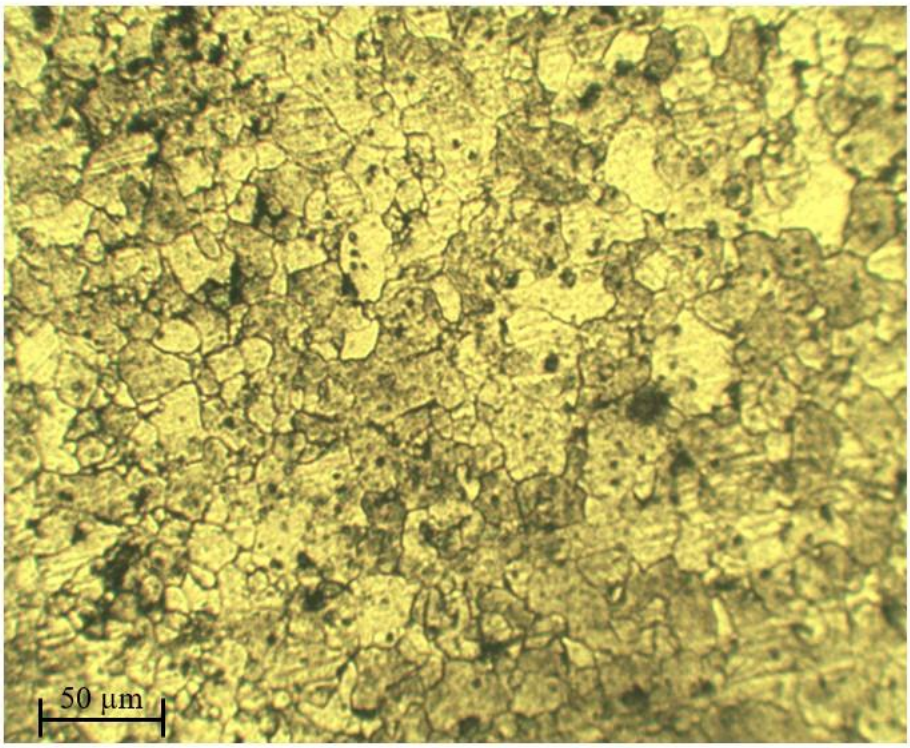

Figure 4. 29: Optical micrographs of AA 2014 alloy BM As-received (200x), Krolls reagent.

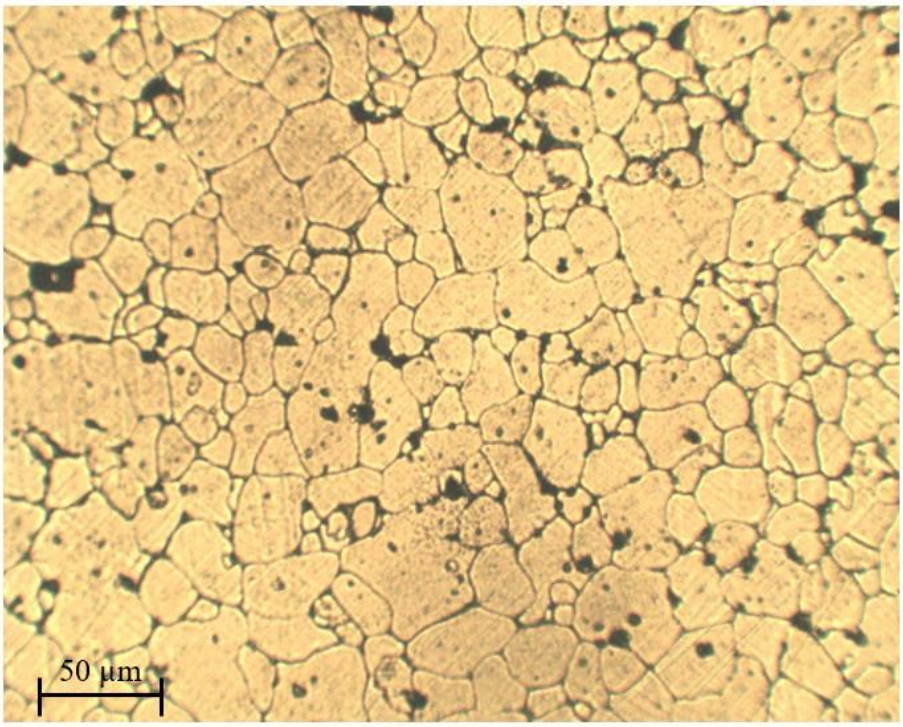

Figure 4. 30: Optical micrographs of AA 2014 alloy region D thermally heated at 650°C (200x), Krolls reagent.

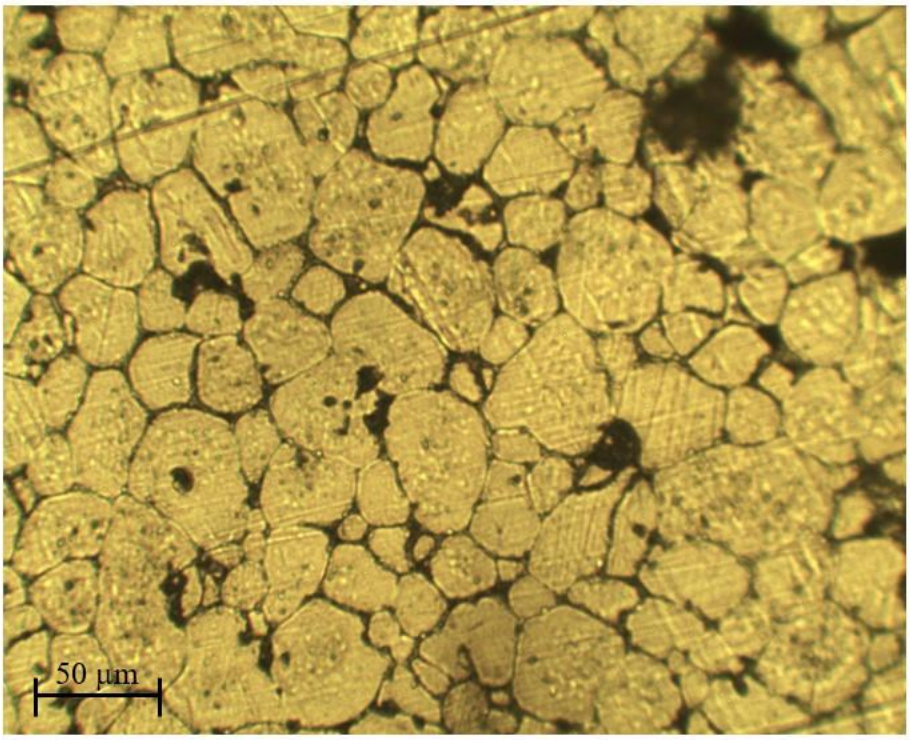

Figure 4. 31: Optical micrographs of AA 2014 alloy region C thermally heated at 590°C (200x), Krolls reagent.

Microstructure characterization of AA 2014 was carried out as discussed in section 3.6.2 and results presented in Table 4.6. A graph showing variation of the grain size in µm and ASTM grain size number of AA 2014 for the BM and two regions of HAZ is as shown in Figure 4.32. The BM recorded the lowest value of grain size whereas the HAZ region C recorded the highest grain size value. There was an increase of grain size in the HAZ region C compared to the HAZ region D.

Table 4.6: ASTM Grain Size Number and Grain size of AA 2014.

AA 2014 Specimen	Thermal simulation Temperature	Average ASTM Grain Size Number, G	Grain size (µm)
BM	As-received	11.811	12
HAZ region C	590°C	9.319	28
HAZ region D	650°C	9.653	25

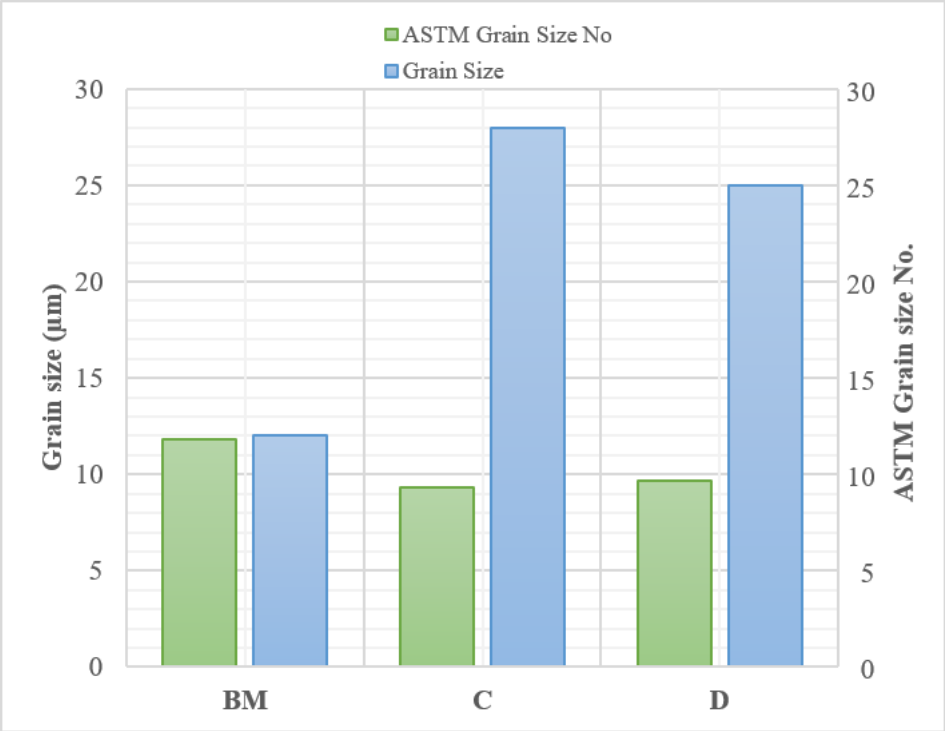

Figure 4.32: ASTM grain size No and Grain size in µm of AA 2014

CHAPTER FIVE: DISCUSSION

5.1 Tensile Properties

The main objective of carrying out the tensile test was to verify whether the BM properties of the AA 2014 used for this test were similar with the AA 2014 supplied by the manufacturer. Tensile tests were conducted on the BM of AA 2014 and results tabulated in Table 4.1. The average values of proof stress ($\sigma_{0.2}$), ultimate stress (σ_{UTS}) and percentage elongation was found to be 401 MPa, 446 MPa and 8.79 percent respectively. The proof stress ($\sigma_{0.2}$), ultimate stress (σ_{UTS}) and percentage elongation of AA 2014 supplied by the manufacturer was 390 MPa, 460 MPa and 11 percent respectively. There was a good correlation between the experimental test results and the material test results supplied by the manufacturer. This test was also helpful in determining the forces to be used during the low cycle fatigue testing as discussed under section 3.5.1.

5.2. Thermal Cycle Simulation

The action of replicating thermal cycle histories (as shown in Figure 4.8) experienced by a specimen during an actual welding process is defined as thermal simulation. The heat produced during welding creates a significant temperature differential in and around the welded region. The heat-affected zone is the region outside the welded joint that is thermally impacted by the welding process. This study focused on studying the weakest regions of the HAZ located 4mm and 5mm from the weld centerline. The simulated heat cycle had an effect on fatigue properties, hardness profile and microstructure of AA 2014 as discussed in sections 5.3 to 5.5. The mechanical characteristics of the base metal and the heat affected zone are strongly related to their microstructures, which are affected by the chemical composition of the material as well as the heat thermal cycles caused by welding operations [139, 140].

Figures 4.5 to 4.7 reflect typical patterns of most arc welds during the actual welding process as outlined in Figure 3.5. Thermal simulation cycles for the HCF, LCF and FCG specimens across the two regions of HAZ was successfully developed as shown in Figure 4.8. Weld heat cycle modeling has been utilized in recent years for weldability research and the identification of microstructure types in the HAZ, which is highly difficult from a microstructure viewpoint due

to its heterogeneous nature. Because of the narrowness of the HAZ, investigating the HAZ of genuine welded connections is difficult [141]. Welding simulation is an appropriate approach for preparing samples that will be used to identify and investigate the various sub-zones of the heat affected zone. This enables the microstructure and characteristics of these sub-zones to be predicted. Research efforts have been directed towards modeling of non-isothermal processes such as those encountered in welding.

Figure 3.5 and 4.8 shows a difference in the time taken to complete the actual thermal cycles experienced during welding and thermal cycles used in this study. This difference was not expected to affect the pattern of HAZ properties since it is the peak temperature and the time experienced by the specimens at the peak temperature that play a critical role during precipitate coarsening and grain growth [132]. The application of thermal profiles to simulate actual welding so as to estimate the properties of the weldment and the HAZ has been investigated by several researchers [104, 105]. Such studies have given rise to the possibility of replicating similar welding conditions through the use of thermal cycle simulations. A good comparison has been reported between actual welding and thermal cycle simulation [132, 142, 143]. Thermal cycles occurring during the process of welding, deviate significantly from equilibrium processes and the size of the HAZ is affected by the welding heat input [144].

There is an observed steep temperature distribution with slight decrease in gradients for the two regions of the HAZ in FCG, LCF and HCF specimens as shown in Figure 4.8. Higher heating and cooling rates are recorded for the HAZ region D as compared to HAZ region C. It is observed that the higher the heating rate, the steeper the gradient and the lower the heating rate the lower the gradient, which was also reported by Akhusama [143]. The crucial parameters characterizing the thermal cycles in the HAZ regions have been attributed to the peak temperature, heating and cooling rates as well as the thermal cycle duration [144]. During the thermal cycle simulation process, heat energy is used just like in the actual welding [132, 143]. The choice of simulation parameters is vital in comparison to the actual welding process in terms of the pattern of energy conversion to heat and subsequent dissipation. This had to be adhered to for the purpose of studying HAZ with properties close to that of the actual welding process. The efficiency of which the input energy is converted is not as critical as the efficiency of heat transfer, energy level and the intensity of energy [45].

5.3 Microstructural Characterization

In this study, optical micrographs of AA 2014 aluminium alloy shown in Figures 4.29 to 4.31were taken at magnification 200x in the L-T direction. The BM microstructure is typical of a rolled material, with elongated grains aligned along the rolling direction and dark pigmented particles. According to Shankar et al [42], BM grains expanded in the rolling direction due to the dispersion of spherical Al_2Cu phases. The particles usually found in the BM are generally Al_2CuMg and Al_7Cu_2Fe or $(Cu,Fe,Mn)Al_6$ [145]. The average grain size of the BM AA 2014 was 12μm. Other studies have found a similar microstructure in the BM [132, 142, 143, 146].

Dark coloured particles which vary in appearance are observed on the micrographs as shown in Figure 4.29 to 4.31. Figure 4.29 (BM) shows the dark particles distributed on both matrix and the grain boundary whereas for the HAZ regions C and D these particles are mainly distributed at the grain boundaries. The varying nature of the dark etching effects could be due to dissolution of some phases during the thermal cycle simulation process. The rate of dissolution and coarsening of the precipitates which affects the mechanical properties is greatly influenced by the heating rate of the thermal simulator. The rate of cooling is also critical as it determines the final microstructure. The specimens were left to cool to room temperature just like in the case of the actual welding process. In thermal cycle simulation, heat energy is used just like in actual welding. The efficiency of heat transfer, energy level and energy intensity influences welding speed and the size of the HAZ [16]. Heating rates are crucial due to their effect on the rate of dissolution and coarsening of precipitates and grain growth.

The grain boundaries for the thermally simulated HAZ regions C and D are much more defined and larger than those for the BM. The difference in appearance of grain boundaries as shown in the three micrographs could be as a result of precipitation of Al_2Cu. Sinhmar and Dwivedi [37] found coarse Al_2Cu precipitates as secondary precipitates in grains of fusion zone in gas tungsten arc welded AA 2014. Al_2Cu precipitates were discovered not only in the weld, but also in the HAZ area. Chong et al [147] found a continuous network of Al_2Cu precipitates that were present in the grain boundaries of an aluminium-copper alloy primary solid solution. If Al_2Cu precipitates occur in welds of AA 2014 alloy as a continuous network of films in the

interdendritic regions, they behave as continuous brittle planes/paths in which fracture might occur [3].

Grain size average of the HAZ region C and D were 28μm and 25μm respectively. The grains are observed to be larger closer to the weld centerline as shown in Figure 4.32(which are 4 mm (region D) and 5 mm (region C) respectively from weld fusion line) as compared to those of the base metal. Therefore, the maximum grain size in these regions closer to the weld centerline could be due to most constituent phases precipitating at the grain boundaries causing grain growth. Most grain growth occurs in the vicinity of peak temperatures, which fully supports the fact that grain growth is a heat activated process [16]. Just like in the welding process, the thermally simulated specimens with peak temperatures closer to the weld centerline experience high peak temperatures and thus will be expected to generate the coarse grain in the HAZ. Thermal simulation temperature for HAZ region C and D, range between the solidus and the liquidus temperature. The phases with low melting temperatures which had melted may have experienced re-solidification while some of the phases may have undergone reversion (coherent precipitates dissolving as a result of high temperatures) as well [143]. This explains the slight decrease in the grain size for the HAZ region D as compared to the HAZ region C.

5.4 Hardness Survey

Following the welding process, hardness measurements give a general idea of the micro structural transformations and the variation of the local mechanical properties [132, 143]. Hardness measurements were performed on thermal simulated AA 2014 specimens and the results were presented in Table 4.5. The BM, HAZ region C and D recorded different values of hardness of 157 HV, 106 HV and 118 HV respectively. The variation of hardness values across the two regions of HAZ is due to the difference in the thermal peak temperature experienced in each region during thermal cycle simulation [132, 143]. Due to the use of targeted heat input, welding of AA 2014 aluminium alloys leads to a dramatic change of the microstructure from the typical grain structure to equiaxed grains, coarse dendritic columnar in the FZ and considerable coarse grains in the HAZ.

There is an observable decrease in hardness for HAZ regions C and D which are found close to the weld FL as compared to the BM. The HAZ Region C located 5 mm from the weld FL was found to have the minimum hardness of 106 HV. The decrease in hardness can be attributed to coarse microstructure as shown in micrographs for HAZ regions C and D. Gorka [142] found that the softening in the HAZ was caused by the coarsening of the metastable phases during welding. The loss in hardness in the HAZ has been established to be a result of-dissolution and coarsening of the hardening precipitates [148, 149].

In this study, the reduction of hardness for HAZ region C and D could be due to dissolution of precipitates that were in the parent metal. The hardness decrease in the HAZ has been reported to be due to interplay between dissolution and re-precipitation which are competing processes [150]. Precipitate coarsening which is severe in region C leads to loss of coherency between the precipitates and the matrix and ultimately the reduction in the mechanical properties. The high temperatures close to the weld centerline are sufficient to dissolve all the precipitates and cooling rates are sufficiently rapid to have the alloying elements retained in the saturated solid solution [132]. The size and percentage of the Al_2Cu phase precipitates in various zones are changed due to precipitate coarsening or/and dissolution [38]. The electrochemical and mechanical characteristics of the weldment are affected by variations in the grain sizes, microstructures and percentage of precipitates in various zones. Grain coarsening and dissolution of coherent Al_2Cu phase in the HAZ might have led to lower hardness values.

There is a slight increase in hardness level for HAZ region D as compared to HAZ region C. Other researchers found a similar trend [16, 143]. Studies [94, 132] hypothesized that the increase in hardness was due to re-precipitation and age hardening of the strengthening precipitates. In addition, they also attributed the rise in hardness to low segregation of strengthening phases and the large fraction of alloying elements remaining in solid solution at the end of the thermal cycle. The slight increase in hardness in region D of the HAZ in AA 2014 could be as a result of re-precipitation and age hardening.

5.5 Fatigue Properties

5.5.1 Fatigue Crack Growth

It is evident that BM and HAZ region C and D exhibit different levels of resistance to FCG. The BM appears to offer the highest resistance to FCG compared to the other two regions of the HAZ. Table 4.4 shows that the FCG exponent *m*, obtained from the slope of the FCG curve, was smaller in the base metal compared to regions C and D. This clearly indicates that the rate of crack growth in the region C and D is higher compared to the BM. Uniform and fine distributed $CuAl_2$ precipitates in the BM hinders the FCG [151]. Dissolution of $CuAl_2$ precipitate in the HAZ regions results in a lower FCG resistance due to less obstacles encountered by the crack as it grows. Dissolution of second phase $CuAl_2$ precipitates during thermal simulation could be the major reason for lower FCG resistance of the HAZ compared to the BM.

Region C and D had lower resistance to FCG. The HAZ region C appears to offer the lowest resistance to FCG compared to the BM and HAZ region D. Region D appears to offer a slightly higher resistance to FCG compared to region C. The optical micrographs in Figures 4.29 to 4.31 revealed that regions C and D had coarse grained microstructure. The coarse grains therefore might have contributed to the weakness in these two regions. Some researchers [151] have pointed out that fine equiaxed grains are less likely to experience solidification cracking than coarse grains. This has been attributed to the equiaxed grains being able to deform to accommodate contraction strains more easily [151]. The relative probability of crack propagation increases with particle thickness [59]. Several researchers [152-155], studied grain size effect on the FCG and concluded that the rate of crack growth was more as the grain size increased.

FCG curves in Figures 4.14 and 4.18show evidence of minimal scatter. The slight fluctuation in FCG curves especially in the HAZ regions C and D is due to the inhomogeneous microstructure which results from the welding thermal cycle [156]. During the rolling process, the intermetallic particles can be crushed in the process, which forms minor cracks. These minor cracks lead to major cracks during the fatigue cyclic loading and they are more favoured at the interface between aluminium matrix and the intermetallics such as Al_7Cu_2Fe [132]. Cracks develop and expand along persistent slip bands, typically slowing down when they approach microstructural obstacles such as hard second phases, nonmetallic inclusions, or, more often, grain boundaries

[157]. These barriers either permanently or temporarily stops the crack depending on the level of stress applied.

Generally, it is affirmed that FCG in the Paris region is less dependent on the microstructure of the material. In this study, the microstructure played a key role in the different properties of the heat affected zone regions. The optimization of the microstructural features for improved resistance of both crack growth and also crack initiation, requires a trade off in the choice of the grain structure or an appropriate distribution of the grain structure. Grain size increase was found to coincide with the decrease in FCG resistance as evidenced in region C and D of the HAZ. The resistance to the growth of microstructurally small cracks is heavily controlled by the microstructure of the material, such as grain size and orientation, as well as the grain boundaries strength [158-162]. Reducing material grain size enhances its endurance strength [163-167]. This is as a result of the mismatch of the fatigue crack faces as they shut, which rises with grain size, decreasing the cycle crack tip opening displacement and, consequently, the rate of crack growth. Nonetheless, growth of short cracks is a plasticity dominated process and because the size of the plastic zone crack tip is governed by grain size, coarse grained microstructures exhibit quicker rates of growth.

Researchers have established that the crack growth conditions are directly influenced by the thermal cycle obtained in the heat affected zone [155]. The thermal cycle greatly influences the final microstructure depending on the peak temperature the region received [16]. Also, it is noted that HAZ region C and D had lower hardness which could be as a result of the coarsening of the strengthening precipitates. The dislocation cell structures mask the influence of grain size in aluminium alloys [127]. The dissolution of strengthening precipitates such as $CuAl_2$ has been reported to greatly influence the FCG negatively [86]. The distribution and size of $CuAl_2$ precipitates play a critical role in deciding the tensile and microhardness properties and consequently the FCG properties [91]. When the particles experience thermal cycle temperatures above 400°C, precipitate dissolution occurs [52]. In this study regions C and D were thermally simulated at temperatures above 400°C. Therefore, the coarsening and dissolution of strengthening precipitates are possibly responsible for the reduced hardness as well as the decrease in FCG resistance in regions C and D. Some researchers investigating welded aluminium alloys made a similar conclusion [168].

5.5.2 Fatigue Strength

High strength aluminium alloys such as AA 2014 aluminium alloy do not reveal any kind of an endurance limit in the stress-life curves at 10^7 cycles. There are limited studies on the long life fatigue and near threshold FCG behaviour done due to time limitations associated with conventional testing procedure [121]. It therefore becomes critical to determine the fatigue strength of the high strength AA 2014 aluminium alloys in the vicinity of the 10^7 cycles. There is a significant difference in the fatigue strength for BM and the two regions of the HAZ of AA 2014 as demonstrated in Figure 4.9. Research has shown that differences in fatigue strength could be attributed to microstructure which produces different conditions for crack initiation and propagation within each specimen [169]. The base metal had the highest fatigue strength of 123 MPa as shown in Figure 4.9 which was estimated using linear interpolation method. HAZ Regions C and D had fatigue strength of 84 MPa and 92 MPa respectively. There was a gradual decrease in fatigue strength on regions close to the weld centerline showing that the thermal cycle significantly affected the material properties in these regions.

The HAZ region C exhibited the lowest fatigue strength. This can be attributed to the precipitate dissolution due to the thermal cycle peak temperatures experienced in this region. This region also recorded the lowest hardness as shown in Figure 4.28. Some researchers found that the fatigue failure was caused by formation of voids, their growth and coalescence and then eventual formation and growth of macroscopic cracks [121]. The transformations in the heat affected regions of heat treatable AA 2014 aluminium alloys are dependent of temperature.

The process of welding and the associated parameters determine the alloy degradation. High heat input and pre-heating deteriorate the fatigue strength and increase the size of the HAZ [124]. The thermal effects in the HAZ have been demonstrated to induce microstructural transformation in heat treated aluminium alloys, modifying the mechanical properties [124]. Formation of low melting intermetallic compounds which segregate along the coarse grain boundary in the HAZ close to the fusion line could be the cause for the drastic decrease in the fatigue strength in the regions close to the weld centerline.

Better fatigue life in the BM can be linked to the presence of finer grains recorded in this region as shown in Figure 4.32. Researchers investigated the influence of particle size on stress-life

curves and established that when the grain size is finer, the fatigue life rises [170-174]. Dislocation slip motion causes fatigue cracks to grow in high strength aluminium alloys that are initially free of significant defects or cracks. Eventually, fatigue cracks spread to final breakage. Metal grain sizes have varied effects on the motion of the slip plane, crack nucleation and crack growth stages of the fatigue process [153, 175]. Upon deformation of metal alloys, some grain boundaries act as obstacle/barrier to slip resulting in dislocations pile up and stress concentrations. The other grain boundaries allow for partial or complete dislocation transfer across borders [176]. The recent development of nanocrystalline alloys, has made the role of grain size on both fatigue growth and nucleation quite controversial [177, 178]. Fine grained materials are thought to have high endurance limits, while large grains slow the fatigue crack growth [55, 59].

Low fatigue life in HAZ regions C and D can also be attributed to coarse microstructure as shown in Figure 4.30 and 4.31. Grain boundaries impede dislocation motion because they separate regions with different crystallographic orientations and/or because they are more disordered than the center of grains. Therefore, the coarse the grains the lesser the grain boundaries that impede dislocation motion thus the lower the fatigue strength. Better fatigue life for the HAZ region C compared to HAZ region D is attributed to the slight increase in grain size in this region. Accordingly, Wagner and Gregory [179] suggested to modify components through the maximization of the total fatigue life in thick sections. They observed that fine grains should be applied at the surface with the provision of good resistance to crack initiation.

5.5.3 Low Cycle Fatigue

From Figure 4.10 it is evident that the BM has better fatigue life as compared to regions C and D of the HAZ. According to Mohamed et al [180], fatigue failure in high strength aluminium alloys is regulated by microcracks nucleation, which spread slowly during cyclic deformation until one of the cracks reaches critical size, resulting in catastrophic failure. At both high and low strains, the HAZ region D had better fatigue life compared to the HAZ region C whereas the BM had the best fatigue life. This observation can be linked to the microstructure of these two regions of HAZ. Large precipitates are responsible for the creation of fatigue cracks in high strength

aluminium alloys such as AA 2014. Strain localization takes place at cyclic deformations in these materials. This leads to increased dislocation densities, large slip offsets or stress levels in grain borders and an early initiation a fatigue crack, either through grain limits or inclusion fracture [180]. Ebara [181] showed that grain size has an effect on LCF strength not only for high strength maraging steel with grain size of 60, 20 and 100 μm but also for high strength AA 2014 alloys. The grain refinement in these materials increases LCF crack initiation and growth resistance.

Shorter fatigue life in the HAZ regions C and D can be attributed to the coarse microstructureas shown in Figure 4.30 and 4.31 which registered larger values of grain sizes compared to the BM. The impact of grain size on high strength aluminium alloys AA 2014 and AA 2024 [180, 182] can be expounded in terms of compatibility of strain which provides the basis for grain boundary impacts. The necessity to preserve continuity between randomly oriented neighbors of the plastic strain across grain borders means that several shear modes or slip systems can be operational if the material is deformed as a whole. With increasing stress levels, the number of slips necessary to ensure continuity increases. While strain compatibility enables numerous slip systems to operate, the latter causes strain hardening rate to rise due to interaction between individual systems creating dislocation barriers, which affects dislocation mobility and mean free path in the interior of the grain.

Comparing fatigue life of AA 2014 at low and high strains in Figure 4.10, it is evident that fatigue life is better at low strains than high strains. According to the findings of Llanes at al [183], the grain size impact was reduced at high plastic strain amplitude and more prominent at low plastic strain amplitude. According to Mughrabi et al [184], grain size impacts the slip character of material, and the beginning of numerous slips occurs at low plastic strain amplitudes in coarse-grain copper than in fine grain copper. In the low amplitude domain, grain size has a considerable influence on the cyclic stress-strain response of polycrystalline copper. According to Morrison and Moosbrugger [172], coarse grained copper has a greater saturation stress than fine grained copper, and at high stresses, cracks begin to form intergranularly at all grain sizes. This explains the phenomena in Figure 4.10 in which at a higher strain the three regions (BM, HAZ region C and D) tend to tend to be closer to each other than at lower strain.

CHAPTER SIX: CONCLUSIONS AND RECOMMENDATIONS

6.1 Conclusions

The conclusions below were drawn from this study concerning the effects of thermal cycle simulation on the microstructure, FCG resistance, LCF, fatigue strength and hardness profiles in the HAZ of AA 2014 aluminium alloy.

a. The heat affected zone is not a homogeneous zone but it comprises of different sub-zones and each sub-zone has its microstructure (grain size) which depends on peak temperature.
b. Just like the welding process, thermal cycle simulation affects the mechanism of precipitate formation and distribution and also the size of the grains. Grains are coarsest at region C (28μm) which represents 5 mm from FL while the BM has the finest grains (12μm).
c. The weakest link in the HAZ is the region C which is 5 mm from the FL since it has the coarsest microstructure (28μm), the lowest hardness (106 HV), low FCG resistance (m=4.8050), low fatigue strength (84 MPa) and least resistance to LCF.

6.2 Recommendations

a. Fractography studies on the fractured AA 2014 aluminium alloy specimen from the fatigue strength tests may be conducted to establish the fracture characteristics, to determine the failure mode and also the effect of intermetallics and/or precipitates involved in fatigue failure.
b. Study of X-ray diffraction (XRD) patterns obtained from aluminium alloy samples submitted to different thermal cycle's simulation can be carried out to demonstrate whether the welding process produces enough heat to cause phase changes within the material.
c. SEM studies should be conducted on thermally simulated HAZ regions of AA 2014 to establish if there exist precipitate dissolution/re-precipitation.
d. This study, through investigating fatigue properties, has shown that the weakest region in the HAZ is 5 mm from the weld centerline. It is therefore necessary to carry out further studies to confirm the reason behind this and also find a suitable joining process or post weld treatment that can improve fatigue properties at this region of the HAZ.
e. This study involved investigating FCG properties of a 2.66 mm thick AA 2014 specimen at R- ratio of 0.2. Further study should be carried out to investigate the effect that both specimen size and R-ratio has on FCG rate of AA 2014 specimen.
f. Further work on thermal simulation should be carried out to compare between the thermal cycle histories in the muffle furnace and the Gleeble simulator. The main challenge would be fitting the FCG test specimen, however, the use of other test specimens (hardness, fatigue strength, LCF and microstructure characterization) would bring out the difference if any.

REFERENCES

1. T. Dursun and C. Soutis, *Recent Developments in Advanced Aircraft Aluminium Alloys*, Materials and Design **56**, 862–871 (2014).
2. AA 2014 Aluminium Alloy Datasheets, Smiths Metals Ltd. Retrieved from https://www.smithmetal.com/2014a.htm, (2020-12-27).
3. W. L. Burch, E. A. Dolega and G. F. Kappelt, *Fusion Welding of 2014 Aluminium Alloy*, Bell Laboratory Report, Revision A (1962).
4. Marks' Standard Handbook for Mechanical Engineers, 8th Edition, McGraw Hill Book Company, 6-56 (July 1, 1978).
5. F. Kutner and G. Lang, *The Influence of Alloying Elements on the Density of Super-Purity Aluminium*, Aluminium, **46** (**10**), 691-694 (1970).
6. A. A. Saleh, *Effect of Heat Treatment on the Mechanical Properties of AA 2014 Alloy*, Contemporary Engineering Sciences, **11** (**69**), 3409–3419 (2018).
7. M. Gavgali and B. Aksakal, *Effects of Various Homogenisation Treatments on the Hot Workability of Ingot Aluminium Alloy AA 2014*, Materials Science and Engineering A, **254**, 189–199 (1998).
8. P. D. Merica, R. G. Waltenberg, and H. Scott, *Heat Treatment of Duralumin*, Sci. Pap. National Bureau of Standards **15**, 271-316 (1919).
9. P. Bassani, E. Gariboldi and G. Vimercati, *Calorimetric Analyses on Aged Al–4.4Cu–0.5Mg–0.9Si–0.8Mn Alloy (AA 2014 grade)*, J. Therm. Anal. Calorim. **87** (**1**), 247–253 (2007).
10. D. J. Chakrabarti and D. E. Laughlin, *Phase Relations and Precipitation in Al–Mg–Si Alloys with Cu Additions*, Prog. Mater. Sci. **49**, 389–410 (2004).
11. J. R. Scully, D.E. Peebles, A.D. Romig, D.R. Frear and C.R. Hills, *Metallurgical Factors Influencing the Corrosion of Aluminum, Al-Cu, and Al-Si Sputtered Thin Films in Dilute HF Solution*, Metall. Trans. A. **23**, 2641-2655 (1992).
12. C. Badini, F. Marino and E. Verne, *Calorimetric Study on Precipitation Path in 2024 Alloy and its SiC Composite*, Mater. Sci. Eng. A **191**, 185–191 (1995).

13. R. D. Doherthy, R. W. Cahn and P. Haasen, Physical Metallurgy, Elsevier, Amsterdam (1996).
14. T. Sheppard, *Extrusion of Aluminium Alloys*, Kluwer Academic, Dordrecht, **5**, 205– 245 (1999).
15. E. Morris, *Precipitation Hardening of Aluminum Alloys*, Metallurgical Transactions A, **6 (4)**, 625–630 (1975).
16. M. W. Sakwa, An Investigation of Heat Flow, Precipitate Formation and Grain Growth in the HAZ of Aluminium Alloy Weldment, MSc Thesis, University of Nairobi, (2000).
17. C. C. Griffee, G. A. Jensen and T. L. Reinhart, *Factors Influencing the Quality and Properties of Aluminium Lithium Welds* in Proc 5th Intl. Al-Li Cnf. 1425-1434 (1989).
18. R. Sridevi, P. Venkadeshwaran, R. Sakthivel, R. Ahamedmeeran and K. Chandrasekaran, *Effect of Welding Parameters on Mechanical Properties and Microstructure of AA 2014 using GMAW process*, **10 (15)**,12163-12173 (2015).
19. G. O. Rading and J. T. Berry, *A Model for the Heat Affected Zone Hardness Profiles in Al-Li-X Alloys*, Welding Journal, **77** (**9**), 383-387 (1998).
20. N. Dowling, Mechanical Behavior of Materials: Engineering Methods for Deformation, Fracture and Fatigue, 4th Edition, Prentice Hall, Upper Saddle River, 357-550 (2012).
21. P. J. E. Forsyth, *Fatigue Problems in Service*: Aircraft Structures, Metal Science, **11**, 293-302 (1977).
22. J. Downer, *The Limits of Knowledge and the Sociology of Inevitable Failure*, American Journal of Sociology, **117** (**3**), 725-762 (2011).
23. C. P. Blankenship and E. A. Starke, *The Fatigue Crack Growth Behaviour of the Al-Cu-Li Alloy Weldalite 049*, Fatigue and Fracture of Engineering Materials and Structures, **14** (**1**), 103-114 (1991).
24. D. L. Chen and M. C. Chaturvedi, *Near-Threshold Fatigue Crack Growth Behavior of 2195 Aluminium–Lithium-Alloy – Prediction of Crack Propagation Direction and Influence of Stress Ratio*, Metallurgical and Materials Transactions, **31**, 1531–1541 (2000).
25. J. E. Hatch, Aluminium Properties and Physical Metallurgy, Aluminium Association Inc. and ASM International, (1984).

26. F. Tariq, N. Naz and R. A. Baloch, *Characterization of Material Properties of 2xxx Series Al-Alloys by Non-Destructive Testing Techniques*, Journal of Nondestructive Evaluation, **31** (**1**), 17–33 (2011).
27. C.P. Harper, Effect of alumina particle additions on the aging kinetics of 2014-aluminium matrix composites, MSc Thesis, University of Evansville, 1983.
28. S. Abis, M. Massazza, P. Mengucci and G. Riontino, *Early Ageing Mechanisms in a High-Copper Al-Cu-Mg Alloy*, Scr. Mater., **45 (6)**, 685–691 (2001).
29. P. D. Merica, R. G. Waltenberg and J. R. Freeman, *Constitution and Metallography of Aluminium and Its Light Alloys with Copper and with Magnesium*, Trans. Am. Inst. Min. Metall. Eng., **64**, 3-25 (1921).
30. P. D. Merica, R. G. Waltenberg and J. R. Freeman, *Constitution and Metallography of Aluminium and Its Light Alloys with Copper and with Magnesium*, Sci. Pap. Bur. Stand. **15**, 105-119 (1919).
31. W. Bolten, Engineering Material Technology, prentice hall (1998).
32. H. B. Cary and S. C. Helzer, Modern Welding Technology 6th Edition, Prentice Hall, Upper Saddle River, 715 (2005).
33. A. F. Norman, V. Drazhner and P. B. Prangnell, *Effect of Welding Parameters on the Solidification Microstructure of Autogenous TIG Welds in an Al–Cu–Mg–Mn Alloy*, Materials Science and Engineering A, **259**, 53–64 (1999).
34. R. Sokkalingam, K. Venkatesan, S. S. Sabari, S. Malarvizhi and V. Balasubramanian, *Effect of Post Weld Aging Treatment on Tensile Properties of GTAW Welded Armour Grade AA2519-T87 Aluminium Alloy Joints*, International Journal of Research in Engineering and Technology, **3** (**11**), 316-320 (2014).
35. R. A. Owen, R. V. Preston, P. J. Withers, H. R. Shercliff and P. J. Webster, *Neutron and Synchrotron Measurements of Residual Strain in TIG Welded Aluminium Alloy 2024*, Materials Science and Engineering A, **346**, 159-167 (2003).
36. E. R. Bohnart, TIG handbook for GTAW Gas Tungsten Arc Welding, Miller Electric Mfg. Co. (2002).

37. S. Sinhmar and D. K. Dwivedi, *A Study on Corrosion Behavior of Friction Stir Welded and Tungsten Inert Gas Welded AA 2014 Aluminium Alloy*, Corrosion Science, **133**, 25-35 (2018).
38. H. Aydın, A. Bayram and I. Durgun, *the Effect of Post-Weld Heat Treatment on the Mechanical Properties of 2024-T4 Friction Stir-Welded Joints*, Materials & Design, **31** (**5**), 2568–2577 (2010).
39. K. H. Hou and W. A. Baeslack, *Effect of Solute Segregation on the Weld Fusion Zone Microstructure in Co_2 Laser Beam and Gas Tungsten Arc Welds in Al-Li-Cu alloy 2195*, **15**, 208–213 (1996).
40. W. A. Baeslack and K. H. Hou, *Characterization of the Heat-Affected Zone in Gas Tungsten Arc Welded Aluminium Alloy 2195-T8*, Journal of Materials Science Letters, **15** (**3**), 239–244 (1996).
41. S. D. Dumolt, An Investigation of the Microstructural Changes in the Heat Affected Zone of Age Hardenable Aluminium Alloys Using Transmission Electron Microscopy, PhD Dissertation, Carnegie-Mellon University, Pittsburg, PA, July 1983.
42. M. P. Shankar, R. Sokkalingam, K. Sivaprasad and V. Muthupandi, *Correlating Tensile Properties with Microstructures of Various Regions in Gas Tungsten Arc Welded AA 2014 Alloy*, Materials Science Forum, **969**, 22–26 (2019).
43. R. P. Martukanitz, C. A. Natalie and J. O. Knoefel, *The Weldability of an Al-Li-Cu Alloy*, J. Metals, **39**, 38-42 (1987).
44. A. J. Sunwoo and K. Morris, *Influence of Intrinsic and Extrinsic Factors on Mechanical Properties of 2090 Aluminium Alloy Weldement*, Mat. Sci. Tech, **7**, 965-971 (1991).
45. A. J. Sunwoo, E. L. Bradley and J. W. Morris, *Effects of Heat Affected Zone Peak Temperature on the Microstructure and Properties of 2090 Al Alloy*, Metall. Trans, 21A, 2795-2804 (1990).
46. O. R. Myhr and O. Grong, *Process Modelling Applied to 6082-T6 Aluminium Weldments-I*: Reaction Kinetics, Acta Metal. Mater, **39** (**11**), 2693-2702 (1991).
47. O. R. Myhr and O. Grong, *Process Modelling Applied to 6082-T6 Aluminium Weldements- II Application of Model*, Acta Metal. Mater, **39** (**11**), 2703-2708 (1991).

48. C. E. Cross, L. W. Loechel and G. F. Braun, *Weldalite^{tm} 049 Weld Development for Aerospace Tankage*, in Al-Li alloys DGM, M. Peters and P. J. Winkler Eds, Oberursel, 1165-1170 (1992).
49. B. Biermann, R. Kupfer, A. Lang and H. W. Bergmann, *Laser Cutting and Welding of Aluminium Sheets*, in Al-Li alloys DGM, M. Peters and P. J. Winkler Eds, Oberursel, 1159-1164 (1992).
50. S. Oliviera, F.A. Darwish and I. G. Solorzano, *Microstructural Characterization and Fatigue Behaviour of 2090 Al-Li Alloy Weldment*, in Al-Li alloys DGM, M. Peters and P. J. Winkler Eds, Oberursel, 545-550 (1992).
51. Y. Erjing, L. Ganhong and W. Zhaoqing, *Microstructure and Mechanical Properties of Al-Li Alloy 8090 Weldments*, in Al-Li alloys DGM, M. Peters and P. J. Winkler Eds, Oberursel, 1191-1196 (1992).
52. I. N. Frdlyander, A. M. Dritz and T. V. Krymova, *High Strength Weldable 1460 Alloy for Cryogenic Application*, in Al-Li alloys DGM, M. Peters and P. J. Winkler Eds, Oberursel, 1245-1250 (1992).
53. T. S. Srivastsan and T. S. Sudarshan, *Welding of Lightweight Aluminium Alloys*, Weld. J. Res. Suppl, **70**, 173- 185 (1991).
54. A. J. Sunwoo and J. W. Morris, *Aging Characteristics of Electron Beam and Gas Tungsten Arc Fusion Zones of Al-Cu-Li Alloy 2090*, Metal. Trans. A **22**, 903-913 (1991).
55. R. Stephens, A. Fatemi, H. Fuchs, Metal Fatigue in Engineering, John Wiley and Sons, Inc, NY, Second Edition, 136-147 (2001).
56. S. T. Rolfe, J. M. Barsom and T. Stanley, Fracture and Fatigue Control in Structures Applications of Fracture Mechanics, Third Edition, West Conshohocken, Pa ASTM, (1999).
57. A. Siqueira, C. Baptista, O. Guimarães, and C. Ruchert, *Describing the Total Fatigue Crack Growth Curves for Aluminum Alloys with an Exponential Equation*, Procedia Engineering, 2 (1), 1904-1914 (2010).
58. P. C. Paris and F. Erdogan, *A Critical Analysis of Crack Propagation Laws*, Journal of Basic Engineering, **18 (4)**, 528–534 (1963).

59. S. Suresh, Fatigue of Materials, Second Edition, Cambridge University Press, Cambridge, UK, (1998).
60. R. G. Forman, V. E. Kearney and R.M. Engle, *Numerical Analysis of Crack Propagation in a Cyclically Loaded Structure*, ASME Transactions Journal of Basic Engineering, **89**, 459 (1967).
61. S. Bailey, N. Baldini, E. Elrone, K. Peters and J. Rosiak, Annual Book of ASTM Standards: Metals Test Methods and Analytical Procedures, ASTM Publishing, 3.01 (3), 627-653 (2004).
62. J. Newman and R. Piascik, *Interactions of Plasticity and Oxide Crack Closure Mechanisms Near the Fatigue Crack Growth Threshold*, International Journal of Fatigue, **26**, 923-927 (2004).
63. W. Elber, *The Significance of Fatigue Crack Closure, Damage Tolerance in Aircraft Structure*, ASTM STP 486, 230–247 (1971).
64. W. T. Wu, Z. Y. Liu, S. Bai, F. D. Li, M. Liu and A. Wang, *Anisotropy in Fatigue Crack Propagation Behavior of Al-Cu-Li Alloy Thick Plate*, Materials Characterization, **131**, 440–449 (2017).
65. J. Chen, Q. L. Pan, X. H. Yu, M. J. Li, H. Zou, H. Xiang, Z. Q. Huang and Q. Hu, *Effect of Annealing Treatment on Microstructure and Fatigue Crack Growth Behavior of Al-Zn-Mg-Sc-Zr Alloy*, Journal of Central South University **25** (**5**), 961–975 (2018).
66. H. Aydin, M. Tutar, A. Durmus, A. Bayram and T. Sayaca, *Effect of Welding Parameters on Tensile Properties and Fatigue Behavior of Friction Stir Welded 2014-T6 Aluminium Alloy*, Transactions of Indian Institute of Metal, **65** (**1**), 21–30 (2012).
67. A. Zabett and A. Plumtree, *Microstructural Effects on the Small Fatigue Crack Behaviour of an Aluminium Alloy Plate*, Fatigue and Fracture of Engineering Materials and Structures, **18**, 801-809 (1995).
68. A. Merati, *A Study of Nucleation and Fatigue Behaviour of an Aerospace Aluminium Alloy 2024-T3*, Int. Journal of Fatigue, **27**, 33-44 (2005).
69. R. Gurbuz and S. P. Alpay, *The Effect of Coarse Second Phase Particles on Fatigue Crack Propagation of an Al-Zn-Mg-Cu alloy*, Metallurgical Transactions, **30**, 1373-1376 (1994).

70. M. Dong, J. Shen, S. Lai and J. Chen, *Effect of Heat Input on the Microstructure and Mechanical Properties of TIG Arc Butt-Welded AZ61 Magnesium Alloy Plates*, Materials Characterization, **60**, 1583-1590 (2009).
71. T. Kawana and H. Kokawa, *A Physical Metallurgy and Materials Science,* Quarterly Journal of the Japanese Welding Society, **1**, 392-398 (1983).
72. J. F. Lancaster, Metallurgy of Welding, 6th Edition. Wood Head Publishing Ltd. (1999).
73. L. Edwards, M. E. Fitzpatrick, P. E. Irving, I. Sinclair, X. Zhang and D. Yapp, *An Integrated Approach to the Determination and Consequences of Residual Stress on the Fatigue Performance of Welded Aircraft Structures*, Journal of ASTM International **3** (**2**), 1-17 (2006).
74. G. Bussu and P. E. Irving, *The Role of Residual Stress and Heat Affected Zone Properties on Fatigue Crack Propagation in Friction Stir Welded 2024-T351 Aluminium Joints*, International Journal of Fatigue **25**, 77-88 (2003).
75. O. A. Hatamleh, *Comprehensive Investigation on the Effects of Laser and Shot Peening on Fatigue Crack Growth in Friction Stir Welded AA 2195 Joints*, International Journal of Fatigue, **31** (**5**), 974–988 (2009).
76. R. Doglione and M. Bartolone, *Fatigue Crack Propagation in 2195-T8 Aluminium Alloy Plate*, Proceedings of the 9th International Conference on Aluminium Alloys, Politecnico di Torino, c.so Duca degli Abruzzi 24, 10129 Torino, Italy (2004).
77. V. M. J. Sharma, K. S. Kumar, B. N. Rao and S. D. Pathak, *Fatigue Crack Growth of AA2219 under Different Aging Conditions*, Materials Science and Engineering A, **528**, 4040-4049 (2011).
78. Z. Q. Zheng, B. Cai, T. Zhai and S. C. Li, *The Behavior of Fatigue Crack Initiation and Propagation in AA2524-T34 Alloy*, Materials Science and Engineering: A, **528**, 2017-2022 (2011).
79. H. Li, J. Gao and Q. Li, *Fatigue of Friction Stir Welded Aluminium Alloy Joints*, A Review of Applied Sciences, **8** (**12**), 2626 (2018).
80. R. I. Rodriguez, J. B. Jordon, P. G. Allison, T. Rushing and L. Garcia, *Low-Cycle Fatigue of Dissimilar Friction Stir Welded Aluminium Alloys*, Materials Science and Engineering A, **654**, 236–248 (2016).

81. Y, Besel, M. Besel, U. A. Mercado and T. Kakiuchi, *Influence of Local Fatigue Damage Evolution on Crack Initiation Behavior in a Friction Stir Welded Al-Mg-Sc Alloy*, International Journal of Fatigue, **99**, 151–162 (2017).
82. C. He, Y. Liu, J. Dong, Q. Wang, D. Wagner and C. Bathias, *Fatigue Crack Initiation Behaviors Throughout Friction Stir Welded Joints in AA7075-T6 in Ultrasonic Fatigue*, International Journal of Fatigue, **81**, 171–178 (2015).
83. D. A. S. Hrishikesh, D. Chakraborty and T. K. PAL, *High-Cycle Fatigue Behavior of Friction Stir Butt Welded 6061 Aluminium Alloy*, Transactions of Nonferrous Metals Society of China, **4**, 648–656 (2014).
84. C. Deng, R. Gao, B. Gong, T. Yin and Y. Liu, *Correlation Between Micro-Mechanical Property and Very High Cycle Fatigue (VHCF) Crack Initiation in Friction Stir Welds of 7050 Aluminium Alloy*, International Journal of Fatigue, **104**, 283–292 (2017).
85. M. R. Sonne, P. Carlone, G. S. Palazzo and J. H. Hattel, *Numerical Modeling of AA2024-T3 Friction Stir Welding Process for Residual Stress Evaluation, Including Softening Effects*, Engineering Materials, **611–612**, 1675–1682 (2014).
86. P. Sivaraj, D. Kanagarajan and V. Balasubramanian, *Fatigue Crack Growth Behaviour of Friction Stir Welded AA7075-T651 Aluminium Alloy Joints*, Transactions of Nonferrous Metals Society of China, **24**, 2459-2467 (2014).
87. S. Kou, Welding Metallurgy, John Wiley and Sons (1987).
88. A. O. Kluken and B. B. Rneklett, *A Study of the Mechanical Properties for Aluminium GMA Weldments*, Welding Journal, **76** (**2**), 39-44 (1997).
89. G. Mathers, Welding of Aluminium and Its Alloys, Woodhead Publishing Limited Cambridge, England (2002).
90. A. Romeyn, Welding of Al-Zn-Mg (7xxx) Alloys, Department of Defence, Materials Research Laboratories Report, (1983).
91. W. Zhou, Problems in Welding of High Strength Aluminium Alloys, Singapore Welding Society Newsletter, September (1999).
92. T. Senthilkumar, V. B. Subramanian and M. S. Babu, *Effect of Pulsed Current GTAW Parameters on Fusion Zone Microstructure of AA6061*, International Journal of Metals and Materials, **13** (**4**), (2007) 345-351.

93. R. Ranganatha, V. A. Kumar, V. S. Nandi, R. R. Bhat, B. K. Muralidhara, *Multistage Heat Treatment of Aluminium Alloy AA 7049*, Transactions of Nonferrous Metals Society of China, **23**, 1570-1575 (2013).
94. G. M. Reddy, A. A. Gokhale and K. P. Rao, *Optimization of Pulse Frequency in Pulsed Current Gas Tungsten Arc Welding of Aluminium Lithium Alloy Sheets*, Material Science and Technology, **14**, 61-66 (1998).
95. M. Chemingui, M. Khitouni, K. Jozwiak, G. Mesmacque and A. Kolsi, *Characterization of the Mechanical Property Changes in an Al-Zn-Mg Alloy After a Two-Step Aging Treatment at 70° and 135°C*, Materials and Design, **31** (**6**), 3134-3139 (2010).
96. Y. E. Ma, Z. Zhao, B. Liu and W. Li, *Mechanical Properties and Fatigue Crack Growth Rates in Friction Stir Welded Nugget of 2198-T8 Al-Li Alloy Joints*, Materials Science and Engineering: A, **569**, 41-47 (2013).
97. L. Yan and J. Fan, *In-Situ SEM Study of Fatigue Crack Initiation and Propagation Behavior in 2524 Aluminium Alloy*, Materials & Design, **110**, 592-601 (2016).
98. W. B. Shou, D. Q. Yi, H. Q. Liu, C. Tang, F. H. Sheu, and B. Wang, *Effect of Grain Size on the Fatigue Crack Growth Behavior of 2524-T3 Aluminium Alloy*, Archives of Civil and Mechanical Engineering, **16**, 304-312 (2016).
99. X. Qianfan, Diesel Engine System Design, Woodhead Publishing, 113-119 (2011)
100. B. K. Parida, *Fatigue Testing*, Encyclopedia of Materials Science and Technology, 2994–2999 (2001).
101. L. F. Coffin, *A Study of the Effects of Cyclic Thermal Stresses on a Ductile Metal*, Transactions of the American Society of Mechanical Engineers, **76**, 923–949 (1954).
102. S. S. Manson, Behaviour of Materials Under Conditions of Thermal Stress, Nat. Advis. Comm. Aero, Tech. Note 2933, (1954)
103. W. J. O'Donnell and B. F. Langer, *Fatigue Design Basis for Zircaloy Components*, Nuclear Science and Engineering, **20** (**1**), 1–12 (1964).
104. F. M. Shuaeib, K. Y. Benyounis and M.S. J. Hashmi, Material Behavior and Performance in Environments of Extreme Pressure and Temperatures, Reference Module in Materials Science, Elsevier, Dublin City University, Dublin, Ireland (2017).

105. Q. Zhang, C. Zhang, J. Lin, G. Zhao, L. Chen, and H. Zhang, *Microstructure Analysis and Low-Cycle Fatigue Behavior of Spray-Formed Al–Li Alloy 2195 Extruded Plate*, Materials Science and Engineering A, **742**: 773-787 (2019).

106. P. S. De, R. S. Mishra, J. A. Baumann, *Characterization of High Cycle Fatigue Behavior of a New Generation Aluminium Lithium Alloy*, Acta Mater. **59** (**15**) 5946–5960 (2011).

107. K. T. V. Rao and R. O. Ritchie, *Fatigue of Aluminium–Lithium Alloys*, Int. Mater. Rev. **37** (**1**) 153–186 (1992).

108. A. A. Csontos and E. A. Starke, *The Effect of Inhomogeneous Plastic Deformation on the Ductility and Fracture Behavior of Age Hardenable Aluminium Alloys*, Int. J. Plast. **21** (**6**), 1097–1118(2005).

109. A. Deschamps, B. Decreus, F. De Geuser, T. Dorin and M. Weyland, *The Influence of Precipitation on Plastic Deformation of Al–Cu–Li Alloys*, Acta Mater, **61** (**11**), 4010–4021 (2013).

110. T. Dorin, F. De Geuser, W. Lefebvre, C. Sigli, and A. Deschamps, *Strengthening Mechanisms of T1 Precipitates and Their Influence on the Plasticity of an Al–Cu–Li Alloy*, Mater. Sci. Eng. A, **605,** 119–126 (2014).

111. M. Lewandowska, J. Mizera and J. Wyrzykowski, *Cyclic Behaviour of Model Al–Li Alloys, Effect of the Precipitate State*, Materials Characterization, **45** (**3**), 195–202 (2000).

112. D. Khireddine, R. Rahouadj and M. Clavel, *The Influence of δ′ and S′ Precipitation on Low Cycle Fatigue Behaviour of an Aluminium Alloy*, Acta Metall. **37** (**1**), 191–201 (1989).

113. J. Szusta and A. Sewryn, *Experimental Study of the Low-Cycle Fatigue Life under Multiaxial Loading of Aluminium Alloy EN AW-2024-T3 at Elevated Temperatures*, International Journal of Fatigue, **96**, 28-42 (2017).

114. H. Hao, D. Ye and C. Chen, *Strain Ratio Effects on Low-Cycles Fatigue Behaviour and Deformation Microstructure of 2124-T851 Aluminium Alloy*, Materials Science and Engineering: A, **605**, 151-159 (2014).

115. S.M. Liu and Z.G. Wang, *Fatigue Properties of 8090 Al–Li Alloy Processed by Equal-Channel Angular Pressing*, Scr. Mater. **48** (**10**), 1421–1426 (2003).

116. M. Wang, Z. Liu, Z. Liu, S. Yang, Y. Weng and T. Song, *Effects of Sc on Microstructure and Low-Cycle Fatigue Properties of Al–Li Alloy*, Mater. Sci. Eng. A **483–484,** 448–451 (2008).

117. W. Z. Han, A. Vinogradov and C. R. Hutchinson, *On the Reversibility of Dislocation Slip During Cyclic Deformation of Al Alloys Containing Shear-Resistant Particles*, Acta Mater. **59** (**9**), 3720–3736 (2011).

118. K. Hockauf, M. F. X. Wagner, T. Halle, T. Niendorf, M. Hockauf and T. Lampke, *Influence of Precipitates on Low-Cycle Fatigue and Crack Growth Behavior in an Ultrafine-Grained Aluminium Alloy,* Acta Mater. **80,** 250–263 (2014).

119. R. L. Carlson and G.A. Kardomateas, An Introduction to Fatigue in Metals and Composites, Chapman and Hall, London (1996).

120. R. Nandan, T. DebRoy and H. K. D. H. Bhadeshia, *Recent Advances in Friction-Stir Welding Process, Weldment Structure and Properties*, Progress in Materials Science, **53** (**6**), 980–1023 (2008).

121. Q. Y. Wang, T. Li, and X. G. Zeng, *Gigacycle Fatigue Behaviour of High Strength aluminium alloys*, Procedia Engineering, **2**, 65-70 (2010).

122. T. O. Mbuya, Analysis of Microstructure and Fatigue Micro-mechanisms in Cast Aluminium Piston Alloys, PhD Thesis, University of Southampton (2011).

123. C. Fares, L. Hemmouche, M. A. Belouchrani, A. Amrouche, D. Chicot and E. S. Puchi-Cabrera, *Coupled Effects of Substrate Microstructure and Sulphuric Acid Anodizing on Fatigue Life of a 2017A Aluminium Alloy*, Materials & Design, **86**, 723-734 (2015).

124. S. Missori and A. Sili, *Mechanical Behaviour of 6082-T6 Aluminium Alloy Welds*, Materials Science and Technology, **18** (**1**), 12-18 (2000).

125. M. S. Alam, Structural Integrity and Fatigue Crack Propagation Life Assessment of Welded and Weld Repaired Structures, PhD Thesis, Louisiana State University, (2005).

126. N. T. Nguyen and M. A. Wahab, *The Effect of Residual Stresses and Weld Geometry on the Improvement of Fatigue Life*, Journal of Materials and Processing Technology, **48**, 583-588 (1995).

127. G. E. Dieter, Mechanical Metallurgy, McGraw-Hill Inc, 3, 417-419 (1986).

128. O. Oluwole and O. J. Ajibade, *Effect of Welding Current and Voltage on the Mechanical Properties of Wrought (6063) Aluminium Alloy*, Materials Research, **13** (**2**), 125-128 (2010).

129. E. Gharibshahiyan, A. Honarbaksh, N. Parvin and M. Rahimian, *The Effect of Microstructure on Hardness and Toughness of Low Carbon Welded Steel Using Inert Gas Welding*, Materials and Design, **32**, 2042-2048 (2011).

130. ASTM E8-04, Standard Test Method for Tension Testing of Metallic Materials, ASTM International, West Conshohocken, PA, (2004).

131. G. O. Rading, Fatigue Crack Propagation in a Structural Steel, Applications of Fracture Mechanics, MSc Thesis, University of Nairobi, (1983).

132. S. K. Rotich, Fatigue Crack Growth and Fatigue Strength Characteristics in the HAZ of AA 7075-T651, MSc Thesis, University of Nairobi, (2017).

133. ASTM E647, Standard Test Method for Measurement of Fatigue Crack Growth Rates, Annual Book of ASTM Standards, 646-666 (1989).

134. D. C. Maxwell and T. Nicholas, *Method for Generation of Haigh Diagram for High Cycle Fatigue*, Fatigue and Fracture Mechanics, **29**, 1321 (1999).

135. H. J. Gough, Fatigue of Metals, Ernst Benn Limited, London (1926).

136. ASTM E606, Standard Practice for Strain-Controlled Fatigue Testing,Annual Book of ASTM Standards, 646-666 (1989).

137. ASTM E112, Standard Test Method for Determining the Average Grain Size, Annual Book of ASTM Standards 03.01(1990).

138. ASTM E92, Standard Test Method for Vickers Hardness of Metallic Materials, ASTM International, 82 (2003).

139. Y. Chen, Y. Wang and J. Gianetto, Proceedings of the 18th International Offshore and Polar Engineering Conference, Vancouver, Canada, July 6–11, (2008).

140. S. R. Lampman, Weld Integrity and Performance, ASM International Technology& Engineering, (1997).

141. M. Dunder, T. Vuherer and I. Kladaric,*Weldability Investigation of TStE 420 After Weld Thermal Cycle Simulation*, **52 (2)**, 97–104 (2010).

142. J. Gorka, An Influence of Welding Thermal Cycles on Properties and HAZ Structure of S700MC Steel Treated Using Thermomechanical Method, PhD Thesis, Silesian University of Technology, Poland, (2011).

143. E. N. Akhusama, Microstructural Evolution and Fatigue Crack Growth Characteristics Through the HAZ of Welded AA 6061, MSc Thesis, University of Nairobi, (2012).

144. D. Zervaki and G. N. Haidemennopoulos, *Computational Kinetics Simulation of the Dissolution and Coarsening in the HAZ during Laser Welding of AA 6061-T6*, Welding Journal, **86**, 211-221 (2007).

145. C. Rajendran, K. Srinivasan, Y. Balasubramanian, H. Balaji and P. Selvaraj, *Influences of Post Weld Heat Treatment on Tensile Strength and Microstructure Characteristics of Friction Stir Welded Butt Joints of AA 2014-T6 Aluminium Alloy*. Journal of the Mechanical Behavior of Materials, **25 (3)**, 89-98 (2016).

146. E. Raouache, Z. Boumerzoug, F. Delaunois and F. Khalfallah, *Investigation by Thermal Cycle Simulation of Heat Affected Zone in Welded AA 2014 Aluminium Alloy*, Res Dev Material Sci, **13 (3)**, 1407-1411 (2020).

147. P.H. Chong, Z. Liu, P. Skeldon and G.E. Thompson, *Large Area Laser Surface Treatment of Aluminium Alloys for Pitting Corrosion Protection*, Applied Surface Science, **208–209**, 399-404 (2003).

148. G. İpekoğlu, S. Erim, B. Goren-Kıral and G. Çam, *Investigation into the Effect of Temper Condition on Friction Stir Weldability of AA6061*, Al-alloy plates, Kovove Materialy, **51**, 155–163 (2013).

149. G. İpekoğlu, S. Erim, G. Çam, *Effects of Temper Condition and Post Weld Heat Treatment on the Microstructure and Mechanical Properties of Friction Stir Butt-Welded AA7075 Al Alloy Plates*, The International Journal of Advanced Manufacturing Technology **70**, 201–213 (2014)

150. Nadish, S. Keshavan, A. Chandrasekhar, B. S. Kumar and M. Chowdegowda, *Metal Inert Gas Welding Behaviour in Al-Zn Based Alloy 7075*, International Journal of Engineering and Manufacturing Science, **2**, 23-30 (2012).

151. B. B. Verma, J. D. Atkinson and M. Kumar, *Study of Fatigue Behaviour of 7475 Aluminium Alloy*, Bulletin of Material Science, **24 (2)**, 231-236 (2001).

152. C. Rajendran, K. Srinivasan, Y. Balasubramanian, H. Balaji and P. Selvaraj, *Influences of Post Weld Heat Treatment on Tensile Strength and Microstructure Characteristics of Friction Stir Welded Butt Joints of AA 2014-T6 Aluminium Alloy*. Journal of the Mechanical Behavior of Materials, **25 (3)**, 89-98 (2016).

153. L. James, *The Effect of Grain Size upon the Fatigue-Crack Propagation Behavior of Alloy 718Under Hold-Time Cycling at Elevated Temperature*, **25**, 305-314 (1986).

154. S. Taira, K. Tanaka and M. Hoshina, *Grain Size Effect on Crack Nucleation and Growth in Long Life Fatigue of Low-Carbon Steel*, Fatigue Mechanisms. ASTM International, 135-173 (1979).

155. Y. Nakai, K. Tanaka and T. Nakanishi, *The Effects of Stress Ratio and Grain Size on Nearthreshold Fatigue Crack Propagation in Low-Carbon Steel*, Engineering Fracture Mechanics, **15 (3-4)**, 291-302 (1981).

156. B. Parida, M. Mohapatra, P. Biswas and N. Mandal, *Study of Mechanical and Microstructural Properties of Friction Stir Welded Al Alloy*, International Journal of Engineering Technology and Advanced Technology, **2 (10)**, 2250-2459 (2012).

157. G. Cam, V. Ventzke, J. F. Santes, M. Kocak, G. Jennequin and P. G. Maurin, *Characterization of Electron Beam Welded Aluminium Alloys*, Science and Technology of Welding and Joining, **4 (5)**, 317 – 323 (1999).

158. D. Taylor and J. F. Knott, *Fatigue Crack Propagation Behaviour of Short Cracks; the effect of microstructure*, Fatigue Eng. Mater. Struct. **4**, 147-155 (1981).

159. C. W. Brown, J. E. King and M. A. Hicks, *Effects of Microstructure on Long and Short Crack Growth in Ni-base Superalloy*, Met. Sci. **18**, 374-380 (1984).

160. J. Lankford, *The Growth of Small Fatigue Cracks in 7075-T6 Aluminium*, Fatigue Engng Mater. Struct. **5**, 233-248 (1982).

161. P. M. Mulvihill and C. J. Beevers, *The Initiation and Growth of Inter-Granularly Initiated Short Fatigue Cracks in an Aluminium 4.5 percent Copper Alloy*, Mech. Engng Publ, London, **1**, 203-213 (1986).

162. J. Lankford, *The Influence of Microstructure on the Growth of Small Fatigue Cracks*, Fatigue Fract. Engng Mater. Struct. **8**, 161-175 (1985).

163. J. Masounave and J. P. Bailon, *Effect of Grain Size on the Threshold Stress Intensity Factor in Fatigue of a Ferritic Steel*, Scripta Met. **10**, 165-170 (1976).

164. E. K. Priddle, *The Influence of Grain Size on Threshold Stress Intensity for Fatigue Crack Growth in AISI 316 Stainless Steel*, Scripta Met. **12**, 49-56 (1978).

165. G. Oates and D. V. Wilson, *The Effects of Dislocation Locking and Strain Ageing on the Fatigue Limit of Low Carbon Steel*. Acta Met. **12**, 21-33 (1964).

166. M. Klesnil, M. Holzman, P. Lukas and P. Rys, *Some Aspects of the Fatigue Process in Low Carbon Steel.* J. Zron Steel Znst, **203**, 41-53 (1965).

167. M. Kage, K. J. Miller and R. A. Smith, *Fatigue Crack Initiation and Propagation in a Low Carbon Steel of two Different Grain Sizes*, Fatigue and Fracture of Engineering Materials and Structures. **15,** 763-774 (1992).

168. L. Zhang, X. Liu, L. Wang, P. Wang and H. Fang, *Fatigue Crack Initiation for Al-Zn-Mg Alloy Welded Joint*, Acta Metallurgica, **25 (3)**, 235-240 (2012).

169. G. M. Dominguez, J. C. Juarez, R.G. Bernal, J. L. Ambriz and E. C. Gomez, *Fatigue Endurance of Welded (GMAW-MIG) Aluminium Alloy 6061-T6*, Int. J. of Emerging Technology and Advanced Engineering, **4,** 583-593 (2014).

170. D. Michael, *The Physics of Fatigue Crack Initiation*, International journal of fatigue, **57**, 58-72 (2013).

171. D. Hoeppner, *The Effect of Grain Size on Fatigue Crack Propagation in Copper*, AM. SOC. Testing Mats, **415**, 486-504 (1967).

172. D. J. Morrison and J. C. Moosbrugger, *Effects of Grain Size on Cyclic Plasticity and Fatigue Crack Initiation in Nickel*, International Journal of Fatigue, vol. **19 (93)**, 51-59 (1997).

173. A. W. Thompson and W.A. Backofen, *The Effect of Grain Size on Fatigue*, Acta Metall, **19**, 597-606(1971).

174. F. Liang and C. Laird, *Control of Intergranular Fatigue Cracking by Slip Homogeneity in Copper, Effect of Grain Size*, Materials Science and Engineering A, **117**, 95-102 (1989).

175. D. Michael, J. H. Maier, and H. Sehitoglu, *The Role of Grain Boundaries on Fatigue Crack Initiation–an Energy Approach*, International Journal of Plasticity, **27 (5)**, 801-821 (2011).

176. W. Z. Abuzaid, M. Sangid, J. Carrol, H. Sehitoglu and J. Lambros, *Slip Transfer and Plastic Strain Accumulation Across Grain Boundaries in Hastelloy X*, Journal of the Mechanics and Physics of Solids **60 (6)**, 1201-1220 (2012).

177. D. Michael, G. Pataky, H. Sehitoglu, R. Rateick, T. Niendorf, and H. Maier, *Superior Fatigue Crack Growth Resistance, Irreversibility, and Fatigue Crack Crowth–Microstructure Relationship of Nanocrystalline Alloys*, Acta Materialia, **59 (19)**, 7340-7355 (2011).

178. T. Hanlon, Y. N. Kwon, and S. Suresh, *Grain Size Effects on the Fatigue Response of Nanocrystalline Metals*, Scripta Materialia, **49 (7)**, 675-680 (2003).

179. L. Wagner, and J. K. Gregory, *Improvement of the Fatigue Life of Titanium Alloys*, Advanced Materials and Processes, **146 (1)**, 50 (1994).

180. A. Mohamed, Y. Madhoun and M. N. Bassim, *The Effect of Grain Size on Low-Cycle Fatigue Behavior of Al-2024 Polycrystalline Alloy*, Metallurgical and Materials Transactions A, **35 (9)**, 2725–2728 (2004).

181. R. Ebara, *Grain Size Effect on Low Cycle Fatigue Behavior of High Strength Structural Materials*, Solid State Phenomena, **258**, 269–272 (2016).

182. P. Cavaliere, *Study of Fatigue Resistance Properties of a Zirconium Modified 2014 Aluminium Alloy*, Metallic Material with High Structural Efficiency, 179–188 (2004).

183. L. Llanes, A. D. Rollett, and C Laird, *Effect of Ramp-Treatment on the Cyclic Stress-Strain Curve of Small Grained Copper*, Materials Science and Engineering A, **167 (1-2)**, 37–45 (1993).

184. H. Mughrabi, R. Wang, N. Hansen, A. Horsewell, T. Leffers, and H. Lilholt, Deformation of Polycrystals, Mechanisms and Microstructures, Proceedings of Risø 2nd

International Symposium on Metallurgy and Materials, September 14-18, Roskilde, (1981).

APPENDICES

Appendix A: Tensile test data for the BM of AA 2014

Tensile test data for the BM of AA 2014 (First Test)

Force (N)	ΔL (m)	Breadth (m)	Width (m)	Area (m^2)	Original L (m)	Stress (MPa)	Strain
0	-	6.51E-03	2.60E-03	1.69E-05	0.025	0	-
250	1.43E-05	6.51E-03	2.60E-03	1.69E-05	0.025	14.770	5.73E-04
500	2.86E-05	6.51E-03	2.60E-03	1.69E-05	0.025	29.540	1.15E-03
750	6.45E-05	6.51E-03	2.60E-03	1.69E-05	0.025	44.311	2.58E-03
1000	8.59E-05	6.51E-03	2.60E-03	1.69E-05	0.025	59.081	3.44E-03
1250	1.19E-04	6.51E-03	2.60E-03	1.69E-05	0.025	73.851	4.77E-03
1500	1.43E-04	6.51E-03	2.60E-03	1.69E-05	0.025	88.621	5.73E-03
1750	1.75E-04	6.51E-03	2.60E-03	1.69E-05	0.025	103.391	7.02E-03
2000	2.01E-04	6.51E-03	2.60E-03	1.69E-05	0.025	118.161	8.02E-03
2250	2.32E-04	6.51E-03	2.60E-03	1.69E-05	0.025	132.932	9.28E-03
2500	2.58E-04	6.51E-03	2.60E-03	1.69E-05	0.025	147.702	1.03E-02
2750	2.89E-04	6.51E-03	2.60E-03	1.69E-05	0.025	162.472	1.16E-02
3000	3.15E-04	6.51E-03	2.60E-03	1.69E-05	0.025	177.242	1.26E-02
3250	3.46E-04	6.51E-03	2.60E-03	1.69E-05	0.025	192.012	1.38E-02
3500	3.72E-04	6.51E-03	2.60E-03	1.69E-05	0.025	206.782	1.49E-02
3750	4.03E-04	6.51E-03	2.60E-03	1.69E-05	0.025	221.553	1.61E-02
4000	4.30E-04	6.51E-03	2.60E-03	1.69E-05	0.025	236.323	1.72E-02
4250	4.60E-04	6.51E-03	2.60E-03	1.69E-05	0.025	251.093	1.84E-02
4500	4.87E-04	6.51E-03	2.60E-03	1.69E-05	0.025	265.863	1.95E-02
4750	5.17E-04	6.51E-03	2.60E-03	1.69E-05	0.025	280.633	2.07E-02
5000	5.44E-04	6.51E-03	2.60E-03	1.69E-05	0.025	295.404	2.18E-02
5250	5.74E-04	6.51E-03	2.60E-03	1.69E-05	0.025	310.174	2.30E-02
5500	6.02E-04	6.51E-03	2.60E-03	1.69E-05	0.025	324.944	2.41E-02
5750	6.31E-04	6.51E-03	2.60E-03	1.69E-05	0.025	339.714	2.53E-02
6000	6.59E-04	6.51E-03	2.60E-03	1.69E-05	0.025	354.484	2.64E-02
6250	7.16E-04	6.51E-03	2.60E-03	1.69E-05	0.025	369.254	2.86E-02
6500	7.45E-04	6.51E-03	2.60E-03	1.69E-05	0.025	384.025	2.98E-02
7000	8.31E-04	6.51E-03	2.60E-03	1.69E-05	0.025	413.565	3.32E-02
7500	1.23E-03	6.51E-03	2.60E-03	1.69E-05	0.025	443.105	4.93E-02
7825	1.83E-03	6.51E-03	2.60E-03	1.69E-05	0.025	462.307	7.33E-02
7625	2.12E-03	6.51E-03	2.60E-03	1.69E-05	0.025	450.490	8.48E-02

Tensile test data for the BM of AA 2014 (Second Test)

Force (N)	ΔL (m)	Breadth (m)	Width (m)	Area (m^2)	Original L (m)	Stress (MPa)	Strain
0	-	6.49E-03	2.60E-03	1.69E-05	0.025	0	-
250	4.29E-05	6.49E-03	2.60E-03	1.69E-05	0.025	14.816	1.72E-03
500	8.58E-05	6.49E-03	2.60E-03	1.69E-05	0.025	29.631	3.43E-03
570	8.15E-05	6.49E-03	2.60E-03	1.69E-05	0.025	33.780	3.26E-03
1000	1.43E-04	6.49E-03	2.60E-03	1.69E-05	0.025	59.263	5.72E-03
1250	1.67E-04	6.49E-03	2.60E-03	1.69E-05	0.025	74.078	6.68E-03
1500	2.00E-04	6.49E-03	2.60E-03	1.69E-05	0.025	88.894	8.01E-03
1750	2.25E-04	6.49E-03	2.60E-03	1.69E-05	0.025	103.710	9.01E-03
2000	2.57E-04	6.49E-03	2.60E-03	1.69E-05	0.025	118.526	1.03E-02
2250	2.83E-04	6.49E-03	2.60E-03	1.69E-05	0.025	133.341	1.13E-02
2500	3.15E-04	6.49E-03	2.60E-03	1.69E-05	0.025	148.157	1.26E-02
2750	3.41E-04	6.49E-03	2.60E-03	1.69E-05	0.025	162.973	1.36E-02
3000	3.72E-04	6.49E-03	2.60E-03	1.69E-05	0.025	177.788	1.49E-02
3250	4.12E-04	6.49E-03	2.60E-03	1.69E-05	0.025	192.604	1.65E-02
3500	4.43E-04	6.49E-03	2.60E-03	1.69E-05	0.025	207.420	1.77E-02
3750	4.56E-04	6.49E-03	2.60E-03	1.69E-05	0.025	222.235	1.82E-02
4000	4.86E-04	6.49E-03	2.60E-03	1.69E-05	0.025	237.051	1.95E-02
4250	5.13E-04	6.49E-03	2.60E-03	1.69E-05	0.025	251.867	2.05E-02
4500	5.44E-04	6.49E-03	2.60E-03	1.69E-05	0.025	266.682	2.17E-02
4750	5.84E-04	6.49E-03	2.60E-03	1.69E-05	0.025	281.498	2.34E-02
5000	6.15E-04	6.49E-03	2.60E-03	1.69E-05	0.025	296.314	2.46E-02
5250	6.55E-04	6.49E-03	2.60E-03	1.69E-05	0.025	311.130	2.62E-02
5500	6.87E-04	6.49E-03	2.60E-03	1.69E-05	0.025	325.945	2.75E-02
5750	7.13E-04	6.49E-03	2.60E-03	1.69E-05	0.025	340.761	2.85E-02
6000	7.44E-04	6.49E-03	2.60E-03	1.69E-05	0.025	355.577	2.98E-02
6500	9.16E-04	6.49E-03	2.60E-03	1.69E-05	0.025	385.208	3.66E-02
7000	1.43E-03	6.49E-03	2.60E-03	1.69E-05	0.025	414.839	5.72E-02
7100	1.77E-03	6.49E-03	2.60E-03	1.69E-05	0.025	420.766	7.10E-02
7000	1.95E-03	6.49E-03	2.60E-03	1.69E-05	0.025	414.839	7.78E-02
6625	2.06E-03	6.49E-03	2.60E-03	1.69E-05	0.025	392.616	8.24E-02

Tensile test data for the BM of AA 2014 (Third Test)

Force (N)	ΔL (m)	Breadth (m)	Width (m)	Area (m^2)	Original L (m)	Stress (Mpa)	Strain
0	-	6.51E-03	2.60E-03	1.69E-05	0.025	0	-
250	3.06E-05	6.51E-03	2.60E-03	1.69E-05	0.025	14.770	1.22E-03
500	6.12E-05	6.51E-03	2.60E-03	1.69E-05	0.025	29.540	2.45E-03
750	9.18E-05	6.51E-03	2.60E-03	1.69E-05	0.025	44.311	3.67E-03
1000	1.22E-04	6.51E-03	2.60E-03	1.69E-05	0.025	59.081	4.90E-03
1250	1.53E-04	6.51E-03	2.60E-03	1.69E-05	0.025	73.851	6.12E-03
1500	1.84E-04	6.51E-03	2.60E-03	1.69E-05	0.025	88.621	7.35E-03
1750	2.14E-04	6.51E-03	2.60E-03	1.69E-05	0.025	103.391	8.57E-03
2000	2.45E-04	6.51E-03	2.60E-03	1.69E-05	0.025	118.161	9.80E-03
2250	2.75E-04	6.51E-03	2.60E-03	1.69E-05	0.025	132.932	1.10E-02
2500	3.06E-04	6.51E-03	2.60E-03	1.69E-05	0.025	147.702	1.22E-02
2750	3.37E-04	6.51E-03	2.60E-03	1.69E-05	0.025	162.472	1.35E-02
3000	3.67E-04	6.51E-03	2.60E-03	1.69E-05	0.025	177.242	1.47E-02
3250	4.12E-04	6.51E-03	2.60E-03	1.69E-05	0.025	192.012	1.65E-02
3500	4.44E-04	6.51E-03	2.60E-03	1.69E-05	0.025	206.782	1.78E-02
3750	4.88E-04	6.51E-03	2.60E-03	1.69E-05	0.025	221.553	1.95E-02
4000	5.20E-04	6.51E-03	2.60E-03	1.69E-05	0.025	236.323	2.08E-02
4250	5.35E-04	6.51E-03	2.60E-03	1.69E-05	0.025	251.093	2.14E-02
4500	5.66E-04	6.51E-03	2.60E-03	1.69E-05	0.025	265.863	2.27E-02
4750	6.25E-04	6.51E-03	2.60E-03	1.69E-05	0.025	280.633	2.50E-02
5000	6.58E-04	6.51E-03	2.60E-03	1.69E-05	0.025	295.404	2.63E-02
5250	7.01E-04	6.51E-03	2.60E-03	1.69E-05	0.025	310.174	2.80E-02
5500	7.35E-04	6.51E-03	2.60E-03	1.69E-05	0.025	324.944	2.94E-02
6000	8.42E-04	6.51E-03	2.60E-03	1.69E-05	0.025	354.484	3.37E-02
6400	9.18E-04	6.51E-03	2.60E-03	1.69E-05	0.025	378.117	3.67E-02
6500	9.80E-04	6.51E-03	2.60E-03	1.69E-05	0.025	384.025	3.92E-02
7000	1.07E-03	6.51E-03	2.60E-03	1.69E-05	0.025	413.565	4.29E-02
7100	1.50E-03	6.51E-03	2.60E-03	1.69E-05	0.025	419.473	6.00E-02
7700	2.05E-03	6.51E-03	2.60E-03	1.69E-05	0.025	454.921	8.20E-02
7600	2.42E-03	6.51E-03	2.60E-03	1.69E-05	0.025	449.013	9.67E-02

Appendix B: Thermal cycle simulation data for the two regions of HAZ of specimen AA 2014.

	HCF Specimens		LCF Specimens		FGC Specimens	
Time (Sec)	Region C 590°C	Region D 650°C	Region C 590°C	Region D 650°C	Region C 590°C	Region D 650°C
0	30.2	29.7	31.2	32.1	30.7	31.6
2	91.4	120	120.2	170	98.4	115
4	193.7	270	156.1	214.7	169.6	259.6
6	282.9	314.1	228.9	258.7	251.3	305
8	321.7	348.6	266.4	339.5	301.4	330.4
10	354.5	415.1	335.2	376.5	336	368.6
12	378.3	446.2	367.6	439.5	369.4	399.9
14	411.7	502.9	425.9	465.1	397.2	429.4
16	439.1	527.4	474.3	509.8	430.7	476.8
18	468.4	571.9	494.6	543.8	480.4	511.2
20	501.9	590.8	529.8	581.9	518	549.9
22	529.1	622.1	544.1	609.7	541.2	591.3
24	558.9	639.2	567.7	628.8	561.1	610
26	579.8	652.1	578.3	651.7	579.9	634.1
28	593.2	633.3	594.8	641.4	586.6	648.3
30	560.4	606.3	577.5	622.9	592.1	645.3
32	529.8	555.7	502.1	584.6	569.3	629.7
34	481.2	533.3	471.8	541.7	531.5	610.2
36	457.2	490.3	423.8	496.5	478	577.8
38	429.7	471.9	404.4	457.9	439.6	519.7
40	415	436.9	328.3	383.1	419.7	479.5
42	389.6	422	310.3	339	398.3	440.4
44	376.2	393.6	288.9	314.2	365.1	416.2
46	350.5	380.4	279.3	303.8	342.7	386.2
48	334.1	357.1	262.3	284.4	326.4	366.5
50	318.3	335.2	250.7	267.7	301.7	348.8
52	301.1	324.9	240.3	260	287.3	323.4
54	289.8	305.4	234.5	247.3	271.6	308.1
56	279.6	296.9	223.1	241.7	253.1	287.6
58	265.3	279.1	212	230.6	239.8	272.2
60	250.1	271.3	207.4	226	230.1	261.1
62	242.2	256.6	197.7	217.8	219.8	249.9
64	232.1	249.5	193.4	212.5	210.3	237.9
66	220	236.4	185.5	201.8	200.1	226.3
68	209.7	230.5	181.6	197.1	193.7	216.5
70	203.1	220	174.7	185.3	185.2	207.5

72	195.4	215	171.5	182.1	181.3	199.1
74	189.6	205.6	165.8	177.3	175.9	191.7
76	184.9	201.2	163	175.8	173.2	187.4
78	180.3	192.8	158	172.6	166.8	182.5
80	172.4	188.6	155.6	170.6	163.3	178.1
82	169.8	180.8	150.4	166.4	158.1	171.2
84	166.5	177.5	148.3	163.6	155.1	166.1
86	161.2	171.2	144.1	159.6	152.8	162.7
88	158.7	168.3	141.3	157.3	148.3	157.3
90	152.6	162.6	136.3	153.5	143.9	154.2
92	149.3	157.3	134.3	149.8	141.3	150.9
94	146.1	154.6	128.3	148.7	138.1	148.1
96	141.8	149.9	126.8	145.8	134.2	146.1
98	137.8	147.5	123.5	144.4	129.6	143.3
100	133.9	143	120.9	141.8	126.7	140.8
102	129.6	140.6	119.4	140.6	122.8	136.2
104	125.1	136.5	118.4	137.1	119.9	132.7
106	120.9	134.2	117.7	135.5	118.1	128.9
108	119.1	130.3	114.7	133	115.7	126.9
110	116.7	128.5	112.9	131.8	115.2	125.3
112	113.3	124.7	109.1	129	113.2	124
114	112.1	122.7	106.7	129	110.8	122.2
116	110.4	119	103.9	127.5	109.1	119.1
118	108.1	116.8	102.4	127.5	107.3	117.2
120	107.3	111.8	99.2	126.7	106.2	115.3
122	105.4	110.7	97.6	126.7	102.9	113.2
124	102.8	107.8	94.8	125.9	101.8	111.8
126	100.1	106.2	93.8	125.3	99.2	110.2
128	98.3	103.6	91.1	124.6	98	108.3
130	94.8	102.3	90	123	95.8	105.9

Appendix C: Fatigue strength data for the BM and two regions of the HAZ of AA 2014.

BM/As-received					
Specimen	1	2	3	4	5
Diameter (m)	0.00406	0.00398	0.00396	0.00398	0.00395
Force (N)	35	23	25	27.5	26.5
Stress (MPa)	179	104	116	124	123
Cycles to failure ($\times 10^7$)	0.083	2.07 Didn't fail	1.24	0.918	0.997
Approximate Fatigue Strength (MPa)	123				

HAZ Region C (590°C)				
Specimen	1	2	3	4
Diameter (m)	0.00402	0.00397	0.00401	0.00396
Force (N)	26	17	19	18
Stress (MPa)	118	80	85	84
Cycles to failure ($\times 10^7$)	0.0876	1.19	0.902	1.01

Approximate Fatigue Strength (MPa)	84				
HAZ Region D (650°C)					
Specimen	1	2	3	4	5
Diameter (m)	0.00401	0.00396	0.00397	0.00401	0.00396
Force (N)	24	17.8	19	21	20
Stress (MPa)	108	82	87	93	92
Cycles to failure ($\times 10^7$)	0.147	1.673 Didn't fail	1.18	0.937	0.9992
Approximate Fatigue Strength (MPa)	92				

Appendix D: Low cycle fatigue data for the BM and two regions of the HAZ of AA 2014.

	Specimen	1	2	3	4
	L (m)	0.039	0.039	0.039	0.039
	δ (mm)	3.394	3.088	2.423	2.242
	Frequency (Hz)	4.3	4.3	4.3	4.3
	Total Strain Amplitude ($\Delta\varepsilon_t$)	0.08703	0.07918	0.06213	0.05749
BM (As-received)	No. of Cycles to failure (N_f)	81429	202874	488597	593496
Region C 590°C	No. of Cycles to failure (N_f)	38553	89391	281736	321906
Region D 650°C	No. of Cycles to failure (N_f)	47623	121492	312419	382563

Appendix E: Fatigue Crack Growth Data for the BM and two regions the HAZ of AA 2014

K-decreasing test data for the BM

Δ P (N)	N (cycles)	2a (mm)	Δ 2a (mm)	a (mm)	Δa (mm)	Δ N	da/dN (mm/cycle)	ΔK ($MNm^{-3/2}$)
1771.1	0	40.6	-	20.3	-	-	-	-
1771.1	86135	42.7	2.1	21.35	1.05	86135	1.22E-05	1.764
1771.1	149200.8	45.5	2.8	22.75	1.4	63065.8	2.22E-05	1.821
1771.1	217959	47.8	2.3	23.9	1.15	68758.2	1.67E-05	1.867
1597.6	307988.8	49.1	1.3	24.55	0.65	90029.8	7.22E-06	1.706
1597.6	413148.4	51	1.9	25.5	0.95	105159.6	9.03E-06	1.739
1597.6	506324	52.4	1.4	26.2	0.7	93175.6	7.51E-06	1.763
1437.4	612532.2	53.6	1.2	26.8	0.6	106208.2	5.65E-06	1.604
1437.4	713197.8	55	1.4	27.5	0.7	100665.6	6.95E-06	1.625
1437.4	818207.6	56.3	1.3	28.15	0.65	105009.8	6.19E-06	1.644
1295.0	927711.4	57.2	0.9	28.6	0.45	109503.8	4.11E-06	1.493
1295.0	1042009	58.3	1.1	29.15	0.55	114297.4	4.81E-06	1.507
1295.0	1162148	59.3	1	29.65	0.5	120139.6	4.16E-06	1.520
1165.9	1287681	60	0.7	30	0.35	125532.4	2.79E-06	1.377
1165.9	1413213	60.8	0.8	30.4	0.4	125532.4	3.19E-06	1.386
1165.9	1519272	61.5	0.7	30.75	0.35	106058.4	3.30E-06	1.394
1050.2	1664727	62.1	0.6	31.05	0.3	145455.8	2.06E-06	1.262
1050.2	1811831	62.6	0.5	31.3	0.25	147103.6	1.70E-06	1.267
1050.2	1972417	63.2	0.6	31.6	0.3	160585.6	1.87E-06	1.273
947.9	2129107	63.6	0.4	31.8	0.2	156690.8	1.28E-06	1.152
947.9	2305572	64.1	0.5	32.05	0.25	176464.4	1.42E-06	1.157
947.9	2477542	64.5	0.4	32.25	0.2	171970.4	1.16E-06	1.160
854.4	2651460	64.8	0.3	32.4	0.15	173917.8	8.62E-07	1.049
854.4	2841856	65.1	0.3	32.55	0.15	190395.8	7.88E-07	1.051
854.4	3011280	65.3	0.2	32.65	0.1	169423.8	5.90E-07	1.053
769.9	4028721	65.4	0.1	32.7	0.05	1017441.6	4.91E-08	0.949

K-decreasing test data for the region C of the HAZ.

Δ P (N)	N (cycles)	2a	Δ 2a (mm)	a (mm)	Δa (mm)	Δ N (cycles)	da/dN (mm/cycle)	ΔK ($MNm^{-3/2}$)
1624.25	0	40.2	-	20.1	-	-	-	-
1624.25	85685.6	42.3	2.1	21.15	1.05	85685.6	1.23E-05	1.610
1624.25	149800	45.1	2.8	22.55	1.4	64114.4	2.18E-05	1.663
1624.25	194889.8	47.7	2.6	23.85	1.3	45089.8	2.88E-05	1.710
1464.05	269340.4	49.6	1.9	24.8	0.95	74450.6	1.28E-05	1.572
1464.05	367010	51.7	2.1	25.85	1.05	97669.6	1.08E-05	1.605
1464.05	460635	54.5	2.8	27.25	1.4	93625	1.50E-05	1.648
1321.65	571337.2	56.5	2	28.25	1	110702.2	9.03E-06	1.514
1321.65	657022.8	58.3	1.8	29.15	0.9	85685.6	1.05E-05	1.538
1321.65	761583.2	60.3	2	30.15	1	104560.4	9.56E-06	1.565
1188.15	874382.6	61.7	1.4	30.85	0.7	112799.4	6.21E-06	1.423
1188.15	988380.4	63.3	1.6	31.65	0.8	113997.8	7.02E-06	1.441
1188.15	1101629	65.1	1.8	32.55	0.9	113248.8	7.95E-06	1.461
1072.45	1226712	66.3	1.2	33.15	0.6	125083	4.80E-06	1.331
1072.45	1347751	67.3	1	33.65	0.5	121038.4	4.13E-06	1.341
1072.45	1453809	68.5	1.2	34.25	0.6	106058.4	5.66E-06	1.353
965.65	1599265	69.4	0.9	34.7	0.45	145455.8	3.09E-06	1.226
965.65	1746368	70.4	1	35.2	0.5	147103.6	3.40E-06	1.235
965.65	1847034	71.2	0.8	35.6	0.4	100665.6	3.97E-06	1.242
867.75	2003275	71.8	0.6	35.9	0.3	156241.4	1.92E-06	1.121
867.75	2149780	72.4	0.6	36.2	0.3	146504.4	2.05E-06	1.126
867.75	2299280	73.1	0.7	36.55	0.35	149500.4	2.34E-06	1.131
783.2	2473198	73.6	0.5	36.8	0.25	173917.8	1.44E-06	1.024
783.2	2634682	74	0.4	37	0.2	161484.4	1.24E-06	1.027
783.2	2818487	74.4	0.4	37.2	0.2	183804.6	1.09E-06	1.030
707.55	3872330	74.5	0.1	37.25	0.05	1053843	4.74E-08	0.931

K-decreasing test data for the region D of the HAZ.

Δ P (N)	N (cycles)	2a	Δ 2a (mm)	a (mm)	Δa (mm)	Δ N (cycles)	da/dN (mm/cycle)	ΔK ($MNm^{-3/2}$)
1668.75	0	40	-	20	-	-	-	-
1668.75	87333.4	42.4	2.4	21.2	1.2	87333.4	1.37E-05	1.656
1668.75	149650.2	44.7	2.3	22.35	1.15	62316.8	1.85E-05	1.701
1668.75	193841.2	47.2	2.5	23.6	1.25	44191	2.83E-05	1.748
1504.1	268891	49	1.8	24.5	0.9	75049.8	1.20E-05	1.605
1504.1	365811.6	51.1	2.1	25.55	1.05	96920.6	1.08E-05	1.639
1504.1	444606.4	53.1	2	26.55	1	78794.8	1.27E-05	1.671
1352.8	570588.2	55.3	2.2	27.65	1.1	125981.8	8.73E-06	1.534
1352.8	661067.4	57.1	1.8	28.55	0.9	90479.2	9.95E-06	1.558
1352.8	750348.2	58.6	1.5	29.3	0.75	89280.8	8.40E-06	1.579
1219.3	863447.2	60.2	1.6	30.1	0.8	113099	7.07E-06	1.442
1219.3	977145.4	61.6	1.4	30.8	0.7	113698.2	6.16E-06	1.459
1219.3	1090544	63.3	1.7	31.65	0.85	113398.6	7.50E-06	1.479
1099.15	1215777	64.5	1.2	32.25	0.6	125232.8	4.79E-06	1.346
1099.15	1347451	65.6	1.1	32.8	0.55	131674.2	4.18E-06	1.357
1099.15	1467291	66.9	1.3	33.45	0.65	119840	5.42E-06	1.371
987.9	1603160	67.7	0.8	33.85	0.4	135868.6	2.94E-06	1.239
987.9	1738429	68.4	0.7	34.2	0.35	135269.4	2.59E-06	1.246
987.9	1854374	69.2	0.8	34.6	0.4	115945.2	3.45E-06	1.253
890	2046268	70	0.8	35	0.4	191893.8	2.08E-06	1.135
890	2192473	70.6	0.6	35.3	0.3	146204.8	2.05E-06	1.140
890	2352009.8	71.2	0.6	35.6	0.3	159537	1.88E-06	1.145
805.45	2527575.4	71.5	0.3	35.75	0.15	175565.6	8.54E-07	1.038
805.45	2717671.6	71.9	0.4	35.95	0.2	190096.2	1.05E-06	1.041
805.45	2890840.4	72.3	0.4	36.15	0.2	173168.8	1.15E-06	1.044
725.35	3887160.2	72.3	0.1	36.15	0.05	996319.8	1.00E-07	0.940

Constant amplitude test data for the BM

Δ P (N)	N (cycles)	2a (mm)	Δ 2a (mm)	a (mm)	Δa (mm)	Δ N (cycles)	da/dN (mm/cycle)	ΔK ($MNm^{-3/2}$)
1268.25	0	39.8	-	19.9	-	-	-	-
1268.25	431723.6	42.1	2.3	21.05	1.15	431723.6	2.66E-06	1.255
1268.25	654626	42.6	0.5	21.3	0.25	222902.4	1.12E-06	1.262
1268.25	848017.8	43.2	0.6	21.6	0.3	193391.8	1.55E-06	1.271
1268.25	1010850	43.9	0.7	21.95	0.35	162832.6	2.15E-06	1.281
1268.25	1142525	44.7	0.8	22.35	0.4	131674.2	3.04E-06	1.293
1268.25	1265061	45.6	0.9	22.8	0.45	122536.4	3.67E-06	1.306
1268.25	1372617	46.6	1	23.3	0.5	107556.4	4.65E-06	1.320
1268.25	1471635	47.8	1.2	23.9	0.6	99017.8	6.06E-06	1.337
1268.25	1561815	48.7	0.9	24.35	0.45	90179.6	4.99E-06	1.349
1268.25	1648998	49.7	1	24.85	0.5	87183.6	5.74E-06	1.363
1268.25	1739028	50.9	1.2	25.45	0.6	90029.8	6.66E-06	1.379
1268.25	1836997	52.4	1.5	26.2	0.75	97969.2	7.66E-06	1.399
1268.25	1921784	53.9	1.5	26.95	0.75	84786.8	8.85E-06	1.419
1268.25	2005672	55.3	1.4	27.65	0.7	83888	8.34E-06	1.438
1268.25	2068438	56.6	1.3	28.3	0.65	62766.2	1.04E-05	1.454
1268.25	2114577	57.8	1.2	28.9	0.6	46138.4	1.30E-05	1.470
1268.25	2176145	59	1.2	29.5	0.6	61567.8	9.75E-06	1.485
1268.25	2231571	60.3	1.3	30.15	0.65	55426	1.17E-05	1.501
1268.25	2272316	61.5	1.2	30.75	0.6	40745.6	1.47E-05	1.516
1268.25	2309766	62.8	1.3	31.4	0.65	37450	1.74E-05	1.532
1268.25	2343921	64.2	1.4	32.1	0.7	34154.4	2.05E-05	1.549
1268.25	2391407	66	1.8	33	0.9	47486.6	1.90E-05	1.571
1268.25	2424363	67.6	1.6	33.8	0.8	32956	2.43E-05	1.590
1268.25	2449979	69.1	1.5	34.55	0.75	25615.8	2.93E-05	1.607
1268.25	2469902	70.5	1.4	35.25	0.7	19923.4	3.51E-05	1.623
1268.25	2485032	71.4	0.9	35.7	0.45	15129.8	2.97E-05	1.634
1268.25	2519336	73.8	2.4	36.9	1.2	34304.2	3.50E-05	1.661
1268.25	2538810	76	2.2	38	1.1	19474	5.65E-05	1.685
1268.25	2568321	78.7	2.7	39.35	1.35	29510.6	4.57E-05	1.715
1268.25	2582402	81.7	3	40.85	1.5	14081.2	1.07E-04	1.747
1268.25	2591840	85.3	3.6	42.65	1.8	9437.4	1.91E-04	1.786
1268.25	2595285	88.3	3	44.15	1.5	3445.4	4.35E-04	1.817

Constant amplitude test data for the Region C

Δ P (N)	N (cycles)	2a (mm)	Δ 2a (mm)	a (mm)	Δa (mm)	Δ N (cycles)	da/dN (mm/cycle)	ΔK ($MNm^{-3/2}$)
1268.25	0	40.2	-	20.1	-	-	-	-
1268.25	359220.4	42.4	2.2	21.2	1.1	359220.4	3.06E-06	1.259
1268.25	546770	42.9	0.5	21.45	0.25	187549.6	1.33E-06	1.266
1268.25	714096.6	43.5	0.6	21.75	0.3	167326.6	1.79E-06	1.275
1268.25	856706.2	44.2	0.7	22.1	0.35	142609.6	2.45E-06	1.285
1268.25	973999.6	45.1	0.9	22.55	0.45	117293.4	3.84E-06	1.298
1268.25	1097285	46.3	1.2	23.15	0.6	123285.4	4.87E-06	1.316
1268.25	1205590	47.4	1.1	23.7	0.55	108305.4	5.08E-06	1.331
1268.25	1304458	48.6	1.2	24.3	0.6	98868	6.07E-06	1.348
1268.25	1394938	49.8	1.2	24.9	0.6	90479.2	6.63E-06	1.364
1268.25	1487065	51.1	1.3	25.55	0.65	92127	7.06E-06	1.382
1268.25	1577244	52.6	1.5	26.3	0.75	90179.6	8.32E-06	1.402
1268.25	1674315	54.4	1.8	27.2	0.9	97070.4	9.27E-06	1.426
1268.25	1759401	56.2	1.8	28.1	0.9	85086.4	1.06E-05	1.449
1268.25	1843439	57.9	1.7	28.95	0.85	84037.8	1.01E-05	1.471
1268.25	1906804	59.5	1.6	29.75	0.8	63365.4	1.26E-05	1.491
1268.25	1953092	60.9	1.4	30.45	0.7	46288.2	1.51E-05	1.509
1268.25	1998182	62.4	1.5	31.2	0.75	45089.8	1.66E-05	1.527
1268.25	2053758	64	1.6	32	0.8	55575.8	1.44E-05	1.547
1268.25	2093904	65.5	1.5	32.75	0.75	40146.4	1.87E-05	1.565
1268.25	2131354	67.1	1.6	33.55	0.8	37450	2.14E-05	1.584
1268.25	2166258	68.8	1.7	34.4	0.85	34903.4	2.44E-05	1.604
1268.25	2199513	70.5	1.7	35.25	0.85	33255.6	2.56E-05	1.623
1268.25	2233069	72.4	1.9	36.2	0.95	33555.2	2.83E-05	1.645
1268.25	2258385	74	1.6	37	0.8	25316.2	3.16E-05	1.663
1268.25	2284899	75.6	1.6	37.8	0.8	26514.6	3.02E-05	1.681
1268.25	2307819	77.3	1.7	38.65	0.85	22919.4	3.71E-05	1.700
1268.25	2324447	79.2	1.9	39.6	0.95	16627.8	5.71E-05	1.721
1268.25	2337479	81.5	2.3	40.75	1.15	13032.6	8.82E-05	1.746
1268.25	2346767	83.9	2.4	41.95	1.2	9287.6	1.29E-04	1.771
1268.25	2354856	85.9	2	42.95	1	8089.2	1.24E-04	1.792
1268.25	2360099	88.7	2.8	44.35	1.4	5243	2.67E-04	1.821

Constant amplitude test data for the Region D

Δ P (N)	N (cycles)	2a (mm)	Δ 2a (mm)	a (mm)	Δa (mm)	Δ N (cycles)	da/dN (mm/cycle)	ΔK ($MNm^{-3/2}$)
1268.25	0	39.9	-	19.95	-	-	-	-
1268.25	375249	42.3	2.4	21.15	1.2	375249	3.20E-06	1.257
1268.25	576580.2	42.7	0.4	21.35	0.2	201331.2	9.93E-07	1.263
1268.25	755741	43.2	0.5	21.6	0.25	179160.8	1.40E-06	1.271
1268.25	918423.8	43.9	0.7	21.95	0.35	162682.8	2.15E-06	1.281
1268.25	1048600	44.7	0.8	22.35	0.4	130176.2	3.07E-06	1.293
1268.25	1171736	45.7	1	22.85	0.5	123135.6	4.06E-06	1.307
1268.25	1283636	46.8	1.1	23.4	0.55	111900.6	4.92E-06	1.323
1268.25	1382205	48.2	1.4	24.1	0.7	98568.4	7.10E-06	1.342
1268.25	1471935	49.2	1	24.6	0.5	89730.2	5.57E-06	1.356
1268.25	1558969	50.4	1.2	25.2	0.6	87033.8	6.89E-06	1.373
1268.25	1648998	51.9	1.5	25.95	0.75	90029.8	8.33E-06	1.393
1268.25	1746518	53.6	1.7	26.8	0.85	97519.8	8.72E-06	1.415
1268.25	1828609	55.3	1.7	27.65	0.85	82090.4	1.04E-05	1.438
1268.25	1904258	56.9	1.6	28.45	0.8	75649	1.06E-05	1.458
1268.25	1967174	58.4	1.5	29.2	0.75	62916	1.19E-05	1.477
1268.25	2013911	59.7	1.3	29.85	0.65	46737.6	1.39E-05	1.494
1268.25	2059001	61.1	1.4	30.55	0.7	45089.8	1.55E-05	1.511
1268.25	2098099	62.7	1.6	31.35	0.8	39097.8	2.05E-05	1.531
1268.25	2138245	64.1	1.4	32.05	0.7	40146.4	1.74E-05	1.548
1268.25	2175995	65.6	1.5	32.8	0.75	37749.6	1.99E-05	1.566
1268.25	2210299	67.2	1.6	33.6	0.8	34304.2	2.33E-05	1.585
1268.25	2243555	68.8	1.6	34.4	0.8	33255.6	2.41E-05	1.604
1268.25	2276810	70.6	1.8	35.3	0.9	33255.6	2.71E-05	1.625
1268.25	2302576	72.1	1.5	36.05	0.75	25765.6	2.91E-05	1.642
1268.25	2329989	73.7	1.6	36.85	0.8	27413.4	2.92E-05	1.660
1268.25	2353957	75.4	1.7	37.7	0.85	23968	3.55E-05	1.679
1268.25	2375079	77.1	1.7	38.55	0.85	21121.8	4.02E-05	1.698
1268.25	2395302	79.4	2.3	39.7	1.15	20223	5.69E-05	1.723
1268.25	2408784	81.6	2.2	40.8	1.1	13482	8.16E-05	1.747
1268.25	2419869	84.1	2.5	42.05	1.25	11085.2	1.13E-04	1.773
1268.25	2426760	86.4	2.3	43.2	1.15	6890.8	1.67E-04	1.797
1268.25	2428558	88.5	2.1	44.25	1.05	1797.6	5.84E-04	1.819

Appendix F: Hardness Values Data for AA 2014

BM								
No of Test	1	2	3	4	5	6	7	8
HV	155.7	156.2	155.8	156.7	155.8	156.4	156.9	156.7
Average HV	157							
HAZ Region C								
No of Test	1	2	3	4	5	6	7	8
HV	107.9	106.7	105.5	106.7	107.2	106.3	105.9	106.9
Average HV	107							
HAZ Region D								
No of Test	1	2	3	4	5	6	7	8
HV	118.7	118.3	117.8	118.5	117.5	118.9	118.4	119.3
Average HV	118							